A Study of ^{19}Ne Resonances and their Astrophysical Implication for the Detection of Novae

Joscelin E. Riley

Doctor of Philosophy

University of York

Physics

October 2017

Abstract

Classical novae are the most common astrophysical thermonuclear explosion and are thought to contribute noticeably to the galactic chemical evolution. As one of the few environments that can be modelled primarily from experimental nuclear data, observations of isotopic abundances would provide a direct test for current hydrodynamic codes. Gamma rays are the only such radiation that can be observed to trace the nucleosynthesis of isotopes directly. Fluorine-18 produced in the runaway is the strongest γ-ray source immediately after the outburst, although reaction rates must be constrained further to predict its intensity and therefore detectability.

The ^{18}F(p,α)^{15}O reaction remains the largest uncertainty in constraining these rates as key nuclear state parameters in the compound nucleus, ^{19}Ne, are still not known despite considerable experimental effort. To resolve this, the most important levels close to the proton threshold were populated using the charge exchange reaction ^{19}F(^{3}He,t)^{19}Ne at IPN, Orsay. A Split-pole spectrometer measured the tritons and identified the states of interest, whilst a highly segmented silicon array detected alpha-particle and proton decays from ^{19}Ne over a large angular range and at a high angular resolution.

The resonance parameters, extracted from the experimental results, provide evidence for a postulated broad state and produce a spin-parity result for the important -122 keV subthreshold state in direct contradiction to previous measurements of the nucleus. The results, in addition to other recent studies, provided input parameters for a comprehensive set of theoretical R-matrix calculations that have realistically modelled the remaining uncertainty in the reaction rate. The newly proposed rate is discussed, along with implications for future studies of the destruction reaction, both direct and indirect, which are necessary in providing an answer to the γ-ray detectability of classical novae.

Contents

List of Figures

List of Tables

Acknowledgements

For every chapter in this thesis, hours have been spent pondering on how to begin. Now facing the acknowledgments I find it is no different, though with a liberating feeling of having almost reached the end. Unlike the rest of this tome, however, I shall endeavour to keep this brief.

From the first meeting when I was but a lowly undergraduate student, to the last only a day ago, Dr. Alison Laird's supervision has kept both my project and my floundering as a scientist in check. Her acceptance of my candidacy has changed my life (for the better) and I am indebted to the assistance and encouragement she provided throughout. If Alison were considered to be playing the part of Athos, then thanks must also go to the other two Musketeers, Drs. Simon Fox and Nicolas de Séréville. Their help has been invaluable over the last few years in the face of countless obstacles (mostly of my own design) and I can only hope I find an opportunity to repay them.

I would also like to acknowledge my experimental collaborators at IPN and GANIL and the time they gave both on and off shift, without whom I would have no data. In particular, Fairouz Hammache and Iulian Stefan who frequently greeted me with croissant and pizza on my many (many) trips to Orsay. From my attachment to the TRIUMF national lab in Canada, I would thank Dr. Chris Ruiz for agreeing to host me and Prof. Barry Davids and the EMMA group for allowing me to do some more practical 'science'.

I now address my fellow students... Firstly to Ben and Ed, without whom my rent would have tripled and my work finished in half the time - a net gain I think. To the astro students, Stephen, Jess, honorary Adelle, Matt, Nic, Ed, Carine and Joe, the hours of deliberation spent in the meetings became the foundation for my theory chapter. To James and Ruchi specifically, I feel as though we have struggled through this elusive subject known as nuclear physics together and only you two have emerged victorious. I am so grateful for the discussions in the office (not all of them) and I can only hope that my thesis is half as good as yours. Although now left for greener pastures, I also have to thank (in no particular order) Lianne, Gemma, Tom, Jack, Paul, Victoria and Phil for making me feel welcome and for starting my education into experimental nuclear physics.

Finally I must thank my family, no doubt sleeping as I write into the small hours on the morning of the deadline. Your support has been constant throughout my education, from the moment I was first dropped off at nursery, to today when I submit my PhD thesis. Words struggle to convey my gratitude for your patience and motivation.

Declaration of Authorship

I confirm that this work was done wholly whilst in candidature for a research degree at the University of York and has not previously been presented for an award at this, or any other, University. Where I have consulted the published work of others, the source has always been clearly attributed and referenced. With the exception of such sources, this thesis is a presentation of original work of which I am the sole author.

Chapter 1

Astrophysical Background

1.1 Introduction

The elemental components that make up all forms of life are forged within the midst of stars. Their very creation provides the sunlight used as the primary source of energy by almost every known living organism. It is through life that the Universe comes to understand itself, beginning with humanity's fascination with the heavens. Their motions have been studied for millennia by civilisations across the globe, and only within the last century has the nature of stellar creation and evolution has been perceived. To truly understand the physical processes of the Universe, it is necessary to observe it, not on the astronomical scale but rather at the subatomic level, where atoms are decomposed into their electron shell and nuclear core. It is this nucleus, comprised of protons and neutrons, that defines the elements, and the forces between them that govern their transmutation.

Since their discovery in 1911 by Ernest Rutherford [1], nuclei and their radiations have been used as probes for understanding the atoms themselves. Whilst the study of atomic and nuclear structure is of great importance, it is the interaction between nuclei and their energy generation through the synthesis of new elements, that is of interest to the field of nuclear astrophysics [2, 3]. The study of nucleosynthesis begins with the measurement of current isotopic abundances. Because of the influences the formation of our solar system has had on the terrestrial abundance of elements, it is necessary to look further afield to the galactic scale.

The majority of mass in the galaxy constitutes hydrogen and helium, known to have been created in the first few minutes following the big bang[1]. The remaining naturally occurring elements up to uranium ($Z < 92$) are formed through the fusion of lighter nuclei in hot, dense stellar environments. There are a number of nuclear reaction processes that become available depending on the conditions of the stellar environment. The Sun for example, as with other stars of its nature, produces energy through the fusion of hydrogen into helium, eventually burning the helium into carbon or oxygen, but will be incapable of fusing heavier elements.

Heavier mass stars are able to create pressures in their core for the fusion of carbon, neon, oxygen and silicon, synthesising elements up to and including iron. It is at this point that studies of nuclear structure show how heavier elements cannot be synthesised in a similar hydrostatic manner. The most fundamental property of a nucleus is its mass, shown not to equal the product of its constituent particles. The mass deficit is known as the nuclear binding energy and is the energy required to separate the constituent nucleons. Measurements of the binding energy identify a peak at ^{56}Fe where synthesis of lower masses nuclei emit energy from their fusion and higher mass nuclei consume energy. Energy generation from nuclear fusion is the balancing force to the natural gravitational collapse of a star, some of which escapes into the local system in the form of photon radiation.

Indeed, once the energy-generating fuel available to a massive star has been exhausted, it can no longer support itself and the star dies, often with catastrophic consequences. It is in the death of stars that heavier elements can be produced, known as explosive nucleosynthesis. Large neutron fluxes produced in the most energetic explosions (supernovae) enable their rapid capture by the heavy elements from the stellar core, synthesising neutron-rich nuclei that decay into heavy mass elements up to uranium. The violent demise to massive stars help to project the newly created elements into the interstellar medium, adding their contribution to the abundances observed today. Additional thermonuclear reaction processes are responsible for the production of specific nuclei, however, this requires a more in-depth knowledge of their stellar environments and as such have not been discussed.

It is classical novae (another such explosive environment) that is the astrophysical site of interest to this work, both in its contribution toward the galactic elemental abundance and the astrophysical processes that occur in its progenitor.

[1]Big bang nucleosynthesis is also thought to have created ^{7}Li and ^{7}Be in much smaller quantities.

1.2 Classical Novae

To a terrestrial observer, a classical nova is perceived as the transitory brightening of a star over a period of a few days. The bursts of radiation, characterised by their light curve (Fig. 1.1) and spectroscopic analysis [4], are considered to be the result of runaway thermonuclear reactions caused by the accretion of matter onto the surface of a white dwarf star.

1.2.1 Explosive Environment

Approximately half of all observed star systems in the galaxy exist as two (or more) stars[1] orbiting around a common centre of mass [5]. Due to the high probability of asymmetric forces driving the creation of star systems, binary stars usually differ in mass from one another, causing each to evolve at a different rate. The heavier of the two stars will generate higher temperatures from its increased density, consuming its available fuel at a higher rate. The formation of a white dwarf star is dependent on the mass of its progenitor star. During the last stages of nuclear burning, stars with <8 $M_\odot$ shed their outer layers through a series of thermal pulses, forming a planetary nebula and leaving behind its core as the new white dwarf remnant.

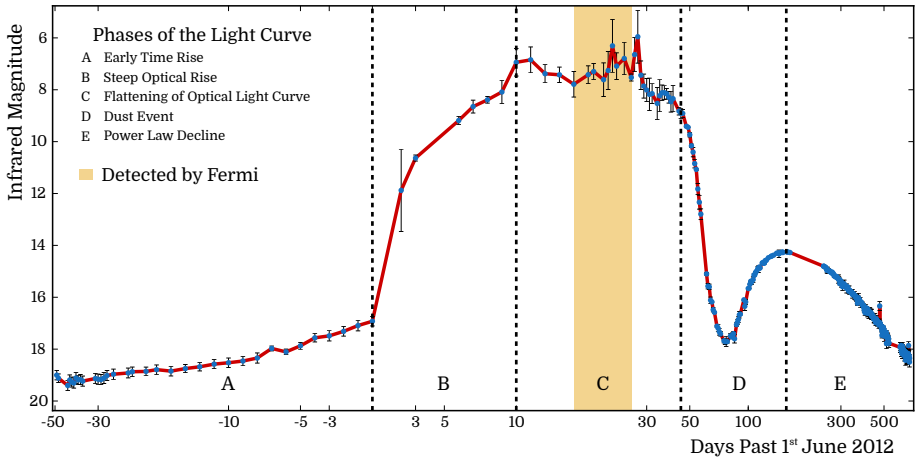

Figure 1.1: Taken from ref. [6], infrared light curve over time of V1324 Sco detected in 2012. The characteristic rise and fall of its near visible radiation identifies the event as a nova. The highlighted time period was during γ-ray detection by the FERMI gamma-ray telescope.

[1] Binary percentages are dependent on star type and are still frequently debated.

The majority of white dwarfs consist of carbon and oxygen as a result of triple-α burning in the core of its progenitor. Slightly higher mass stars, able to reach temperatures for the fusion of carbon, produce white dwarf remnants composed of oxygen and neon. No longer able to undergo fusion to support themselves from gravitational collapse, white dwarfs condense until their electrons behave as a Fermi gas, occupying all available quantum states below the Fermi energy and repulsing one another through the Pauli exclusion principle. This degeneracy pressure is limited in mass (calculated by Chandrasekhar to be 1.459 $M_\odot$ [7, 8]) before the gravitational forces are too great and the star is collapsed further to be held by the degeneracy pressure of neutrons, creating a neutron star.

The occurrence of novae in such a binary system is dependent on the proximity of the white dwarf and its less evolved companion. Close to each star, surfaces of equal gravitational potential are approximately spherical. Further from the stars, the potential becomes ellipsoidal, stretched by the potential of its stellar companion. A critical equipotential, known as the Roche lobe, forms the L_1 Lagrangian point defining the limit at which orbiting material is gravitationally bound to that star. Fig. 1.2 shows a diagrammatic depiction of the Roche lobe. Depending on their separation, it is possible for the less evolved companion star to expand beyond the Roche lobe, displacing its atmospheric gases of (primarily) hydrogen into the gravitational potential of the white dwarf through L_1. The matter does not fall directly onto the surface but is formed, at a typical rate of 10^{-10} $M_\odot yr^{-1}$, into an accretion disk. Friction converts the kinetic energy of the disk into thermal energy causing the material to descend toward the degenerate surface of the white dwarf.

The new hydrogen rich matter on the surface of the white dwarf is gradually compressed and heated from subsequent accretion, causing the lower layers to become electron degenerate, matching the pressures of the white dwarf. Hydrogen begins to fuse into helium via proton-proton (*p*-*p*) burning during the accretion phase, causing the temperature to increase further. The Fermi-Dirac statistics that govern the behaviour of the degenerate matter decouple the pressure of the Fermi gas from its temperature. The nova envelope cannot expand from the fusion ignition to regulate its temperature thus causing a thermonuclear runaway at its base. At this point, temperatures reached in the envelope of $T = 0.05-0.35$ GK ($E = k_bT = 0.05-0.36$ MeV) are sufficient for hydrogen burning via the hot(H)-CNO cycle using the carbon and oxygen isotopes dredged up from the white dwarf to act as the initial catalysts. The runaway reactions last approximately 1000s until

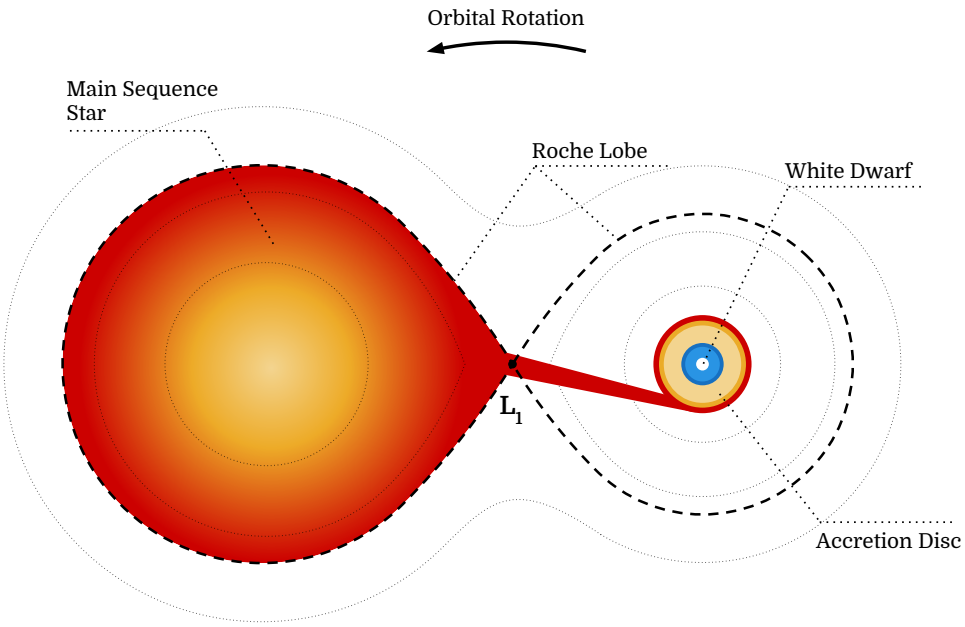

Figure 1.2: Diagram of a binary star system consisting of a white dwarf and a main-sequence star. The stars are close enough for hydrogenic matter to pass between them, falling onto the surface of the white dwarf.

the degeneracy of the material is lifted at the Fermi temperature and an explosion occurs, ejecting approximately $10^{-6}M_{\odot}$ of material into the interstellar medium at 10^{6} ms^{-1} [9].

The nova explosion is not thought to destroy the white dwarf star beneath, allowing the accretion of H from its companion to continue generating enough mass every 10^{4} years for further novae events [10]. Given the commonality of binary systems it is not surprising that novae explosions occour at a high frequency in the galaxy, at a rate of 34^{+15}_{-12} yr^{-1} [11]. Whilst the ejected mass of a nova is small in comparison to more energetic supernova events, their frequency could suggest a significant contribution to the galactic abundance and evolution [12, 13]. Indeed, observations of novae spectra at optical, infrared and ultraviolet wavelengths reveal an overabundance of particular elements in comparison to our solar system abundances [14].

Hydrodynamic models show that the novae ejecta from carbon-oxygen white dwarfs are dominated by C, N and O nuclei, whilst an additional enrichment of Ne, Na and Al is estimated from heavier oxygen-neon white dwarfs [15]. The composition of ejected mass from a nova explosion contains key information on the white dwarf beneath and allows predictions of the accretion rate, temperature and timescale. Whilst chemical abundance

measurements are available from the near optical wavelengths used for current observations, it is thought that isotopic abundances may be determined through the detection of γ-ray emission. Constraint on the production of key isotopes would assist models in their simulation of nova explosions in both their nuclear and astrophysical inputs.

1.2.2 Nucleosynthesis

p-p Chain

Nuclear reactions in novae can synthesise nuclei up to mass A $\simeq$ 40 [14, 16]. The process begins, as mentioned earlier, at low temperatures with the fusion of four protons (^{1}H) into a ^{4}He nucleus through proton-proton (*p-p*) reaction chains. Each conversion releases 26.7 MeV into the nova envelope, increasing its temperature. The three possible reaction chains have been shown in Fig. 1.3. *p-p* I, II and III dominate at <0.018, 0.018−0.025 and >0.025 GK respectively meaning that all three chains are expected to occur during the accretion phase in novae. There are no stable nuclei of mass A = 5 or 8, preventing the synthesis of heavier nuclei using the *p-p* chains alone. For the ignition to progress to the runaway sequence required of a nova, heavier mass isotopes must already be present in the system to act as catalysts to burn protons into ^{4}He at a faster rate.

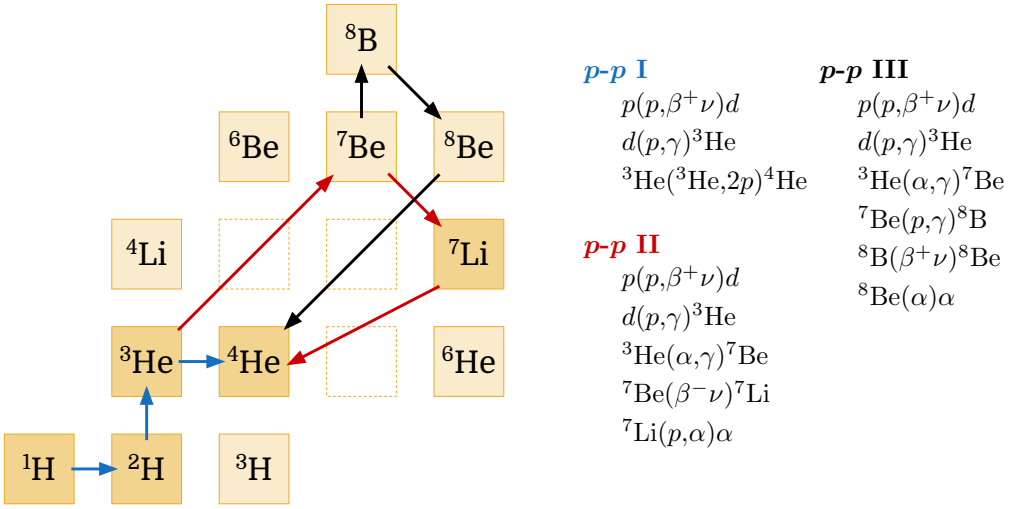

Figure 1.3: Diagram of the *p-p* reaction chains that burn four *p*'s into a helium-4 nucleus. *p-p* I is shown in blue, *p-p* II is shown in red and *p-p* III is shown in black.

CNO Cycle

Carbon and oxygen are readily available from the surface of the white dwarf and are dredged by mixing with the accreted matter to act as seeds for the carbon-nitrogen-oxygen (CNO) burning cycle. The cycle is catalytic in nature owing to the fact that, for the simplest CNO cycle shown in Fig. 1.4 as an example, the ^{12}C is recovered in the final reaction allowing the cycle to restart and the seed nuclei to remain in equilibrium. The rate of the cycle is determined by the speed of the slowest reaction. For CNO cycles this is usually limited by proton capture such as ^{14}N$(p,\gamma)^{15}$O below, where lower temperatures mean protons have less energy and a lower probability of tunnelling through the Coulomb barrier. Late in the accretion phase, hydrogen burning through *p*-*p* chains contribute less and the CNO cycle begins to dominate.

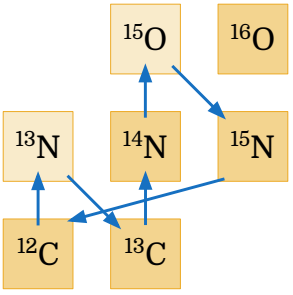

CNO I

^{12}C$(p,\gamma)^{13}$N
^{13}N$(\beta^{+}\nu)^{13}$C
^{13}C$(p,\gamma)^{14}$N
^{14}N$(p,\gamma)^{15}$O
^{15}O$(\beta^{+}\nu)^{15}$N
^{15}N$(p,\alpha)^{12}$C

Figure 1.4: Diagram of the first CNO cycle that burns four *p*'s into a helium-4 nucleus.

Further increases in the envelope temperature provide more energy to the proton fuel and the destruction of ^{13}N, through proton capture, becomes more favourable than its β^{+} decay. This occurs at approximately T = 0.1 GK evolving the CNO cycle into the H-CNO cycle (see Fig. 1.5). An important distinction between hot and 'cold' cycles are their limiting reactions. As mentioned previously, the CNO cycle rate is limited by its proton capture whilst the H-CNO cycles become β^{+} limited, creating a build-up of nuclei waiting to decay via positron emission. Mediated by the weak force, the waiting points in the H-CNO cycle also mean that the reaction rate becomes independent of temperature. The three H-CNO cycles form a network where material can move between cycles at each branching point allowing higher mass nuclei to be synthesised. For example ^{17}F may either decay via positron emission continuing the H-CNO II cycle, or proton capture, continuing

the H-CNO III cycle. The primary energy generation for novae between T = 0.1−0.35 GK is provided by the three H-CNO cycles.

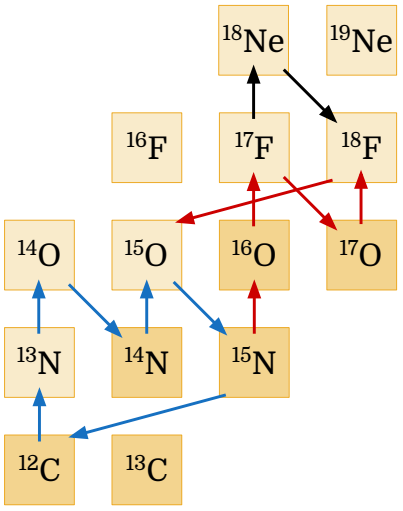

H-CNO I

^{12}C$(p,\gamma)^{13}$N
^{13}N$(p,\gamma)^{14}$O
^{14}O$(\beta^+\nu)^{14}$N
^{14}N$(p,\gamma)^{15}$O
^{15}O$(\beta^+\nu)^{15}$N
^{15}N$(p,\alpha)^{12}$C

H-CNO II

^{15}O$(\beta^+\nu)^{15}$N
^{15}N$(p,\gamma)^{16}$O
^{16}O$(p,\gamma)^{17}$F
^{17}F$(\beta^+\nu)^{17}$O
^{17}O$(p,\gamma)^{18}$F
^{18}F$(p,\alpha)^{15}$O

H-CNO III

^{15}O$(\beta^+\nu)^{15}$N
^{15}N$(p,\gamma)^{16}$O
^{16}O$(p,\gamma)^{17}$F
^{17}F$(p,\gamma)^{18}$Ne
^{18}Ne$(\beta^+\nu)^{18}$F
^{18}F$(p,\alpha)^{15}$O

Figure 1.5: Diagram of the H-CNO cycles that burn four p's into a helium-4 nucleus. H-CNO I is shown in blue, H-CNO II is shown in red and H-CNO III is shown in black.

Convection thought to occur within the nova envelope [16] transports the concentration of β^+ nuclei to the outer surface and replaces its mass with unburnt hydrogenic matter. The resulting nucleosynthesis is far from hydrostatic equilibrium and triggers an explosive increase in pressure and the ejection of the envelope. Peak temperatures for CO novae have been modelled to be lower than those of ONe novae, typically preventing the synthesis of isotopes heavier than oxygen. The seed nuclei in the ONe white dwarfs, comprising mainly of oxygen and neon, create a slower ignition time, but allow for more frequent breakout from the H-CNO cycles and the subsequent rapid capture of protons (rp-process) [17]. The reactions after breakout are not thought to contribute significantly to the energy of a nova outburst but do allow the nucleosynthesis of isotopes between $20 \leq A \leq 40$.

1.3 Nova γ-ray Luminosity

There are two suspected sources of γ rays from classical nova. The first is related to particle acceleration from the shocks between the nova ejecta and the remaining accretion disk. The shocks produce radiation at very high energies (∼GeV) and it is this emission that was detected by the Fermi satellite highlighted in Fig. 1.1. The second γ-ray source, closer to

MeV in energy, arises from the ejection of radioactive nuclei and allows the nucleosynthesis during the novae event itself to be traced directly. Though yet to be detected with any certainty, it is this radiation that would provide information on the astrophysical processes that occur during the explosive burning. Gamma-ray observations would provide more stringent tests of hydrodynamic models that simulate both the interaction of the envelope with the white dwarf beneath [17] as well as the equations of state for the envelope itself. With consistent monitoring, such detections may also provide the ability to observe novae that would otherwise be invisible due to interstellar dust.

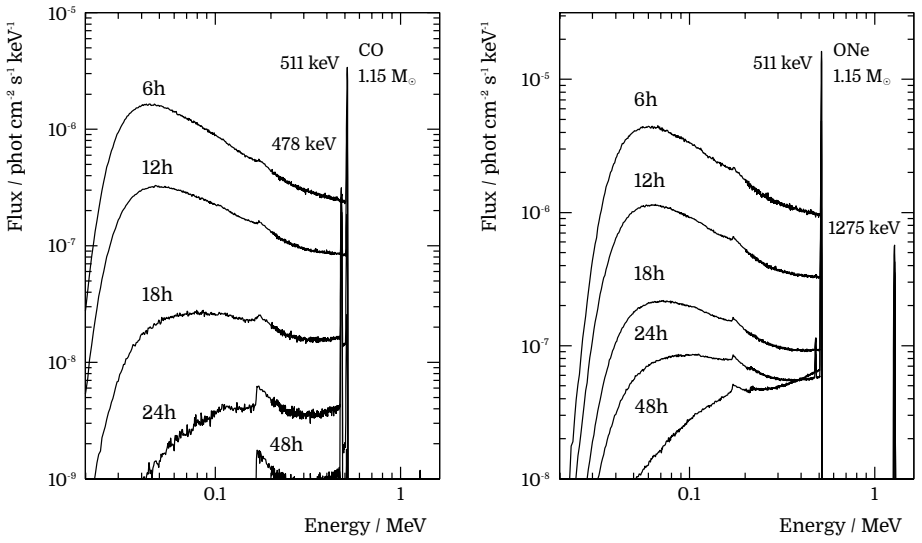

Figure 1.6: Simulated γ-ray emission from CO (left) and ONe (right) novae taken from ref. [18]. The peaks are caused by the decay of isotopes listed in Table 1.1 and the continuum is due to the Compton scattering of the emitted photons. No γ rays are expected below $\sim$30 keV due to photoelectric absorbtion.

The very short lived ^{14,15}O and ^{17}F nuclei, produced in the H-CNO cycle, decay whilst the envelope is still opaque to radiation with a lifetime of τ = 102, 176 and 93 seconds respectively. The decay from these isotopes help power the expansion of the envelope [9], however, their early destruction also prevents their detection. Fig. 1.6 shows the γ-ray flux expected to be visible from CO and ONe novae based on Monte-Carlo simulations [18]. The two novae are able to be distinguished by their production of ^{7}Be (478 keV) and ^{22}Na (1275 keV) respectively, however, the emission after the first few hours is thought to be dominated by the 511 keV line, produced by the destruction of e^- - e^+ pairs [19]. Positron production arises primarily from the decay of ^{13}N and ^{18}F. Because the lifetime of ^{13}N (τ = 862 s) still places its peak emission prior to the envelopes radiation transparency, ^{18}F

(τ = 158 min) is, therefore, the best candidate for γ-ray observations of nucleosynthesis within novae.

Isotope	**Lifetime**	**γ-ray Emission**	**Nova**
^{7}Be	77 days	478 keV	CO
^{13}N	862 s	511 keV & continuum	CO, ONe
^{14}O	102 s	-	CO, ONe
^{15}O	176 s	-	CO, ONe
^{17}F	93 s	-	CO, ONe
^{18}F	158 min	511 keV & continuum	CO, ONe
^{22}Na	3.75 yr	511, 1275 keV	ONe

Table 1.1: List of the primary radioactive isotopes produced during a nova event and their contribution to the expected γ-ray spectrum.

Gamma rays are emitted well before the visual maximum of the nova, meaning wide field of view instruments must already be monitoring the sky at the appropriate energy range[1]. Such instruments included the Burst and Transient Source Experiment (BATSE) aboard the Compton Gamma-Ray Observatory (CGRO) where *a posteriori* analysis, by Hernanz *et al.* [20], found upper limits to 3σ for the 511 keV emission from three nova. Currently, the most promising search for novae γ-ray emissions is from the Swift multi-wavelength space observatory launched in 2004 [21]. The satellite contains the Burst Alert Telescope (BAT), capable of observing 2 sr of the sky at any time, and whilst no γ-ray emissions were observed from the 24 novae events detected since its launch, none were within its currently predicted detectable range of $\sim$1 kPc. Also in current operation, the INTErnational Gamma Ray Astrophysics Laboratory (INTEGRAL) is able to extend this detectable range to 4-5 kPc, however, its much narrower field of view (0.2 sr) makes nova detection far less likely [22].

1.3.1 ^{18}F Abundance in Novae

The distance at which γ rays can be detected by orbital observatories is dependent on a number of properties detailing the evolution and expansion of the novae envelope. The biggest uncertainty, however, is that of ^{18}F abundance [18]. The radioisotope contributes directly to the flux of both the 511 keV line (from e^- - e^+ annihilation) and the continuum (caused by the Compton scattering of the emitted γ rays), providing a limit to

[1]Spectral resolution must also be high enough to distinguish the cosmic 511 keV line from the slightly blue-shifted 511 keV line from novae.

the nova detection range when using the detectors currently aboard orbiting satellites. As shown in Fig. 1.5, the synthesis of ^{18}F is a result of the ^{17}F(p,γ)^{18}Ne($\beta^+\nu$)^{18}F or ^{17}F($\beta^+\nu$)^{17}O(p,γ)^{18}F reactions in the H-CNO cycle. The rates of both the ^{17}F(p,γ) reaction [23] and the ^{17}O(p,γ) reaction [24] have been measured to a high precision and their uncertainties have been well constrained. Proton-induced reactions

- ^{18}F(p,α)^{15}O
- ^{18}F(p,γ)^{19}Ne

on the fabricated ^{18}F, result in the destruction of the radioisotope, and it is these reactions that require further study. At nova temperatures, the majority of ^{18}F destruction occurs from the (p,α) reaction whilst the (p,γ) contributes a factor of 1000 less [25]. Current destruction reaction rate calculations place the detectable range of novae between 0.5 and 5 kPc [21]. This order of magnitude uncertainty must be resolved through accurate measurements of the ^{18}F destruction rate in order to determine the feasibility of γ-ray detections of novae and to interpret the fluxes correctly if such an event were to be observed.

1.4 Current Status of ^{18}F Destruction Rate

Both of the proton induced reactions, mentioned previously, proceed through the formation of unbound resonant states in the ^{19}Ne compound nucleus before decaying via their respective methods[1]. The rate at which these reactions occur is decided by the parameters of the ^{19}Ne resonant states where the contribution of each is dependent on the energy of the reaction (i.e. the temperature of the environment). The study of the ^{19}Ne nucleus was only begun in earnest from 1970, with experiments by Garrett *et al.* [26] and Haynes *et al.* [27] using (^{3}He,α) neutron pickup reactions to observe a number of resonances, both above and below the p-threshold, for the first time. Those above threshold were used by Wiescher and Kettner [28] in conjunction with states postulated from its well studied mirror nucleus ^{19}F for the first estimation of the ^{18}F(p,α) reaction rate.

Experiments to study the ^{19}Ne nucleus continued over the next few decades using a variety of charge exchange or particle transfer reactions to populate the states [29]. The first direct reaction measurements of the ^{18}F(p,α) cross section were not begun until the developments of radioactive ^{18}F beams in the mid 1990's. Experiments by Rehm *et al.* [30–32],

[1]Proton decay is also possible, however, as this reaction would cause no nuclei to be lost within the nova system, it has no contribution to the destruction rate.

Coszach *et al.* [33] and Graulich *et al.* [34] measured the yield from ^{18}F ion reactions with polypropylene targets and quickly found the rate across all the experimental energies to be dominated by a single $3/2^+$ resonance at ∼650 keV above the proton threshold. Extraction of the state's parameters proved to be ambiguous however, due to the resolution limitations of these early experiments. Only in 2001 did Bardayan *et al.* [35] measure the resonance's energy, width and strength unambiguously.

The limitations of the direct reactions for studying the structure of the nucleus, and also for measuring the reaction rate at the necessary novae temperatures, drove the need for further work in measuring the resonance parameters indirectly. The ^{19}F(^{3}He,t)^{19}Ne charge exchange reaction was therefore performed by Utku *et al.* [36] improving the measurement of 14 states and observing 3 new states above the p-threshold. Simultaneous detections of the alpha-particle and proton decays from the resonances populated in the experiment also helped to provide the first constraint on decay branching ratios. The results (and associated uncertainties) from this experiment were utilised by A. Coc *et al.* [37] in the year 2000 who began constraining the reaction rate within the expected nova temperature range. From this work the rate was found to vary by a factor of ∼300 between the lowest and highest calculations.

Further direct ^{18}F(p,α) and ^{18}F(p,p') measurements were performed after the turn of the millennium in the centre of mass energy region, between 330 and 1000 keV, by Bardayan *et al.* [38–40], Chae *et al.* [41] and de Séréville *et al.* [42, 43]. Bardayan was able to provide the first determination of the strength of the 330 keV resonance thought to dominate the reaction rate in novae in addition to achieving the precise measurement of the 665 keV resonance mentioned above. Given the strength of the 665 keV resonance, known to have $J^\pi = 3/2^+$, and the discovery/postulation of further $3/2^+$ states closer to the proton threshold at $E_{c.m.} = 8$ and 38 keV, interference effects were thought to contribute to the rate over the energy range of interest (see Fig. 1.7 taken from ref. [43]). The measurements made by Chae and de Séréville were therefore performed 'off resonance' in an attempt to constrain the potential $3/2^+$ interference terms. The measurement by Chae was done at energies above the 665 keV resonance, whilst those of de Séréville performed below in energy, both with the intention of extrapolating the rate down to astrophysical energies using the R-matrix formalism. With the data available, it was still not possible to identify the correct interference pattern of the resonances thus further data were required both from direct capture rates and indirect resonance parameter measurements.

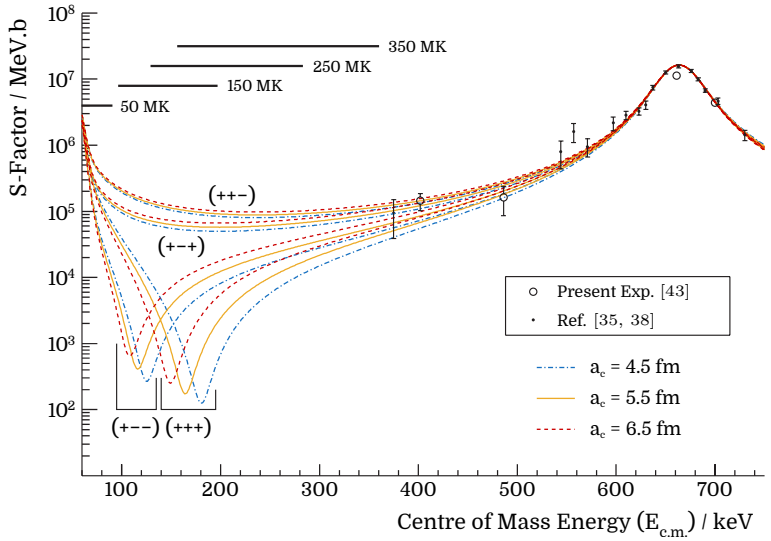

Figure 1.7: Interference between $3/2^+$ states in ^{19}Ne as calculated by de Séréville *et al.* in 2009. Figure taken from ref. [43].

Concurrently, studies of the mirror nucleus ^{19}F were performed from 2003 to 2007 using the neutron transfer reaction ^{18}F(d,p) as reported by de Séréville *et al.* [44–47] and Kozub *et al.* [48, 49]. These studies provided useful comparisons between nuclear states from the two analogue nuclei. ^{19}F resonance parameters that were easily accessible due to their height above the p-threshold allowed parameters of ^{19}Ne resonances just above the p-threshold to be deduced. A comprehensive review of the known states in ^{19}Ne above the 6411 keV p-threshold and their analogue states in ^{19}F was conducted by Nesaraja *et al.* [50] in 2007. Accumulating all prior experimental measurements of both nuclei and providing estimates of unmeasured ^{19}Ne nuclear level parameters (in addition to unobserved nuclear levels), Nesaraja provided a useful reference from which to base further rate calculations. Indeed a re-analysis of the reaction rate by A. Coc [51] in 2008 successfully reduced the uncertainty from a factor of 300 to a factor of 10 (see Fig. 1.8).

Since the publication by Nesaraja, many states have been remeasured in addition to new observations of states previously missing from the level scheme. Table 1.2 summarises the changes to the ^{19}Ne level scheme since the publication of Table I in ref. [50] and presents resonance parameters known with the least uncertainty. Changes or additions (discussed in the following paragraph) have been highlighted in red. Included in the table are results from this work that will be discussed in subsequent chapters. Fig. 1.9 has also been included to visualise the energy levels in ^{19}Ne and their relation to the mirror nucleus ^{19}F. Analogue assignments have remained unchanged from Nesaraja unless indicated.

E_x / MeV	$E_{c.m.}$ / keV	J^π	Γ_α / keV	Γ_p / keV	Γ_γ / eV
6.008(20)[a]	−403*	$(\frac{1}{2}^+)$[b]	124(25)[a]	ANC = 4[c] fm$^{-\frac{1}{2}}$	...
6.014(2)[d]	−397*	$\frac{3}{2}^-$[d]	...	...	...
6.072(2)[d]	−339	$\frac{3}{2}^+$, $\frac{5}{2}^-$[d]	6×10^{-4}[d]	0.143[d]	...
6.097(3)[d]	−314	$\frac{7}{2}^+$, $\frac{9}{2}^+$[d]	...	...	...
6.132(3)[d]	−282*	$\frac{3}{2}^+$, $\frac{5}{2}^-$[d]	7×10^{-4}[d]	0.143[d]	...
6.282(2)[e]	−129*	$\frac{1}{2}^+$[f], $\frac{9}{2}^+$, $\frac{11}{2}^+$[a]	11.624[g], ...	ANC = 73.069[h] fm$^{-\frac{1}{2}}$, ...	...
6.295(2)[e]	−116	...	...	...	...
6.411	0	^{18}F + p			
6.416(3)[d]	5*	$\frac{3}{2}^-$[d,f], $\frac{5}{2}^+$[d]	0.5(5), 0.126(126)[d]	[47(47), 1.2(12)] $\times10^{-51}$[d]	0.77(41)
6.437(9)	26	$\frac{1}{2}^-$	220(20)	$1.1(11)\times10^{-20}$	[1(1)]
6.440(3)[d]	29	$\frac{11}{2}^+$[d]	$20(13)\times10^{-3}$	$1.8(18)\times10^{-38}$	0.35(18)
6.459(3)[d]	48*	$\frac{3}{2}^+$[f], $\frac{5}{2}^-$[d]	4(4), 5.5(55)[d]	[2.35(4), 8.4(84)] $\times10^{-14}$[d]	1.1(6)
(6.504(30))	93	$(\frac{7}{2}^+)$	0.4(4)	$4.6(46)\times10^{-10}$	0.14(8)
6.537(15)[i]	126	$(\frac{9}{2}^+)$	$1.3(11)\times10^{-2}$	$2.7(27)\times10^{-12}$	0.30(16)
6.700(3)[d]	289*	$(\frac{5}{2}^+)$	1.2(10)	$1.2(12)\times10^{-5}$	0.29(15)
6.742(2)[d]	331*	$\frac{3}{2}^-$	5.2(37)	$2.22(69)\times10^{-3}$	5.0(26)
6.851(4)[e]	440	$(\frac{3}{2}^-)$	Γ_t = 40(20)[e]	$9.7(97)\times10^{-3}$	2.8(15)
6.864(1)[e]	453*	$\frac{7}{2}^+$[a]	1.2(0.9)	$1.1(11)\times10^{-5}$	2.3(12)
(6.939(30))	528	$(\frac{1}{2}^-)$	99(69)	$3.4(34)\times10^{-2}$	[1(1)]
6.968(19)[i]	557	$(\frac{5}{2}^+)$	29(25)	$4.7(47)\times10^{-2}$	[1(1)]
7.076(2)	665*	$\frac{3}{2}^+$	23.8(12)	15.2(1)	$0.072^{+0.172}_{-0.061}$[j]
7.173(5)	762*	$\frac{11}{2}^{(-)}$	$1.2(10)\times10^{-2}$	$9.8(98)\times10^{-8}$	0.15(8)
7.238(6)	827	$\frac{3}{2}^+$	6.0(52)	0.35(35)	[1(1)]
7.253(10)	842*	$(\frac{1}{2}^+)$	23(20)	0.2(2)	[1(1)]
7.420(14)	1009*	$\frac{7}{2}^+$[a]	71(11)	27(4)	[1(1)]
7.500(3)[k]	1096*	$\frac{5}{2}^+$[k]	1.0(1)[k]	1.5(1)[k]	5.5(29)
7.531(11)	1120*	$\frac{5}{2}^-$	21(11)	10(6)	[1(1)]
(7.558(30))	1147	$(\frac{5}{2}^-)$	21(18)	1.3(13)	[1(1)]
7.616(5)[l]	1206*	$\frac{3}{2}^+$	43(15)	2(1)	1.8(10)
7.644(12)	1233*	$(\frac{1}{2}^-, \frac{3}{2}^-)$[k]	16(6)	27(10)	[1(1)]
7.700(10)	1289*	$(\frac{5}{2}^-)$	6.2(53)	1.7(17)	[1(1)]
7.758(6)[k]	1347*	$\frac{3}{2}^+$[k]	5(2)[k]	42(10)[k]	...
7.819(11)	1408*	$(\frac{7}{2}^+)$	4(3)	18(13)	0.53(28)
(7.826(30))	1415	$(\frac{11}{2}^+)$	1.7(15)	$6.4(64)\times10^{-3}$	0.47(25)
7.879(26)[m]	1468*	$\frac{1}{2}^{(+)}$[l]	130(108)[l,m]	228(50)[m]	...
7.944(15)	1533*	$(\frac{5}{2}^+)$	26(22)	5.9(12)	[1(1)]
7.984(8)[k]	1573*	$(\frac{1}{2}^+)$[k]	34(13)[k]	$8(^{+8}_{-4})$[k]	[1(1)]
(8.014(30))	1603	$(\frac{3}{2}^+)$	2.9(22)	4.8(48)	[1(1)]
8.072(30)[m]	1661*	$(\frac{1}{2}^+)$	Γ_α/Γ_p = 0.22(1.2)[m]	3.34(2.89)[m]	1.17(59)

[a] This work. [b] Dufour & Descouvemont [56]. [c] Boulay *et al.* [60].
[d] Laird *et al.* [52]. [e] Parikh *et al.* [57]. [f] Bardayan *et al.* [61].
[g] Adekola *et al.* [53]. [h] A. S. Adekola [58]. [i] Cherubini *et al.* [62].
[j] Akers *et al.* [54]. [k] Murphy *et al.* [59]. [l] Dalouzy *et al.* [63].
[m] Adekola *et al.* [55]. * Resonances fitted in Fig. 4.15.

Table 1.2: ^{19}Ne resonance parameters adapted from Table I in ref. [50]. Parenthesised E_x represent missing levels, parenthesised J^π are from mirror assignments and bracketed Γ_γ are assumed widths.

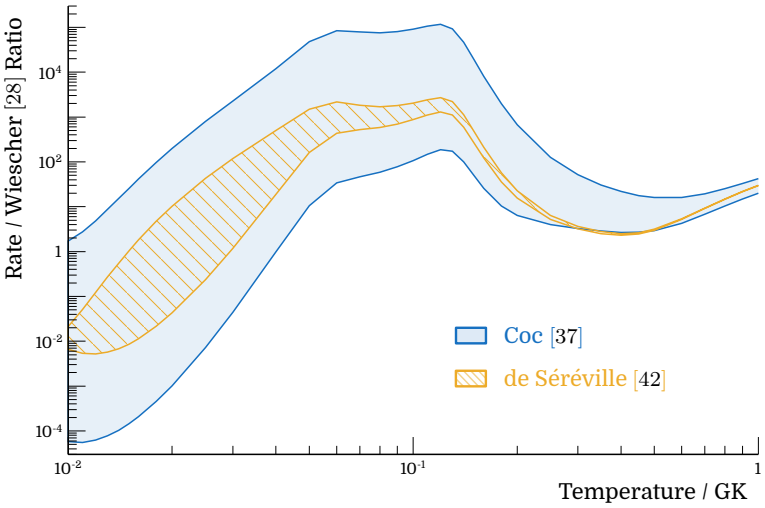

Figure 1.8: Reaction rate ratio between the first calculation by Wiescher & Kettner in 1982 [28] and Coc *et al.* in 2000 [37] (blue) and de Séréville *et al.* in 2008 [42] (red). Figure taken from ref. [37].

The first change came from work by Dufour & Descouvemont [56] who highlighted two $1/2^+$ states ($E_{c.m.} = -410$ keV, 1490 keV) calculated to be of particular importance to the rate. The states' spin, corresponding to *s*-waves, and width meant that the high energy tail of the subthreshold state was expected to extend above threshold and provide substantial interference with the upper $1/2^+$ state across the nova temperature range. The first observation of the high energy broad $1/2^+$ state was made two years later in 2009 by Dalouzy *et al.* [63] using the inelastic scattering of protons via inverse kinematics, $H(^{19}Ne,p)^{19}Ne^*(p)^{18}F$, matching width measurements well with those predicted by its mirror state in ref. [56]. Experiments over the following years by Mountford *et al.* [64] and Adekola *et al.* [55], confirmed the observation of the state with similar resonance parameters.

Until this point, reaction rate estimates had been calculated as a sum of resonant state contributions above the proton threshold. The work by Dufour & Descouvemont was the first forray into the study of subthreshold resonances, which was continued later by Adekola *et al.* [53, 65] in 2011 with the first observation of an $l = 0$ proton transfer at $E_{c.m.} = -122$ keV, using a (d,p) transfer reaction to populate ^{19}Ne states. The spin was indicative of a $1/2^+$ or $3/2^+$ state (spins of particular importance to the rate) and as such, carried implications that resonances just above threshold contributed far less than previously thought. A study by Laird *et al.* [52] a year later measured resonances above and below the threshold with a very high energy resolution utalising the well established

(^{3}He,t) charge exchange reaction. A number of results arose from this experiment that changed the landscape of the ^{19}Ne nucleus significantly. Firstly, the important 8 and 38 keV doublet states were found to be a triplet of states with $E_{c.m.} = 5$, 29 and 48 keV. Secondly, Distorted Wave Born Approximation (DWBA) analysis showed that the 5 keV resonance was spin $3/2^-$ (in agreement with the new assignment from ref. [53]) and the 48 keV was $5/2^-$, throwing into question the $3/2^+$ mirror assignments in the region. Thirdly, the subthreshold resonance at $E_{c.m.} = -122$ keV was observed clearly, however, no low-spin assignments could be made to the data matching the $l = 0$ transfer from Adekola. Other subthreshold states were also measured below the -122 keV state that angular distributions suggested could be $3/2^+$ spin and thus be candidates for the mirror $3/2^+$ states.

The last direct reaction measurement of ^{18}F(p,α) to be performed was by Beer *et al.* [66] in 2011. As well as measuring cross sections between the 330 keV and 665 keV

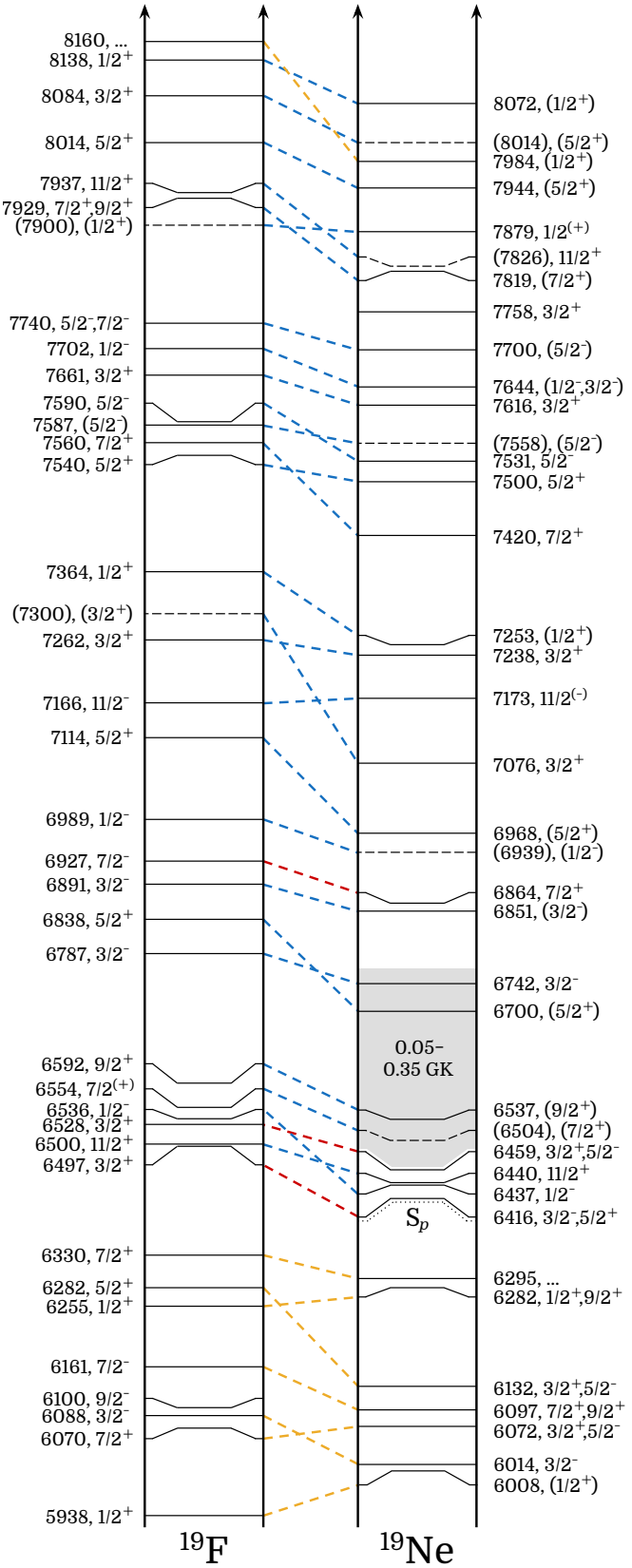

Figure 1.9: Analogue state assignments for ^{19}F/^{19}Ne. Red lines are broken assignments and yellow are new suggestions from this work.

resonances, the resonance strengths of both were measured and agreed well with those by Bardayan. Crucially, however, a beam energy of $E_{c.m.} = 250$ keV was used to perform the lowest energy measurement to date with the intention of constraining the interference terms dominating the rate uncertainty at that energy. After 155 hours of observation, two counts were recorded with no background. The large error[1] associated with the cross section meant that the reaction rate remained relatively unconstrained.

Unmentioned thus far, the $^{18}F(p,\gamma)$ reaction rate ratio is known to affect the final abundance of the γ-ray observable ^{18}F, though to a lesser extent than the (p,α) reaction [36]. The only measurement of the reaction to date was performed by Akers *et al.* [54] in 2013. A week of continuous beam time yielded two events for on resonance measurements at $E_{c.m.} = 665$ keV. With its associated error[2], the resonance strength was found to be over an order of magnitude weaker than previously thought, rendering the 665 keV resonance insignificant to the $^{18}F(p,\gamma)$ reaction rate. Even with its lower contribution to the destruction of ^{18}F, sensitivity studies [69] have shown final abundances to vary by a factor of two from the current uncertainty in the $^{18}F(p,\gamma)$ reaction rate.

The year 2015 saw three experiments conducted with relevance to ^{19}Ne resonances in novae. The first was by Cherubini *et al.* [62] using the Trojan horse method to identify two unobserved states at $E_{c.m.} = 126$ keV and 556 keV, though neither are expected to contribute to the reaction rate. The second experiment by Bardayan *et al.* [61] performed a re-measurement of angular distributions from the subthreshold -122 keV resonance using the $^{20}Ne(p,d)^{19}Ne$ transfer reaction. The state was found to have a strong s-wave transfer consistent with the state's original assignment of $J^\pi = 1/2^+$ and in clear contrast to the measurement by Laird. A solution was proposed in the third experiment by Parikh *et al.* [57] using $(^3He,t)$ reactions to populate ^{19}Ne resonances. Achieving a very high energy resolution, fits made to the data showed the -122 keV subthreshold state to either be a broad state or a doublet. The existence of two states could explain the difference in spin assignments if each state were populated preferentially by the two different reactions. The experiment also found evidence for a previously missing broad $3/2^-$ state at $E_{c.m.} = 440$ keV. A brief analysis of the cross section (and reaction rate) was also performed by Bardayan in ref. [61] using the more recent measurements and assuming $J^\pi = 1/2^+$ for

[1] Calculated using a method for low statistics from ref. [67].
[2] Error calculations taken from the technique outlined in ref. [68].

the −122 keV resonance (see Fig. 1.10). The uncertainty in the rate was found to be less than a factor of 5 giving an uncertainty in ejected ^{18}F mass of a factor of 2.

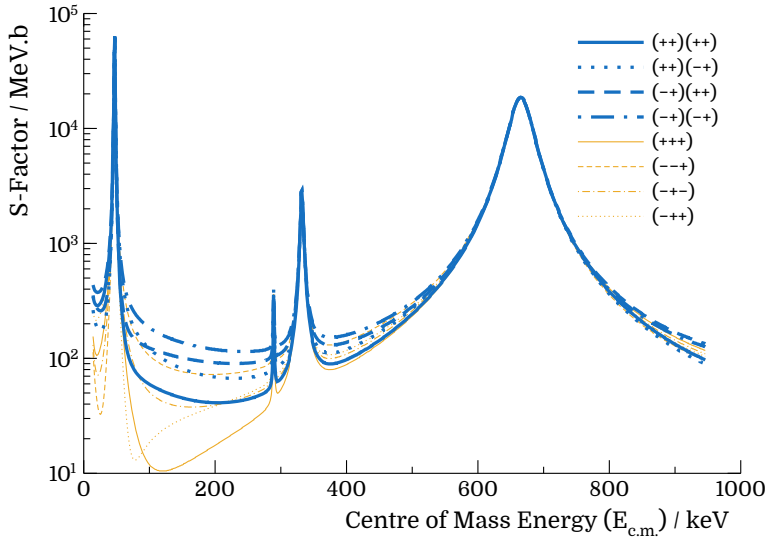

Figure 1.10: The most recent cross section calculation by Bardayan *et al.*. The first four terms are assuming the −122 keV to be $J^\pi = 1/2^+$, the last four terms are assuming $J^\pi = 3/2^+$. Figure taken from ref. [61].

The final experiment to be discussed is that from Boulay *et al.* [60], performed last year (2016), in which the first observation of the broad $1/2^+$ subthreshold state, postulated by Dufour & Descouvemont, was made. The experiment used inelastic proton scattering in inverse kinematics (similar to those used by Dalouzy) and detected the decay particles from populated ^{19}Ne states. The existence of the subthreshold state adds further complication to the ^{18}F(p,α) direct capture contribution, owing to the additional interference between s-wave resonances, and is expected to increase the reaction rate uncertainty from that calculated in ref. [61].

1.5 Motivation for the Present Work

^{19}Ne resonances still retain significant uncertainties relating to their energy, width and spin despite their continuous study over the past four decades. As a result, calculations of the reaction governing the destruction of ^{18}F during a novae outburst vary wildly in their rate making abundance estimates unobtainable without substantial error. Experimentally, direct reactions are still difficult to conduct owing to the low cross sections when measuring at astrophysical temperatures (see section 2.2.1) and to the current intensity of radioactive

^{18}F beams. The purpose of this study is therefore to utilise indirect methods to populate resonances of astrophysical importance, bypassing the Coulomb barrier, and measure the parameters of interest.

Of particular importance are parameters taken solely from ^{19}F mirror states such as partial widths of near threshold resonances. Their proximity to the proton binding energy makes measurements of p partial widths through proton branching ratios difficult, even when using indirect population methods. A strong measurement with constrained errors on the alpha-particle width, however, could indirectly yield a limit on the proton width sufficient for improving reaction rate calculations. Given its potential impact on the reaction rate, the -122 keV resonance (in dispute by Laird [52], Bardayan [61] and Parikh [57]) must be investigated further through a measurement of the state's spin-parity.

Of equal importance to the measurement of new parameters, is an understanding of the existing parameters' uncertainties and their impact on the reaction rate. Knowledge of the rate's sensitivity to each resonance can help guide future efforts towards the assessment of those states with a greater impact on the astrophysical reaction rate of interest. Therefore, in addition to an experimental undertaking, this work's focus was also on the evaluation of measurements performed within the last decade, since the publication of Nesaraja [50]. In particular, the discovery of the postulated broad $1/2^+$ resonance raises many questions about the contribution direct capture now plays in the ^{18}F(p,α) rate, given the potential for interference between resonances. The observation of new resonances by Cherubini [62] and Parikh [57] have yet to be investigated in conjunction with direct reaction data and may provide constraint on these interference terms.

Despite its proven influence on the final abundance of ^{18}F [69], the ^{18}F(p,α) reaction is known to proceed three orders of magnitude faster than that of the ^{18}F(p,γ) reaction at novae temperatures [36]. Therefore, the study of this work has only been on the former of the two reactions. The results from an experiment using the ^{19}F(^{3}He,t)^{19}Ne charge exchange reaction, designed to investigate the α-particle and p widths of ^{19}Ne resonances, will be discussed in Chapters 3 and 4. Additionally, cross section calculations based on the entrance and exit channels of the ^{18}F(p,α)^{15}O reaction are outlined in Chapter 5.

Chapter 2

Theory

2.1 Nuclear Reaction Theory

The aim of this work was to investigate the rate of ^{18}F destruction through the indirect study of resonant proton capture. To understand how the population and decay of nuclear states in ^{19}Ne through ^{19}F(^{3}He,t) can be used to predict their behaviour when populated by ^{18}F(p,α), it is necessary to outline the physical theories and mechanisms behind nuclear reactions. It is also appropriate to discuss how reactions measured under laboratory conditions can be translated into their stellar counterparts. The following sections therefore describe basic nuclear structure properties and their application to interactions between nuclei.

2.1.1 Cross Sections

The probability of reaction between two colliding particles is represented by the cross section (σ) of the two particles and is defined (in terms of a laboratory experiment) as

$$\frac{N_r}{t} = \frac{N_b}{t}\frac{N_t}{A}\sigma \ , \tag{2.1}$$

where N_r/t is the reactions per unit time, N_b/t is the number of beam particles per unit time and N_t/A is the target particles per unit area. The cross section has units of area and can be thought of, classically, as the geometrical surface presented by the target to the incoming beam. The discrepancy observed between actual geometrical areas and their

cross section measurements suggest that it is more appropriate to be described as the probability of reaction.

Due to experimental constraints, it is rarely possible to measure the products of a reaction at all angles. Instead, the differential cross section measures the flux of reactants for a given solid angle $d\Omega$. The total cross section can be extracted by integrating over the total solid angle

$$\sigma = \int_{4\pi} \frac{d\sigma(\theta)}{d\Omega} d\Omega \ , \tag{2.2}$$

The shape of the differential cross section can provide information on the mechanism of the reaction, such as the transfer of orbital momentum. This is discussed in greater detail in section 2.4.

2.1.2 Particles as Waves

The interactions between reacting nuclei through the strong force are complex and not well understood, requiring approximations to be made to describe observations seen through experiment. Direct reactions (such as the charge exchange reaction in this work) can be modelled using scattering theory where incoming beam is described by a plane wave travelling, as is customary, in the z-direction with momentum $\hbar k$,

$$\psi^{\text{beam}} = Ae^{ikz} \ , \tag{2.3}$$

where A is the peak amplitude and k is the wavenumber. The wave scatters off a central potential V produced by the target particle (Fig. 2.1) and the outgoing wavefunction is a superposition of the incoming plane wave and the scattered radial wave,

$$\psi_T = A\left[e^{ikz} + f(\theta)\frac{e^{ikr}}{r}\right] \ . \tag{2.4}$$

Here, e^{ikr} is the scattered radial wave (following the inverse square law) and $f(\theta)$ is the scattering amplitude. The incoming and outgoing waves consist of a stream of particles and are considered to be in a steady state[1]. Their current densities, $j_{\text{in/out}}$, can be substituted

[1]Described by the time independent Schrödinger equation.

for terms in eq. 2.1 to show that the cross section (probability of reaction) is equivalent to the square of the scattering amplitude.

$$\frac{d\sigma}{d\Omega} = \frac{j_{\text{out}} r^2}{j_{\text{in}}} = |f(\theta)|^2 \quad . \tag{2.5}$$

A partial wave analysis[1] shows the difference between the scattered and unscattered wave functions at large distances (such as the position of a detector). To maintain an equilibrium between incoming flux and outgoing flux, the only change scattering can make is to the relative phase of the two waves. The phase shift (δ_l) is a result of the different dependence on r when the scattered wave is close enough to the central potential such that $V \neq 0$. This implies that all the information on the parameters of the potential is carried by the scattering amplitude and, by extension, the phase shift.

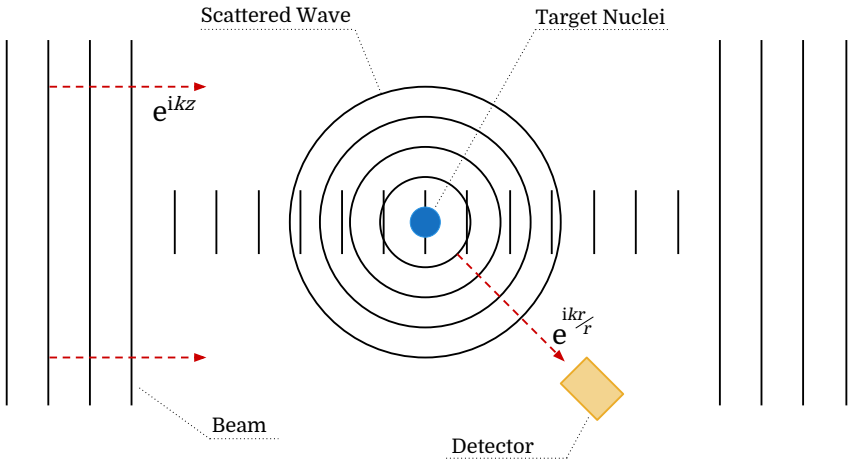

Figure 2.1: Nuclear reaction described by a wave scattering off a central potential. The detector observes a superposition of the beam and scattered particle wave-functions.

2.1.3 Resonances

A rapid rise in phase shift is often observed in reaction cross section measurements plotted as a function of energy, identified by an equivalent rapid variation in cross section. The changes above the smoother dependency on energy, such as that from Coulomb repulsion, are attributed to resonances. A compound nucleus may continue to exhibit discrete quantum states above the separation energy of the reacting nuclei where the interacting

[1] Each wave is decomposed into its angular momentum constituents, l, known as partial waves.

particles are trapped within a potential barrier (Fig. 2.2) for a period of time τ. The phase shift observed is a measure of the time delay experienced by the scattered wave packet.

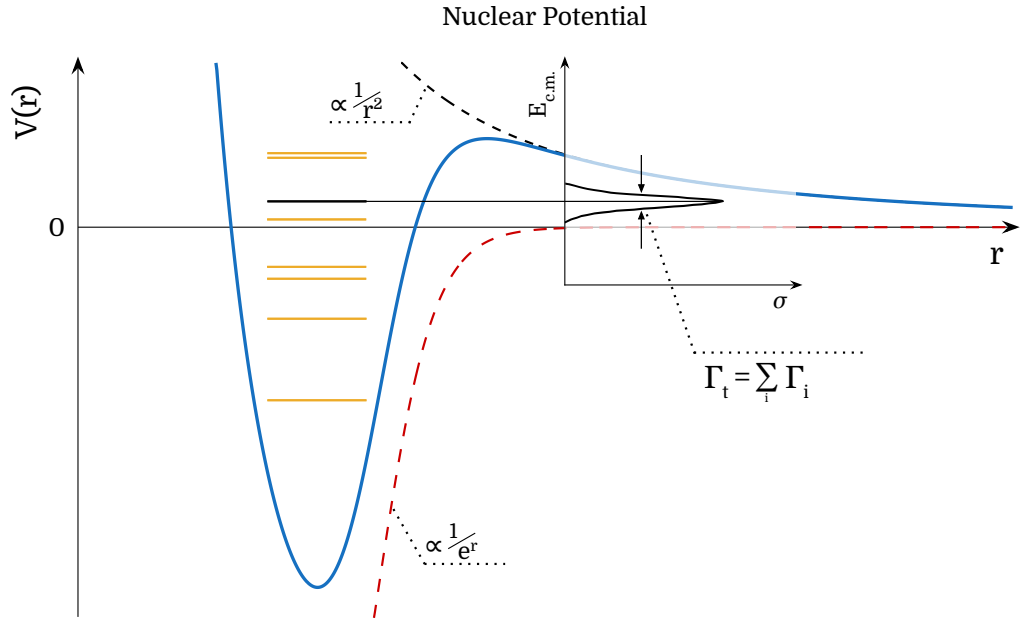

Figure 2.2: Potential plotted as a function of radius from a compound nucleus. The total nuclear potential (shown in blue) is the product of the attractive Woods-Saxon potential in red (generated by the strong force) and the repulsive centripetal force in black (caused by the spin of the nucleus). Resonances lie outside the attraction of the nuclear force but remain trapped by a second potential barrier.

Resonances are characterised by their total spin J and parity $\pi = \pm 1$ much like their bound state counterparts. Their energy E_r[1] is distributed in probability by its width parameter Γ which is related to the state's lifetime by

$$\Gamma_t = \sum_i \Gamma_i = \frac{\hbar}{\tau} \ , \tag{2.6}$$

where Γ_i are the partial widths and are directly proportional to the decay probabilities for the resonance. The width of a resonance depends on a number of factors including the penetrability P_l of a particle to tunnel through the Coulomb or angular momentum potential barriers (discussed in section 2.2.1), the spectroscopic factor S that describes the configuration of the nucleons and the single-particle reduced width θ_{sp} containing the probability that the decaying particle appears at the boundary of the compound nucleus.

[1]Also denoted as $E_{\text{c.m.}}$ in this work representing the difference from separation energy in the $^{18}\text{F} + p$ centre of mass frame.

The partial width is therefore given by

$$\Gamma_i = \frac{2\hbar^2}{\mu R^2} P_l C^2 S_i \theta_{sp}^2 \ , \tag{2.7}$$

where $\mu = \frac{m_a m_A}{m_a + m_A}$ is the reduced mass, R is the interaction radius and C is the Clebsch-Gordon coefficient. The partial width describes, in part, the probability of reaction through that channel (see section 2.2.2).

The increase in phase shift over a resonance is a superposition of the resonance's phase shift,

$$\delta_{\text{res}}(E) = \tan^{-1}\left(\frac{\Gamma/2}{E_r - E}\right) \tag{2.8}$$

and some background phase shift $\delta_{\text{bg}}(E)$ that changes more slowly. If $\delta_{\text{bg}}(E) \simeq 0$ then the resonance is represented by a clear peak known as a pure Breit-Wigner resonance (discussed in more detail in section 2.2.2). If $\delta_{\text{bg}}(E) \neq 0$ then the two phase shifts interfere with each other to produce destructive patterns that reduce the measured cross sections (see Fig. 2.3).

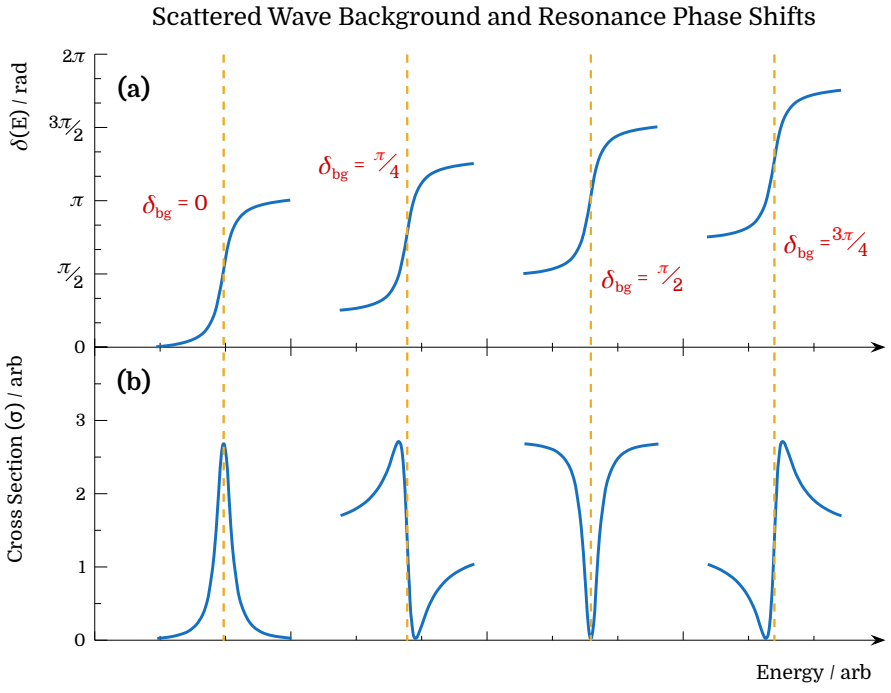

Figure 2.3: Figure depicting the phase shift caused by a resonance (panel **(a)**) and its impact when in combination with a background phase shift (panel **(b)**). Resonances can interfere constructively ($\delta_{bg} = 0$), destructively ($\delta_{bg} = \pi/2$) or anywhere in between. Adapted from Fig. 3.3 in ref. [70].

It is this interference that attributes to the reaction rate uncertainty observed by de Séréville *et al.* [43] (see Fig. 1.7). Interferences only occur for background phase shifts in the same partial wave as that of the resonance, i.e. for similar J^{π}, as different partial waves are incoherent in their summation to form the total wave function [70].

2.2 Astrophysical Reaction Rates

The work in this thesis is focused on measuring the rate at which the ^{18}F(p,α) reaction occurs in novae. It is therefore necessary to address the behaviour of nuclei in an astrophysical environment to understand its influence on the probability of reaction. The fusion reaction rate between two particles a and A is given by

$$R_{aA} = n_a n_A v\sigma(v) \ , \tag{2.9}$$

where $n_a n_A$ are the number densities of each particle and v is the relative velocity between the two. Unlike a monoenergetic beam, particles in an astrophysical environment have a distribution of velocities dependent on the temperature. The probability of a relative velocity between the two particles between v and $v + dv$ must be accounted for in eq. 2.9 to produce

$$\langle \sigma v \rangle = \int P(v) v \sigma(v) dv \ . \tag{2.10}$$

The probability $P(v)$ within a stellar temperature T can be described using the Maxwell-Boltzmann distribution[1],

$$P(v)dv = 4\pi v^2 \left(\frac{\mu}{2\pi k_b T} \right)^{3/2} \exp\left(\frac{-\mu v^2}{2k_b T} \right) dv \ , \tag{2.11}$$

where μ is the reduced mass of the system and k_b is the Boltzmann constant. As most nuclear experiments are measured in energy, it is more convenient to convert the integration variable using the non-relativistic relationship $E = {}^1/_2 \mu v^2$. Equations 2.10 and 2.11 can then be combined to produce the reaction rate for the particle pair

$$\langle \sigma v \rangle = \left(\frac{8}{\pi \mu} \right)^{1/2} \frac{1}{(k_b T)^{3/2}} \int_0^{\infty} \sigma(E) E \ \exp\left(-\frac{E}{k_b T} \right) dE \ , \tag{2.12}$$

[1]Temperatures in stellar environments mean relativistic effects are negligible.

commonly multiplied by Avogadro's number N_A and expressed in terms of $\mathrm{cm^3 mol^{-1} s^{-1}}$. The equation's use lies in its ability to calculate the rate of reaction in stellar environments using cross section measurements made under laboratory conditions.

2.2.1 Gamow Window

Before nuclei separation is small enough to allow interaction via the strong force ($r \simeq 10{-}15$ m), charged particles will feel a repulsive force from the Coulomb potential,

$$V_C(r) = \frac{Z_a Z_A q^2}{4\pi\epsilon_0 r} \ , \tag{2.13}$$

where Z is the nuclear charge, q is the elementary charge and ϵ_0 is the permittivity of free space. The fusion of nuclei a and A is inhibited by the magnitude of the repulsive potential from the Coulomb force and, under classical conditions, would require a stellar temperature several orders of magnitude higher than those observed in order to overcome the barrier. However, a quantum mechanical approach to the nuclei finds that the position of a particle r is a function of probability (given by the square of its wavefunction $|\psi(r)|^2$). There is therefore a finite chance that the particle's position has surpassed the Coulomb barrier and feels the stronger attractive force of the nuclear potential.

The penetrability of a particle through the barrier can be calculated by considering its transmission probability through a small section (δr) of a square well potential. As δr tends to 0, the total transmission coefficient[1] is given by the product of each section

$$T = \exp\left(-\frac{2}{\hbar}\sqrt{2m}\int_{r_0}^{r_c}\sqrt{\frac{Z_a Z_A q^2}{r} - E}\ dr\right) , \tag{2.14}$$

where r_0 is the radius of the square well potential at which the barrier is highest, and r_c is the classical turning point where the potential is equal in energy to the incoming particle. The integral can be solved analytically [5] and, at very low energies where $E_a \ll E_c$, approximated to

$$T = \exp\left(-\frac{2\pi}{\hbar}\sqrt{\frac{m}{2E}}Z_a Z_A q^2\right) = e^{-2\pi\eta} \ , \tag{2.15}$$

[1] Calculated for an s-wave with no orbital momentum barrier.

where η is the Sommerfeld parameter. This approximation of the transmission coefficient (eq. 2.15) is referred to as the Gamow factor.

The reaction cross section has a high energy dependence from both the transmission through the potential barrier (eq. 2.13) and from its characterisation as a wave[1] (eq. 2.4). The cross section can therefore be expressed as

$$\sigma(E) = \frac{1}{E} e^{-2\pi\eta} S(E) \ , \tag{2.16}$$

where $S(E)$ is known as the astrophysical S-factor and exhibits a much weaker energy dependence in comparison to the other terms. The S-factor can be considered to represent the intrinsically nuclear part of the reaction probability and is a more useful term for extrapolating measured cross sections down to astrophysical energies where small changes in energy can yield reaction probability variations over many orders of magnitude.

With the definition of the S-factor, the reaction rate from eq. 2.12 can be re-written as

$$\langle \sigma v \rangle = \left(\frac{8}{\mu\pi} \right)^{1/2} \frac{1}{(k_b T)^{3/2}} \int_0^\infty S(E) \exp\left[-\frac{E}{k_b T} - \left(\frac{E_G}{E} \right)^{1/2} \right] dE \ , \tag{2.17}$$

where E_G is the Gamow energy given by

$$E_G = 2\mu \left(\frac{\pi Z_a Z_A q^2}{\hbar} \right)^2 \ . \tag{2.18}$$

The two exponential terms in eq. 2.17 arise from the Maxwell-Boltzmann distribution of energies (eq. 2.11) and the Coulomb barrier penetrability (eq. 2.15) and have been plotted in Fig. 2.4. It can be seen that there are a very low proportion of particles with high energy and that particles with low energy do not have a sufficient chance of penetrating far enough through the Coulomb barrier to allow interaction between the nuclear surfaces. The balance between these two factors gives rise to the Gamow window where reaction probability is at its highest (also shown in Fig. 2.4), calculated as a convolution of the two functions.

[1] The de Broglie wavelength of a particle is proportional to its energy ($\lambda \propto \frac{1}{\sqrt{E}}$)

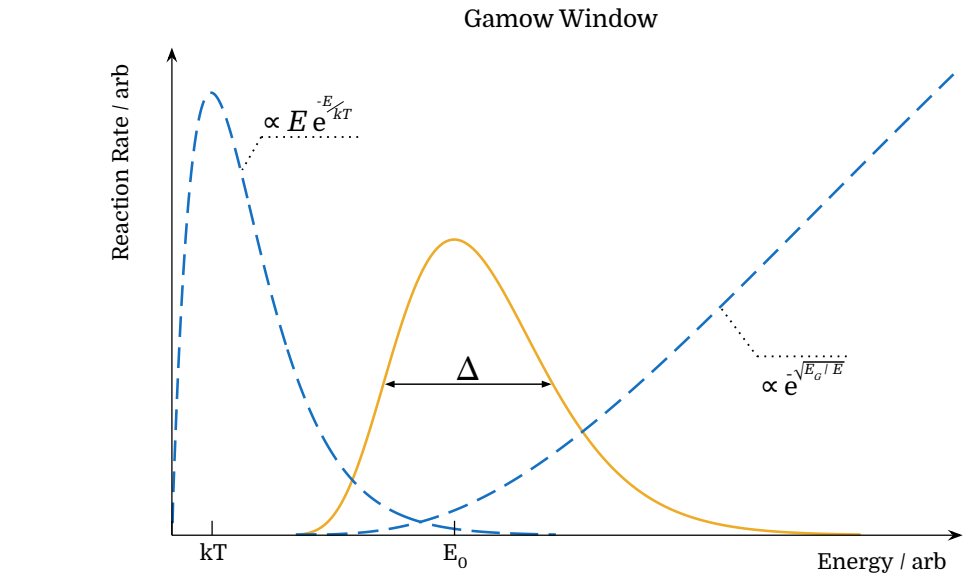

Figure 2.4: Gamow window, centred on E_0 and amplified for the purpose of this figure, representing the probability of reaction in a stellar environment.

The reaction rate of nuclei are only significant about the Gamow peak and, if approximated as a Gaussian, the position and width can be calculated by

$$E_0 = \left(\frac{E_G k_b^2 T^2}{4}\right)^{1/3} \qquad (2.19) \qquad \text{and} \qquad \Delta = \frac{4}{\sqrt{3}}\sqrt{E_0 k_b T} \qquad (2.20)$$

respectively.

2.2.2 Resonant Reactions

Thus far, calculations of the astrophysical reaction rate have assumed a direct capture of a projectile into bound states of the compound nucleus (with the assumption of γ-ray emission as the resulting nucleus finds its lowest energy). It has already been discussed (section 2.1.3) that cross sections do not always vary smoothly with energy and that capture at resonant energies exhibit rapid changes in cross section. It is resonant capture that dominate the majority of thermonuclear reactions as their presence (even at energies outside the Gamow window) can increase the probability of reaction by several orders of magnitude. It is also the contribution of resonances to the reaction rate that is of interest in this work as the interplay between ^{19}Ne resonances produce significant uncertainty in the ^{18}F(p,α) cross section.

Narrow Resonance

The cross section for a reaction proceeding through an incoming i and outgoing f channel of a narrow, isolated resonance is described by the Breit-Wigner equation [71],

$$\sigma_{BW}(E) = \frac{\lambda^2}{4\pi}\frac{2J+1}{(2J_a+1)(2J_A+1)}\frac{\Gamma_i\Gamma_f}{(E_r-E)^2+(\Gamma/2)^2} \ , \tag{2.21}$$

where λ is the de Broglie wavelength (of the reduced mass), E_r is the resonance energy, $\Gamma_{i,f}$ are the partial widths of the channels, Γ is the total width of the resonance, $J_{a,A}$ are the spins of the reacting particles and J is the spin of the resonance. Substituting σ_{BW} from eq. 2.21 for $\sigma(E)$ in eq. 2.12 yields

$$\langle\sigma v\rangle = \frac{\sqrt{2\pi}\hbar^2}{(\mu k_b T)^{3/2}}\left[\frac{2J+1}{(2J_a+1)(2J_A+1)}\right]\int_0^\infty \frac{\Gamma_i\Gamma_f}{(E_r-E)^2+(\Gamma/2)^2}\exp\left(-\frac{E}{k_bT}\right)dE \ . \tag{2.22}$$

Assuming a narrow resonance where $\Gamma \ll E_r$ such that the energy distribution and penetrability change very little across the resonance, they may be evaluated at $E = E_r$ to re-write the cross section as

$$\langle\sigma v\rangle = \left(\frac{2\pi}{\mu k_b T}\right)^{3/2}\hbar^2(\omega\gamma)\exp\left(\frac{E_r}{k_bT}\right) \ , \tag{2.23}$$

where $\omega\gamma$ is referred to as the resonance strength and equates to

$$\omega\gamma = \left[\frac{2J+1}{(2J_a+1)(2J_A+1)}\right]\left[\frac{\Gamma_i\Gamma_f}{\Gamma}\right] \ . \tag{2.24}$$

The resonance strength and energy are the principal parameters that determine a resonant reaction rate. Eq. 2.23 can be summed for each resonance if several contribute to the reaction.

Broad Resonance

Unlike the narrow treatment of a resonance, broad resonances are wide enough such that the energy dependence of the cross section must be accounted for and cannot be approximated as in eq. 2.23. Reaction rates cannot be solved analytically and instead must be calculated numerically using the Breit-Wigner formula [5],

$$\sigma_{BW} = \frac{\pi\hbar^2}{2\mu E}\omega\gamma\frac{P_i(E)}{P_i(E_r)}\frac{\Gamma_f(E)}{\Gamma_f(E_r)}\frac{\Gamma(E_r)}{(E_r - E)^2 + (\Gamma(E)/2)^2} \ , \tag{2.25}$$

where the penetrability of the entrance channel P_i must be calculated using solutions of the Schrödinger equation, calculated with a Coulomb potential, known as the regular and irregular Coulomb functions.

2.3 R-Matrix

The Reaction matrix (R-Matrix) theory is a mathematical formalism that is used to parameterise reactions occurring through the formation of a compound nucleus and relate them to the observed cross sections and angular distributions [72]. Referring back to the scattering approximation of a nuclear reaction, the formalism separates the configuration space of the problem into two regions either side of a boundary a_c,

$$a_c = 1.3(A_a^{1/3} + A_A^{1/3}) \ , \tag{2.26}$$

known as the channel boundary where A_a and A_A are the mass numbers of the particle pair. The 'external' region corresponds to the many different reaction possibilities (channels) for forming or destroying the compound nucleus (in the case of this work, ^{19}Ne). The 'internal' region consists of the compound nucleus itself separated from the external at a fixed radius a_c. Fig. 2.5 shows a rough illustration of the boundary between the internal nucleus and the external particle configurations.

As described in section 2.1.2, the external region ($r > a_c$) can be described by the superposition of an incoming plane wave and the scattered radial wave. For the purpose of the R-matrix formalism eq. 2.4 can be written as

$$\psi_l = \left[I_l - e^{2i\delta_l}O_l\right] = \left[I_l - U_lO_l\right] \ , \tag{2.27}$$

where I and O are the incoming and outgoing waves from the boundary respectively and U is the collision function. The incident orbital angular momentum of the system is denoted by l. The phase shift (or scattering function) contains the information on the scattering

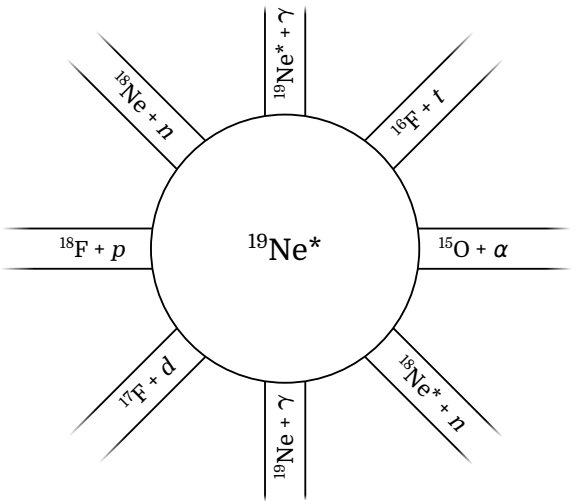

Figure 2.5: Schematic diagram of the compound nucleus volume defined by the channel boundary. Possible reaction channels for the ^{19}Ne nucleus have been shown. Adapted from Fig. 4 in ref. [73].

potential (the compound nucleus) but must first be related to the wavefunction inside the channel boundary.

The internal region ($r < a_c$) contains a complete set of stationary states that satisfy the hamiltonian $HX_\lambda = E_\lambda X_\lambda$ where E_λ, are the eigenvalues and X_λ are the eigenvectors for state λ. A boundary condition, b, relates the stationary states with the quasi-stationary resonances at the boundary a_c, such that

$$\frac{dX_\lambda}{dr} + bX_\lambda|_{r=a_c} = 0 \ . \tag{2.28}$$

The internal wavefunction can be described by

$$\psi(r) = \sum_\lambda C_\lambda X_\lambda(r) \ , \tag{2.29}$$

where

$$C_\lambda = \int_0^a X_\lambda^*(r)\psi(r)dr \ . \tag{2.30}$$

The logarithmic derivative of eq. 2.29 evaluated at the boundary $r = a_c$, yields a Fourier series with stationary states X_λ and

$$C_\lambda = \frac{\hbar^2}{2\mu a_c}\frac{X_\lambda^*(a_c)}{(E_\lambda - E)}\left[\psi'(a_c) - b\psi(a_c)\right] \ . \tag{2.31}$$

Combining eq. 2.29 and 2.31, the logarithmic derivative can be written as

$$\frac{\psi'(a_c)}{\psi(a_c)} = \frac{(1-bR)}{R} \ , \tag{2.32}$$

where R is the reaction function (R-function), equal to

$$\begin{aligned} R &= \frac{\hbar^2}{2\mu} \sum_\lambda \frac{|\psi_\lambda(a_c)|^2}{E_\lambda - E} \ , \\ &= \sum_\lambda \frac{\gamma_\lambda^2}{E_\lambda - E} \ . \end{aligned} \tag{2.33}$$

where γ^2 is known as the reduced width. Equating the logarithmic derivatives for the external wave function (eq. 2.27) and internal wave function relates the collision function U (and the cross section measurements) with the R-function (and the resonance parameters),

$$U = O^{-1}(1-RL)^{-1}(1-RL^*)I \ , \tag{2.34}$$

where L is defined as $L = O'O^{-1} - b$. So far the formalism has only been presented for a single reaction channel. For the many channel example in Fig. 2.5 the formalism is extended to use matrix notation. The R-function is rewritten as

$$R_{cc'} = \sum_\lambda \frac{\gamma_{\lambda c}\gamma_{\lambda c'}}{E_\lambda - E} \ , \tag{2.35}$$

and known as the R-matrix where the index set $c = \{asvlm\}$ denote the channel, channel spin, channel spin component, orbital angular momentum and orbital angular momentum component for the entrance and exit ($'$) channels.

2.3.1 Subthreshold Resonance

Bound states can be considered solutions to the Schrödinger equation for negative energies that correspond to positive imaginary wave numbers [70]. Depending on the parameters of the state, their high energy tails can occasionally extend beyond the separation energy and contribute to resonance capture. The strength of the tail can be described using the asymptotic normalisation coefficient (ANC) of the Whittaker function,

$$W_{-\eta_I, l+1/2}(-2k_I r) \simeq e^{-k_I r + \eta_I \ln(2k_I r)} \ , \tag{2.36}$$

where η_I is the imaginary Sommerfeld parameter. Importantly, the ANC can be related to the reduced width of the state, necessary for the R-matrix formalism, via

$$\gamma^2 = \left(\frac{\hbar^2}{2\mu a_c}\right) \frac{C^2\, W(-2ka_c)^2}{1 - C^2 \int_{a_c}^{\infty} |W(-2kr)|^2 dr} \ , \tag{2.37}$$

where C is the ANC.

2.4 Angular Distributions

From eq. 2.24 it can be seen that the strength of a resonance is dependent on both its spin and its partial widths, and it was these two parameters that were measured for this work via the ^{19}F(^{3}He,t)^{19}Ne*(α)(p) reaction. The emission strength of decay products from populated states in ^{19}Ne is strongly dependent on the angle of emittance. The variation in decay products (or differential cross section) is governed by the angular momentum transferred to the decay particle which, in turn, is decided by the spin J of the originating state.

Whilst many reaction studies have been performed observing the correlation of γ rays, only a few have measured the emission of particle decay after a similar method of population used in this work. The theoretical foundations have only been dealt with within an article by Pronko & Lindgren [74] and it is to this formalism that the following description adheres. The reaction in this work of type A(a,b)B(c)C is outlined in Fig. 3.1 and corresponds to the same case in the aforementioned article. Within this framework, the angular distribution of particle c is governed by the following,

$$W(\theta) = \sum_{mll'skr} P(m)\, A(Jll'smk)\, (2 - \delta_{ll'})\, X^r(ll')\, Y(s)\, P_k \cos(\theta) \ , \tag{2.38}$$

where

$$A(Jll'smk) = (-1)^{|s-m|}\, \hat{l}\, \hat{l'}\, \hat{J}^2\, \langle ll'00|k0\rangle\, \langle JJm - m|k0\rangle\, W(lJl'J; sk) \ . \tag{2.39}$$

The terms of equations 2.38 and 2.39 are as follows,

***P*(*m*)** This represents the probability of populating the magnetic substates of the recoil state. The quantum number m can only assume values between $-J$ and J, however, substates are limited by the spin of the target, ejectile and exit channel.

$\boldsymbol{X^r(ll')}$ Depending on the channel spin, the decay particle can transfer one or two values of orbital momentum l. Due to conservation of parity $l' = l \rightarrow l + 2$. The term $X^r(ll')$ represents the mixing between these values.

$\boldsymbol{\delta_{ll'}}$ Dirac function equivalent to 0 unless $l = l'$

$\boldsymbol{Y(s)}$ Where s is the exit channel spin, $Y(s)$ represents the contribution of each spin.

$\boldsymbol{P_k \cos(\theta)}$ These are solutions to the Legendre polynomial equation of order k where θ is the angle of emission in the centre of mass frame. For reasons of symmetry, only even values of k are used and the summation is truncated at a maximum value of k where $k_{\max} = 2l$.

$\boldsymbol{\hat{l}, \hat{l}'}$ and $\boldsymbol{\hat{J}^2}$ are the angular momentum operators for l, l' and J, the magnitude of which are equivalent to $\sqrt{l(l+1)}$ $\sqrt{l'(l'+1)}$ and $J(J+1)$ respectively.

$\boldsymbol{\langle ll'00|k0\rangle}$ and $\boldsymbol{\langle JJm - m|k0\rangle}$ are Clebsch-Gordan coefficients that can be represented by the Wigner $3-j$ symbol [71]

$$\begin{pmatrix} a & b & c \\ \alpha & \beta & \gamma \end{pmatrix} = (-1)^{a-b-\gamma}(2c+1)^{-1/2}\langle ab\alpha\beta|c-\gamma\rangle \ . \tag{2.40}$$

$\boldsymbol{W(lJl'J;sk)}$ is the Racah coefficient and can be represented by the Wigner $6-j$ symbol

$$\begin{Bmatrix} a & b & e \\ d & c & f \end{Bmatrix} = (-1)^{a+b+c+d} W(abcd;ef) \ . \tag{2.41}$$

The parameters above are all constant coefficients and the shape of the decay distribution is governed only by the Legendre polynomials. The order of the polynomial is related to the orbital momentum transferred and, therefore, measurements of the decay with respect to their angular distribution yield information on the spin of the state.

2.4.1 Alpha-Particle Decay

The states in ^{19}Ne above 3528 keV can decay via an α-particle ($J^\pi = 0+$) to the ground state in ^{15}O ($J^\pi = 1/2^-$). The channel spin is therefore calculated to be

$$s = J_{^{15}\mathrm{O}} + J_\alpha \ = \ \frac{1}{2} \pm 0 \ = \ \frac{1}{2} \ .$$

Only a single channel spin is possible and therefore $Y(s) = 1$ and the sum over s is removed from eq. 2.38. Conservation of angular momentum and parity produce the following two relationships,

$$J = l \pm s \qquad \text{and} \qquad \pi_f = (-1)^l \pi_i \ .$$

Table 2.1 summarises the relationship between the orbital angular momentum l transferred and the spin parity J^π of the state in ^{19}Ne. As shown in the table, each value of J^π corresponds to a single value of l and therefore $X^r(ll') = 1$ and can be removed from eq. 2.38. Table 2.1 also shows the limitation of such measurements as only the l-value can be determined experimentally, leaving some ambiguity in the J^π of the state for all but the isotropic distribution.

$\boldsymbol{l}$	$\mathbf{J^\pi}$	$\boldsymbol{k_{\max}}$
0	$\frac{1}{2}^-$	0
1	$\frac{1}{2}^+$ $\frac{3}{2}^+$	2
2	$\frac{3}{2}^-$ $\frac{5}{2}^-$	4
3	$\frac{5}{2}^+$ $\frac{7}{2}^+$	6
4	$\frac{7}{2}^-$ $\frac{9}{2}^-$	8
5	$\frac{9}{2}^+$ $\frac{11}{2}^+$	10

Table 2.1: Legendre polynomial orders ($k_{\max}$) and their associated spin-parity states in ^{19}Ne for α-particle decay.

The simplifications from the decay of a spin-zero particle lead to the following α-particle decay distribution

$$W_\alpha(\theta) = \sum_{mk} P(m)\, A(Jll'smk)\, P_k \cos(\theta)\ . \tag{2.42}$$

The $A(Jll'smk)$ and $P(m)$ coefficients were combined into a single free parameter when fitting the distributions (see section 4.6).

2.4.2 Proton Decay

States above 6411 keV in ^{19}Ne were also able to decay through proton emission. The spin of the proton ($J^\pi = 1/2^+$), however, leads to some further ambiguity. The spin of the exit channel is calculated as

$$s = J_{^{18}\mathrm{F}} + J_p \ = \ 1 \pm \frac{1}{2} \ = \ \frac{1}{2} \text{ or } \frac{3}{2}\ ,$$

resulting in the possibility of two values. Using the same relationships as for the α-particle decay, Table 2.2 shows the values of orbital momentum and their corresponding

spin parity states in ^{19}Ne. For a given spin, several possibilities for the orbital angular momentum, l, carried away by the proton exist. Whilst this leads to further ambiguity, a common assumption is that the p-decay occurs with the lowest orbital momentum transfer possible.

None of the terms in eq. 2.38 can be simplified and must be accounted for when fitting proton decay distributions. Like the α-particle decay before, however, all terms except the Legendre polynomials can be treated as a single free parameter, as $J^{\pi}_{^{19}\mathrm{Ne}}$ is the only property of interest in the current work.

$\boldsymbol{l}$	$\mathbf{J^{\pi}}$	$\boldsymbol{k_{\max}}$
0	$\frac{1}{2}^+$ $\frac{3}{2}^+$	0
1	$\frac{1}{2}^-$ $\frac{3}{2}^-$ $\frac{5}{2}^-$	2
2	$\frac{1}{2}^+$ $\frac{3}{2}^+$ $\frac{5}{2}^+$ $\frac{7}{2}^+$	4
3	$\frac{3}{2}^-$ $\frac{5}{2}^-$ $\frac{7}{2}^-$ $\frac{9}{2}^-$	6
4	$\frac{5}{2}^+$ $\frac{7}{2}^+$ $\frac{9}{2}^+$ $\frac{11}{2}^+$	8
5	$\frac{7}{2}^-$ $\frac{9}{2}^-$ $\frac{11}{2}^-$ $\frac{13}{2}^-$	10

Table 2.2: Legendre polynomial orders ($k_{\max}$) and their associated spin-parity states in ^{19}Ne for p decay.

Chapter 3

^{19}F(^{3}He,t)^{19}Ne Experimental Setup

3.1 Experimental Proposal

To conclude from Chapter 1, the astrophysical reaction rates for proton capture onto ^{18}F within classical nova outbursts must be known to a greater accuracy. Since direct measurements are often experimentally challenging, alternative methods must be employed to provide constraints. In section 2.3 it was shown that reaction rates can be calculated by parameterising entrance and exit channel resonances with their associated compound nucleus. The proposed experiment was therefore to perform indirect reactions to populate the ^{19}Ne compound nucleus and probe its nuclear states for their energy, widths and angular momenta.

Whilst several reactions were possible, similar experiments performed previously [36, 52, 57] have shown charge-exchange reactions to be a reliable method of populating the states of interest. A beam of ^{3}He was incident upon a target of CaF_2 to exchange a neutron for a proton producing an excited ^{19}Ne nucleus - ^{19}F(^{3}He,t)^{19}Ne (Fig. 3.1). Measurements of the branching ratios and spin-parities (J^{π}) were obtained using the excited ^{19}Ne decay products. Nuclear decay is a well described process that would allow for an accurate interpretation of the particle distributions observed.

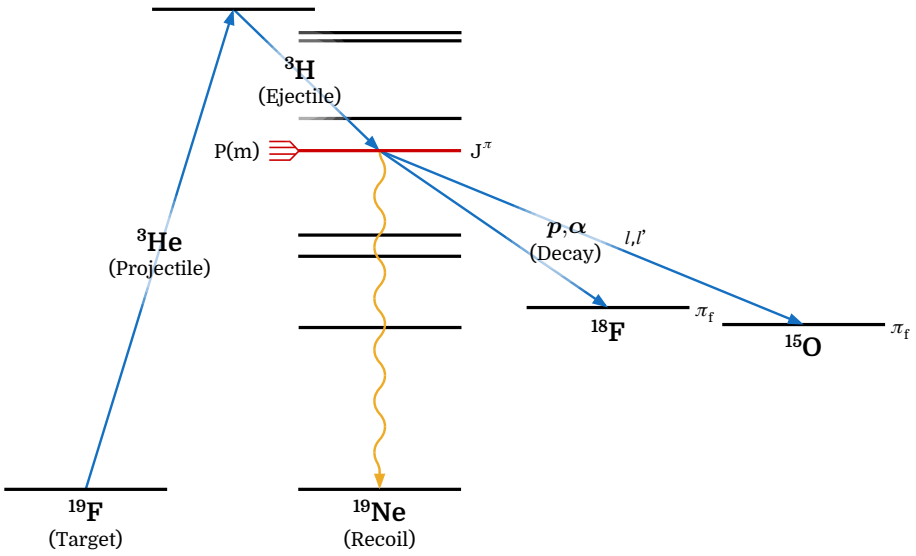

Figure 3.1: Diagram of the ^{19}F(^{3}He,t)^{19}Ne(α)(p) reaction process. Populated states in ^{19}Ne decay via γ, p or α emission. Each state, of spin J$^{\pi}$, occupies one of several magnetic substates P(m) and decays via a channel spin of l or l' directly to the ground state of the daughter nucleus. Adapted from Fig. 1 in ref. [74].

The ^{19}Ne primary decay modes were through alpha-particle and proton emissions and proved to be experimentally trivial to detect. The probability of emission, known as the branching ratio, was used to calculate its associated partial width ($\Gamma_{\alpha,p}$). Ensuring the detectors were sensitive to the position of each decay, emission rates were grouped according to angle, the relative distribution of which is related to the orbital angular momentum of the decay channel and, in turn, the spin of the original nuclear state. Due to energy loss effects, the decay products were unlikely to be an accurate determination of the originating resonance energy. The momentum of the residual ^{3}H (triton) ejectile, however, was able to be analysed to a far higher precision, providing the ^{19}Ne state energy.

The triton and decay particle were therefore detected in coincidence and paired in the data acquisition software to maintain their physical interpretation. Given the widths of the resonances populated, the lifetime of the decay was on the order of 10^{-16} s and required accurate timing information to coordinate the two events. The experimental setup used to achieve these measurements is described in the following sections.

3.2 Beam Production

3.2.1 Ion Source

A duoplasmatron was used to extract the ^{3}He from its bottle and prepare it for acceleration. The gas was admitted into a vacuum chamber containing a cathode filament where the ^{3}He became ionised due to interactions with the free electrons produced by the cathode. An anode, machined into a cone and pierced with a small aperture, extracted the plasma which was subsequently separated by charge using a secondary electrode. Collisions with a lithium vapor caused the ^{3}He ions to capture electrons and become negative. Any ^{3}He that escaped the source without ionisation was recycled using a cold-trap.

3.2.2 Tandem Accelerator

To perform the reaction with the required kinematics, the beam of ^{3}He particles had to be accelerated to the necessary energy of 25 MeV (8.33 MeV u^{-1}). The acceleration was accomplished using the IPN Orsay tandem accelerator where the anions from the ion source were accelerated toward a positive potential terminal held at the centre of the tandem chamber.

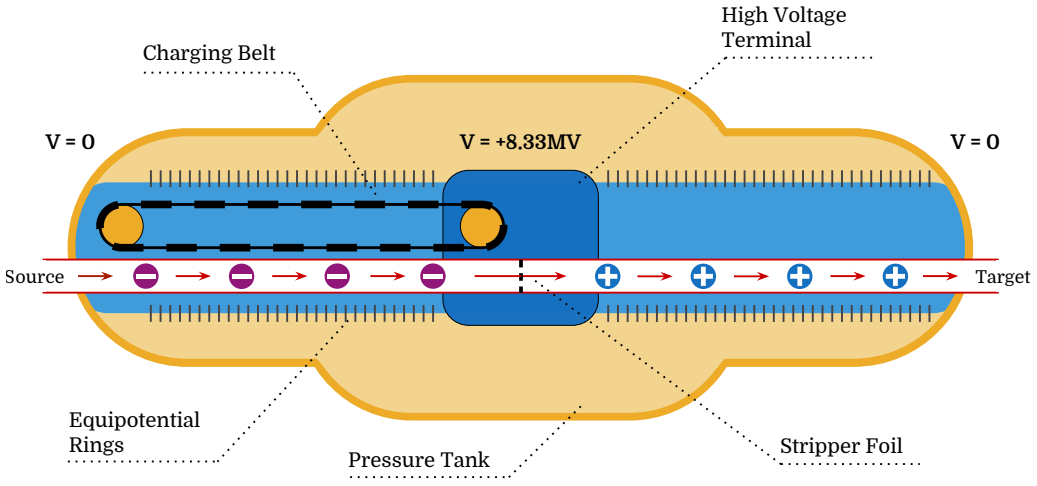

Figure 3.2: Schematic diagram of a tandem accelerator. Beam is accelerated from left to right due to the high potential held at the centre.

The central potential is created by transferring electrons away from the terminal using an electrostatically charged belt consisting of alternating conducting and insulating surfaces.

In order to reach the high voltage required, the terminal is held within a steel tank filled with sulphur hexafluoride (SF_6) which acts as an electrical insulator.

Within the terminal the accelerated ions are stripped of their electrons usually from passing through a carbon or beryllium foil. Now positively charged, the $^3He^{2+}$ is accelerated away from the same potential thus multiplying the output of the accelerator. Fig. 3.2 shows a diagram of the accelerator and how each half of the chamber provides an accelerating force. The extracted beam energy follows the simple equation $E = (q+1)V_{terminal}$, where q is the ion charge state.

The beam is then transported through a series of evacuated beam pipes to the reaction chamber in front of the split-pole spectrograph. Fig. 3.3 shows the organisation of the IPNO facility and the path the ^{3}He beam took to the reaction chamber for this experiment.

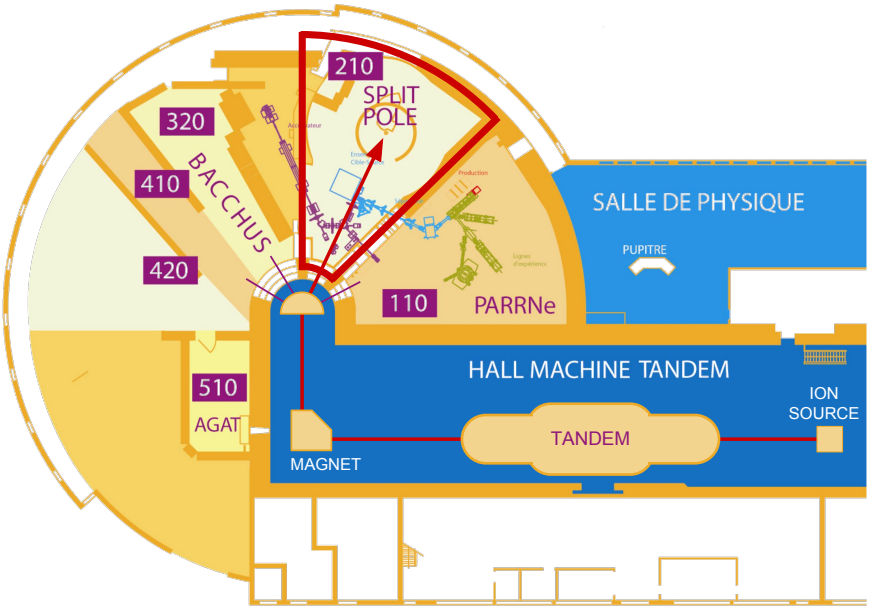

Figure 3.3: Diagram showing the beam transport required to take the accelerated ^{3}He to the reaction chamber.

3.3 Enge Split-pole Spectrograph

The Enge Split-pole at the Institut de Physique Nucléaire, Orsay is a magnetic spectrometer that momentum-analyses charged particles. Following a nuclear reaction, light mass products can be analysed using the spectrograph to precisely determine their energy and

therefore the nuclear state from which they originated. The energy is obtained by projecting spatially separated particles of different momenta onto a position sensitive detector using a magnetic field.

The aim with any magnetic spectrometer is to maximise the solid angle and momentum 'bite' (range) whilst still focusing equivalent momentum particles on the same detector position. Whilst magnetic spectrometers had already been in use for some time, the split-pole design by Harald Enge [75, 76] offered some improvements.

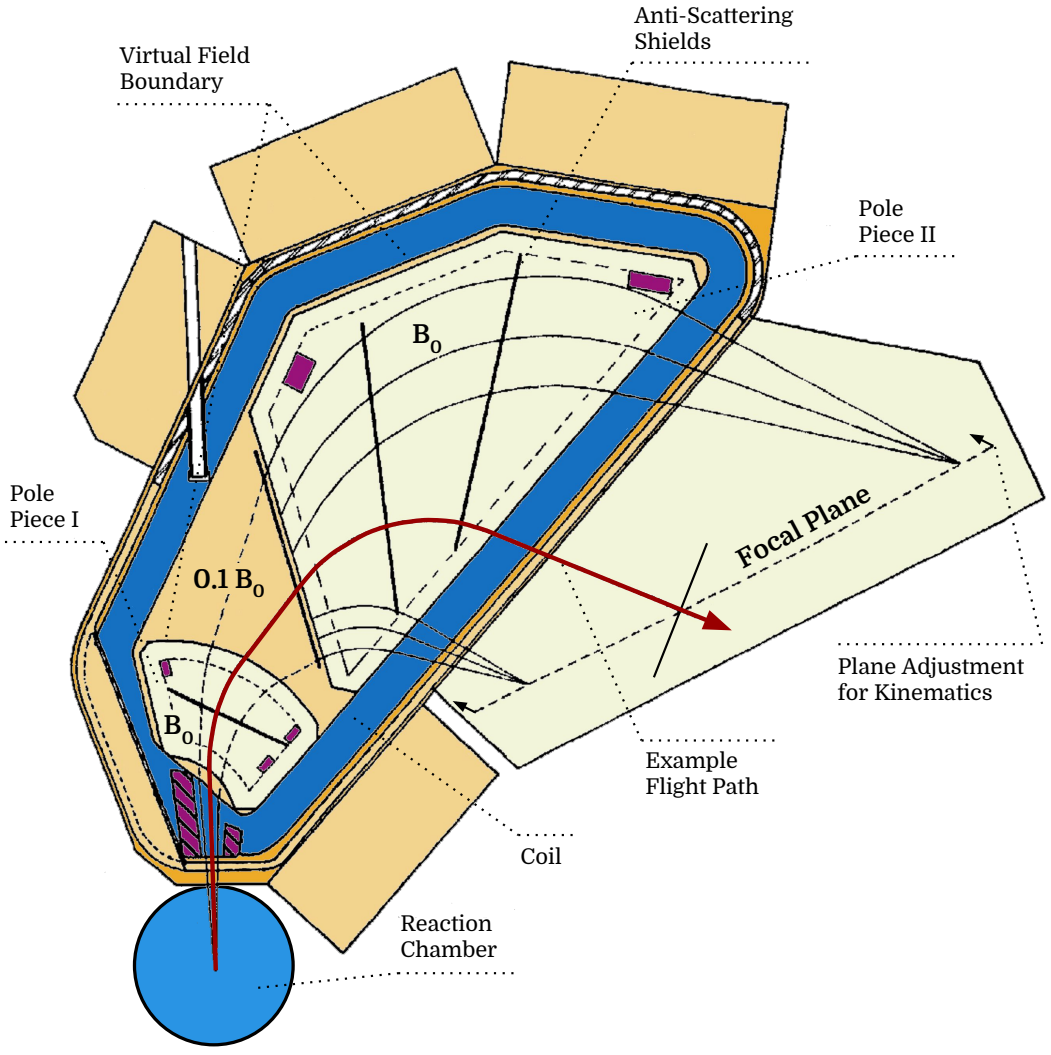

Figure 3.4: Cross-section of a Split-pole design magnetic spectrometer. Highlighted is the path of a reaction product originating from the target, centred in the reaction chamber, to the focal plane at the end of the spectrometer. Adapted from Fig. 5 in ref. [77].

By splitting each pole of the magnet in two whilst remaining enveloped by a single coil, fringe field effects outside of the pole regions provide transverse focusing. The shaping

of the poles (in particular the exit boundary of the first piece) focuses the particles in the plane of the spectrometer. The result was a higher degree of separation and therefore improved energy resolution. Fig. 3.4 shows a cross-section of a split-pole and demonstrates the flight-path of a particle through the magnetic field.

3.3.1 Magnetic Spectrometers

The principal behind a magnetic spectrometer resides in the application of a magnetic field to deflect incoming charged particles from their original trajectory [77]. As the energy, and therefore velocity, of the reaction ejectile changes, so too does the magnitude of deflection. By applying simple charged-particle dynamics it is possible to quantify the deflection experienced by the reaction products.

The force on a particle of charge Q, velocity v and mass m passing through a magnetic field of magnitude and direction $\underline{B}$ is given by

$$\underline{F} = Q\underline{v} \times \underline{B} \ . \tag{3.1}$$

The magnetic field produces a centripetal acceleration causing the particle to be deflected in an orbital path with a radius ρ, thus experiencing the force,

$$F = \frac{mv^2}{\rho} \ . \tag{3.2}$$

Making the assumption that the velocity is perpendicular to the magnetic field, eq. 3.1 and 3.2 can be equated to give

$$B\rho = \frac{mv}{Q} \ . \tag{3.3}$$

The product $B\rho$ is referred to as the magnetic rigidity and is, as quoted, a measure of how rigid a particle's motion is through a magnetic field. The higher the mass or more energy it has, the higher its rigidity. The principle of particle separation applies to any charged particle passing through a one-dimensional field and must be accounted for even in beam transportation. It is also analogous to the property of electronic rigidity $E\rho$.

3.3.2 Focal Plane Detectors

The resulting orbits of the reaction products are intercepted by a focal plane detector at the end of the Split-pole. Because different reactions performed in the reaction chamber can have vastly different kinematics, the reaction products can be focused at different depths. The focal plane is therefore motorised and can be adjusted to suit the reaction. Fig. 3.4 demonstrates the direction of this movement.

Within the focal plane are three separate detectors; two proportional counters and a plastic scintillator. The three detectors are used together to identify the particles that reach the focal plane.

Proportional Counters as Detectors

A proportional counter provides an environment for self-amplification of signals for any incident ionising radiation. The counter consists of a gas-filled chamber, in the case of the Split-pole isobutane (C_4H_{10}), and a potential field provided by a cathode and anode. As the tritons pass through the chamber they deposit energy creating electron-ion pairs which are accelerated toward the respective electrode. As the electrons gain energy, they themselves ionise the gas creating further electron-ion pairs which are subsequently accelerated. The initial signal (typically one pair produced per 30 eV lost) is amplified and the avalanche of electrons detected at the anode is proportional to the energy deposited.

The gas and voltage used affect the operation of the counter and can be changed to improve the efficiency and signal quality for the radiation of interest. The gas chamber in the Split-pole is of sufficient density to remove only some of the particle's energy allowing it to pass through to the remaining focal plane detectors. In some configurations the electrodes can be rearranged to a specific orientation to provide information on the geometry of the interaction. For example, multiple anode wires forming a grid structure provide an x and y position for the radiation's path through the detector. The Split-pole however uses a series of delay lines to calculate the particle's position as explained in section 3.3.2.

Plastic Scintillators as Detectors

Radiation interacting with a scintillator deposits energy, exciting its constituent atoms, which then promptly de-excite producing photons. Coupled to a photocathode, the photons strike a photosensitive surface and release an electron. The electrons are multiplied after colliding with a series of dynodes, amplifying the signal and finally collecting on an anode for measurement. The choice of scintillating material for a given type of radiation dictates the detector properties, such as efficiency, energy resolution, response time, light yield etc. A common configuration for detecting charged particles (and also used as part of the Split-pole's focal plane detectors) is an organic scintillator within a solid plastic solvent that can be easily shaped for various geometries.

Split-pole Particle Identification

Measuring a particle's position after passing through a mass spectrometer is not always enough to determine if the particle originated from the reaction of interest. It is necessary to identify the particle's isotope by utilising the differential energy loss particles experience as they interact with the orbital electrons of atoms. The aforementioned energy loss can be measured using detectors such as those mentioned above and is dependent on the particle's charge as described by the non-relativistic Bethe-Bloch formula,

$$-\frac{dE}{dx} = \frac{4\pi n Z^2}{m_e v^2}\frac{e^2}{4\pi\epsilon_0}\left[\ln\left(\frac{2m_e v^2}{I}\right)\right] , \tag{3.4}$$

where n is the target electron density and I is the electron excitation potential of the target. Considering two particles with the same initial velocity, the more massive or higher charged particle will deposit a large amount of energy in the first energy loss (dE) detector but a smaller amount in a second total energy (E) detector. Comparing the signals from the two will yield a dE v E particle identification plot that highlights contaminating particles.

The primary purpose of the first proportional counter in the Split-pole is to provide a position measurement of the particles' location along the focal plane. Five wires run parallel to the plane and act as the anodes. A series of strips run into the plane at an angle of 40°, the same angle the analysed reaction products reach the focal plane. The strips are used as cathodes and are connected in series by a delay line. Two signals are

read out, one at each end of the delay line starting/stopping a TDC. The time difference calculated by the TDC provides the position of interaction along the focal plane.

The second proportional counter (and secondary use of the first) is for measuring energy loss. The plastic scintillator is the last detector the particles interact with and measures the total remaining energy. Given the focal plane length, signals from the plastic scintillator are read out at both ends. Two readings are required because the light signals produced from events at the focal plane extremities reduce in intensity when read at the opposing end causing the signal to fall below threshold. In total, five data elements are recorded from the Split-pole, shown in Table 3.1.

Element	**French**	**English**	
1	Position	Position	Prop Counter
2	Fil	Wire (thread)	
3	δE	δE	Prop Counter
4	Plastique Petit	Small Plastic	Scintillator
5	Plastique Grand	Big Plastic	

Table 3.1: List of data elements taken from the Split-pole and their detector of origin. Both the French and English terms have been used to reference the elements in this thesis.

3.3.3 Magnetic Field

Due to variations in the current applied to the Split-pole coil, the magnetic field across the dipole is not constant and the Split-pole at Orsay does not include a feedback loop to correct for the variations. Equation 3.3 shows that for the same particle travelling through different field strengths, different position values will be recorded reducing the energy resolution.

The rate of change can vary from a few seconds to several hours and is typically on the order of $^{\delta B}/_{B} \approx 10^{-4}$ (see Fig. 4.4). A nuclear magnetic resonance (NMR) probe records the magnetic field strength during the course of the experiment and can be used in calibration of the focal plane position. The calibration process is explained further in section 4.2.1.

3.4 Silicon Semiconductor Array

3.4.1 Coincidence Measurement

As mentioned previously, the primary purpose of the experiment was to measure the decaying particles from the populated ^{19}Ne states. To this end, detectors were required to surround the target that would be sensitive to the alpha-particle and proton decay energies expected. In order to anticipate and correct for the angular dependence of the decay (given the spin of the originating state), the detectors would need to have a high position sensitivity. For this experiment, W1-type [78] silicon semiconductor detectors were placed within the reaction chamber itself.

Semiconductors as Detectors

A crystalline material forms a periodic lattice of atoms that restricts the orbiting electrons to specific energy bands. The valence band corresponds to the highest electron orbital and thus still restricted to a specific lattice site. The conduction band is the energy region in which electrons are free to move throughout the entire structure. If the difference (band gap) between the two energy regions is sufficiently large, the crystal becomes an electrical insulator. By manipulating the band gap, the material can become a partial conductor that only allows free movement of electrons if enough energy is supplied to the system (for example incident radiation).

As electrons are promoted from the valence to conduction band, positively charged holes appear and, under the influence of an applied electric potential, will drift in the opposite direction to the now free electron. The stream of charge creates a measurable current directly proportional to the energy of the incident radiation that created the electron hole pair. To function as a detector, the principal desirable property is a high drift velocity that prevents the electrons and holes from recombining thus maintaining a high level of charge proportionality.

To ensure a large potential difference and therefore fast drift, atoms within the crystal can be substituted for an element with a higher or lower number of valence electrons, leaving an extra electron or hole once the covalent bonds have been formed in the lattice. An n-type semiconductor has been doped with an element that provides more electrons, whilst

a p-type has fewer electrons. Combining the two causes the excess electrons to flow across the junction from the n to the p-type semiconductor whilst still maintaining the charge imbalance from the doping elements atomic numbers. A depleted region in the system is formed where electrons and holes have recombined. Adding an external voltage extends this region and further increases the potential seen by any excited electron and hole pairs.

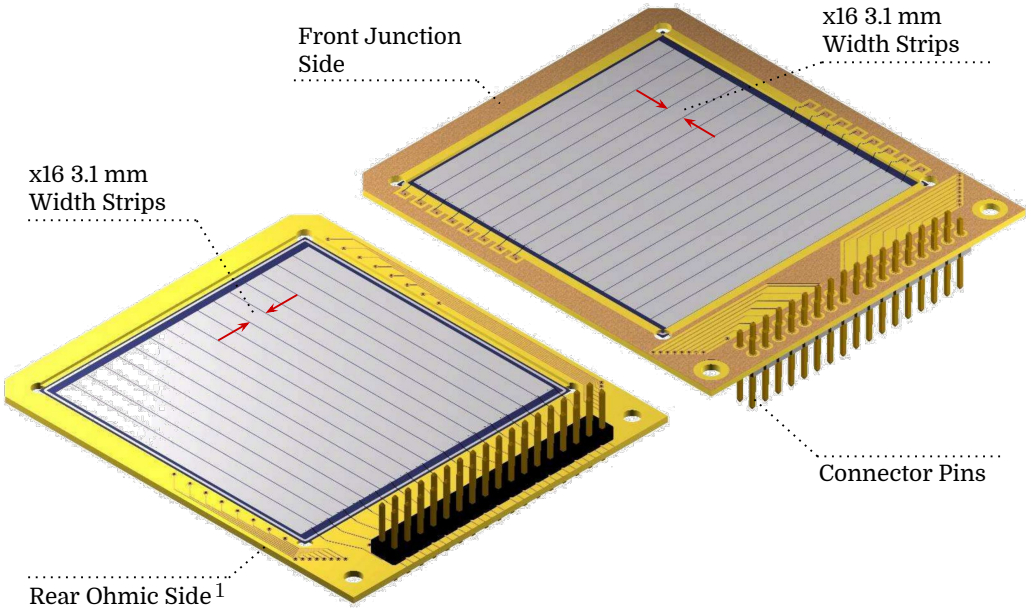

Figure 3.5: Digital render of the W1-type silicon semiconductors used in this experiment. The strips on the front side are orthogonal to those on the back creating a matrix of detectable positions with a 3mm^2 resolution.

W1-Type Semiconductors

The W1 detectors used for the experiment contain a fully depleted semiconductor wafer, made primarily of silicon and segmented into 16 electrically isolated strips on both the front and back. The strips are arranged such that the front 16 are orthogonal to the rear 16 (Fig. 3.5). The double-sided silicon strip detector (DSSSD) is capable of reading a charge from both a front and a back strip, constraining an incident particle's position to a much higher resolution than just a single semiconductor plane. Each strip is 3 mm by 50 mm with a 0.1 mm interstrip region necessary to prevent crosstalk. The detector's position resolution is, therefore, $\sim \pm 1.5$ mm^2 though the angular resolution is dependent on the particle's origin.

[1] An ohmic contact is a non-rectifying electrode through which charges of either sign can flow freely [79].

3.4.2 Target Chamber Geometry

To maximise the ^{19}Ne decay detection efficiency, the DSSSD array covered the largest solid angle possible. The circular reaction chamber measured 31.75 cm in diameter and 15 cm in height. A sliding seal allowed the spectrograph to be rotated round the chamber whilst remaining under vacuum. Experimental target foils were fixed to a ladder in the centre of the chamber and operated remotely, exchanging five target positions.

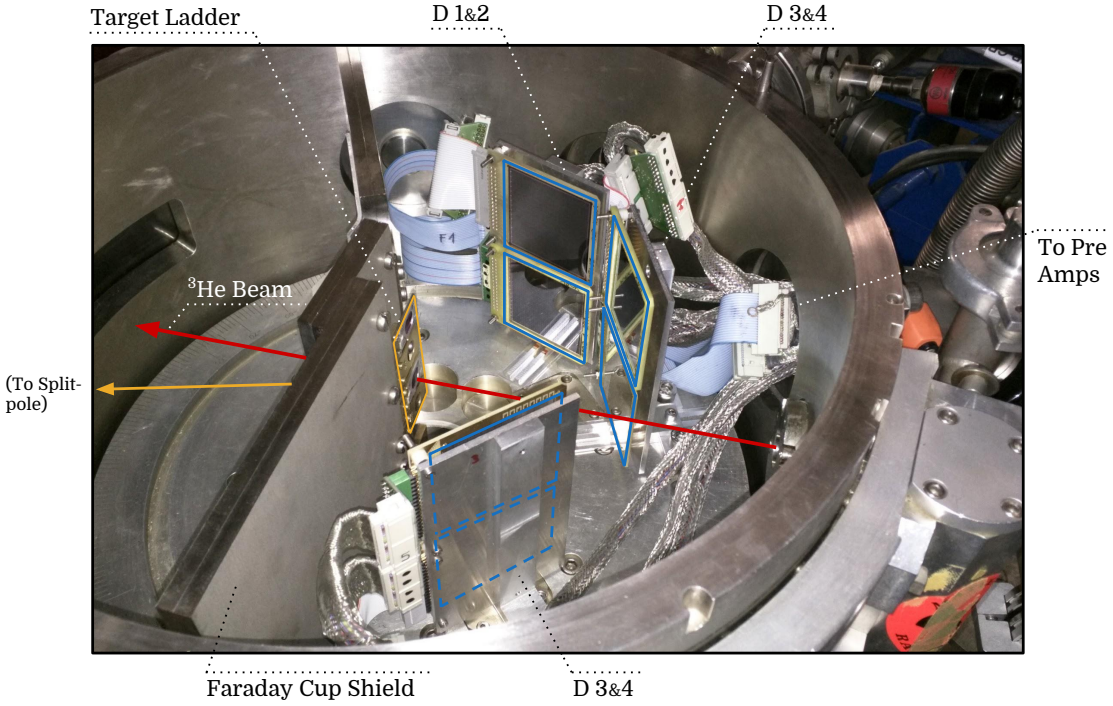

Figure 3.6: Photograph of the Split-pole reaction chamber housing the CaF_2 target (highlighted in yellow) and Si semiconductor array (highlighted in blue). When the lid is closed, the Faraday cup is positioned directly behind the target ladder, shielded from the silicon.

To measure beam current, a Faraday cup is permanently hung from the chamber ceiling behind the target ladder. The disadvantages to the faraday cup placement are two-fold. First, its placement behind the target ladder prevents operation of the Split-pole from 0° in the lab frame. Second, as the cup is made from graphite, excitations of the carbon nuclei to the 2^+ state from unreacted beam cause 4.4 MeV γ rays to flood the chamber in addition to the β-decay products from the cup activation. Both of these radiation sources are too strong for silicon placement within the chamber without protection. A shield was constructed that divided the chamber in two allowing silicon detectors to be placed at backward angles to the target and remain protected.

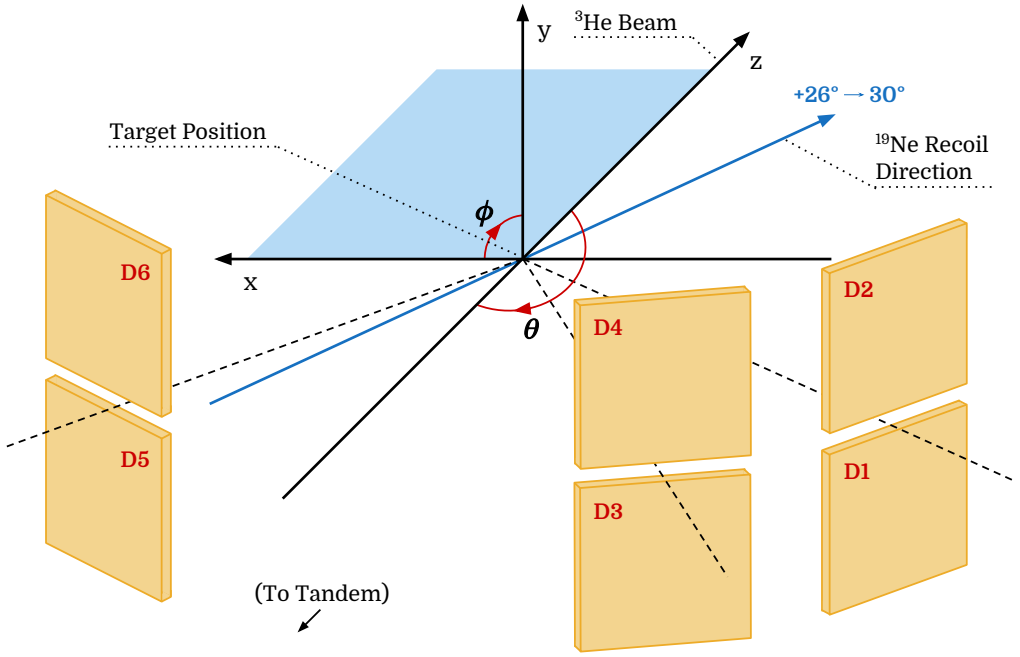

Figure 3.7: Schematic diagram of the reaction chamber geometry. The z axis points along the beam allowing θ to be calculated in the plane of the chamber. The ^{19}Ne recoil direction (shown in blue) causes a rotation to the reference frame of $\sim 28°$ from which the centre of mass angles are calculated.

A rail running round the edge of the chamber allowed radial and angular adjustment to the detector position whilst still remaining normal to the target. As an improvement to previous measurements, new mounts were designed that could stack two W1 detectors vertically thus still occupying the same 'floor space'. A diagram showing the geometry of the silicon array can be found in Fig. 3.7. Three mounts were used to hold six W1 detectors in the chamber, characterised in Table 3.2.

Detector	Thickness / μm	Contact	Angle (θ) / ∘	Distance / mm
1	300	Grid	113	94.4
2	300	Grid		
3	150	Planar	155	98.5
4	300	Grid		
5	140	Grid	(-)135	81.9
6	140	Planar		

Table 3.2: List of W1 type silicon detectors that formed the detector array within the reaction chamber. Angle and distance measurements were taken to the centre point of each detector pair. Positions of each pixel were subsiquently calculated using trigonometric methods.

3.4.3 Silicon Detector Efficiency

In total, the silicon detectors cover 11.45% of the total solid angle[1] (1.44 sr) however this is not accounting for the kinematics of the reaction. Given that the beam carries all of the momentum, reaction products must be forward focused in the laboratory frame. The emission preference has the effect of lowering the detector efficiency depending on the angle subtended between the recoil particle and the specific silicon pixel. To calculate the efficiency of the silicon array, Monte-Carlo[2] simulations reconstructed the chamber geometry and reaction kinematics to estimate the detection probability of each W1 pixel. A framework of pre-defined structures and reactions furnished by NPTool [80] provided a simplified interface with the Geant4 [81] Monte-Carlo algorithms.

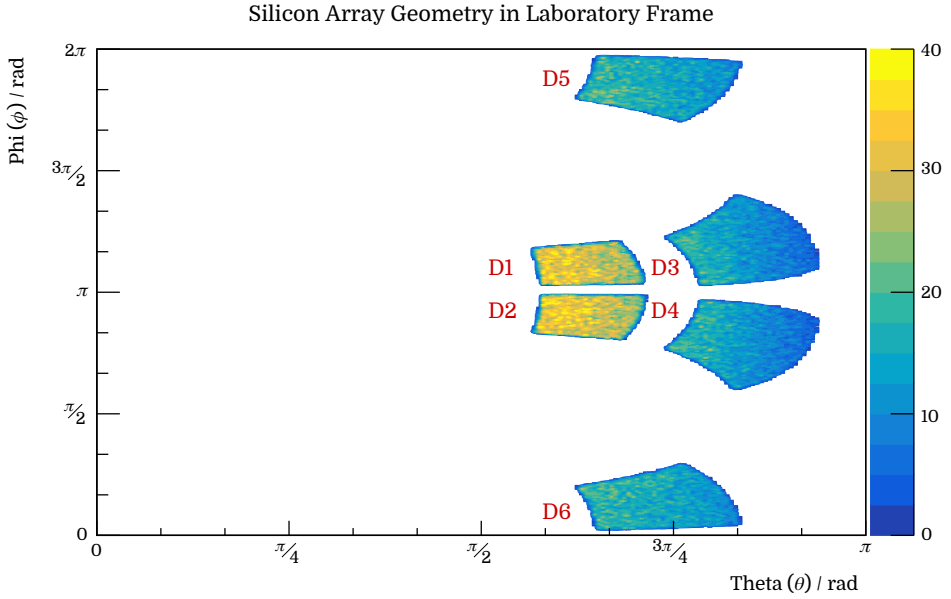

Figure 3.8: ^{19}F(^{3}He,t)^{19}Ne(α)(p) simulation showing angular coverage of the silicon array in the lab frame.

The simulation conducted for this experiment included the six W1 detectors placed according to measurements taken during the experimental set-up, a simplified detector replicating the acceptance window of the Split-pole and the CaF_2 target foil. Separate simulations were run for each ^{19}Ne state of interest and for each decay mode. In addition, a single simulation was run for a continuous range of ^{19}Ne excitations from 5 to 8 MeV necessary for the depiction of Fig. 3.10.

[1] Accounting for the loss of three strips in D1&2 due to the target mount obscuring extreme angles close to 90°.

[2] Monte-Carlo algorithms rely on repetitive random sampling to quantify an output parameter and can, in principle, be used to solve any problem with a probabilistic interpretation.

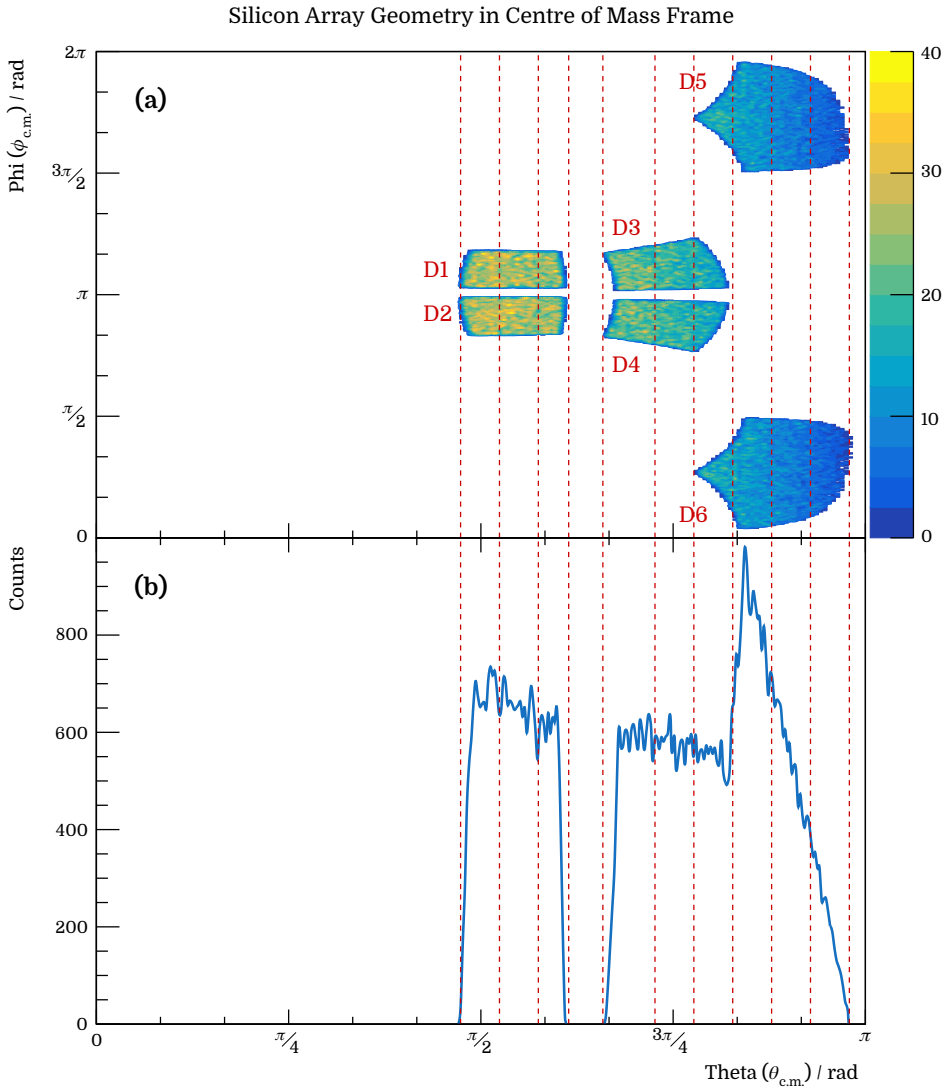

Figure 3.9: ^{19}F(^{3}He,t)^{19}Ne(α)(p) simulation showing angular coverage of the silicon array in the centre of mass frame. Panel **(a)** shows a matrix of theta against phi for each interaction of the α particle with the W1 detectors (back scattered ^{3}He beam was removed using an energy cut). Panel **(b)** shows the x-axis projection of theta. The 12 segments used for angular distribution bins have been highlighted.

Fig. 3.8 shows the angular coverage of the six W1 detectors in the laboratory frame for a single excitation of ^{19}Ne decaying via α emission. In order to correctly interpret the angular correlation of the recoil decay products, it was necessary to transform silicon array pixel positions from lab into centre of mass (c.m.) coordinates. As the only component that need be considered in radioactive decay is the parent nucleus itself, the centre of mass frame is that of the moving ^{19}Ne. The coordinates for each silicon pixel were therefore rotated around the y-axis toward the direction of the ^{19}Ne recoil (see Fig. 3.7) and boosted proportionally to its kinetic energy. The calculations for the frame transformation

are outlined in Appendix A. The silicon angular coverage, and therefore efficiency, are consequently dependent on the ^{19}Ne state populated. Panel **(a)** of Fig. 3.9 shows the angular coverage of the array after rotation and boost into the centre of mass frame.

Gating on single resonance populations, the total angular range was divided into 12 segments binned in theta (panel **(b)** of Fig. 3.9) and the efficiency of each given by

$$\varepsilon_{\text{bin}} = \frac{1}{4\pi \ n_{\text{bin}}/n_{\text{tot}}} \ , \tag{3.5}$$

where n_{bin} is the alpha-particle or proton counts in the silicon array gated on the angular bin and n_{tot} is the total number of tritons detected in the simulated Split-pole. Multiplying this number by the number of experimental counts detected gives the counts per steradian required for angular distribution plots.

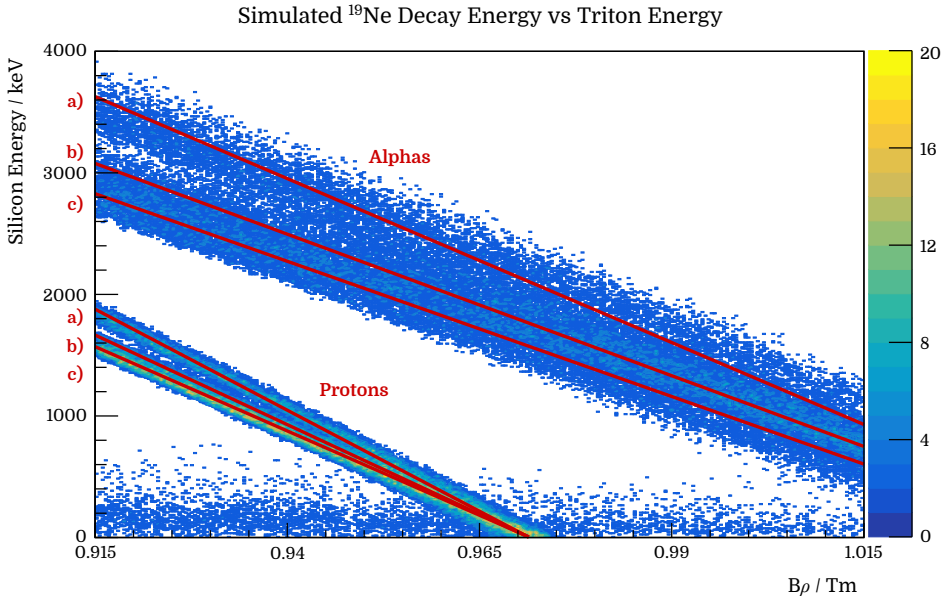

Figure 3.10: ^{19}F(^{3}He,t)^{19}Ne(α)(p) simulation showing Si energy against Split-pole magnetic rigidity. The triton energy has been given in units of magnetic rigidity. The expected positions of p and α loci are well separated. The lines **a**, **b** and **c** have been drawn as guides to show the median of the loci originating from detectors 1&2, 3&4 and 5&6 respectively.

The simulation predicted the kinematic relationship between the detected tritons and the recoil decay products as shown in Fig. 3.10. As the timing resolution for the system was insufficient to identify alpha-particles from protons, it is this relationship that was used to identify the decay products. The loci diffuseness is dependent on energy straggling through the target and thus on the angle of the pixel, hence the disparity between each pair of detectors.

3.5 Signal Analysis

The rate of ^{19}Ne population from the beam hitting the target requires appropriate electronics to record the signals from each of the Split-pole's 5 elements in addition to the 196 strip channels in the silicon array. With approximately 300 events every second in the Split-pole and the Si array subject to a rate almost three orders of magnitude higher, a digital data acquisition system (DAQ) was necessary to record each signal.

3.5.1 Electronics

The signals from the silicon array were fed into Mesytec MPR-16 preamplifiers with each silicon strip requiring its own channel. The primary function of a preamplifier is to extract the signal from the detector whilst maximising the signal-to-noise ratio. As semiconductors produce only a small output signal, the preamplification was charge-sensitive (as opposed to current-sensitive) for the purpose of integrating the current across the entire signal pulse. Signals from the silicon strips were passed through the reaction chamber feedthroughs and, to reduce noise, immediately placed into the MPR-16s. This limits additional input capacitance caused by radio frequency pickup, ground loops or noise from the cable itself.

Signals from the preamplifier were then sent into Mesytec STM-16+ shaping amplifiers. The intention of shaping the pulse is to remove the pile-up from a train of signals from the preamplifier. The relative pulse height can be extracted and any additional height from the tail of the previous pulse is removed. Due to the long exponential decay of the preamplifier, the signal can 'undershoot' as it returns to zero. The signal decay undershoot can be alleviated using a pole zero cancellation network where an adjustable resistor is placed in parallel with the CR capacitor. Once shaped the signal height is then analysed from the analogue pulse and converted into a digital measurement. Silena-9418 CR-RC[1] ADCs (Analogue to Digital Converter) were used to process 32 channels at a time thus requiring one ADC for each detector.

The shaping amplifiers also included an LED (Leading Edge Discriminator) that generated a logic pulse if the shaped signal was above a certain threshold. The pulse was used as a stop signal for the CAEN V767 TDCs (Time to Digital Converter) that were operated

[1] Charge differentiator (CR) and integrator (RC) circuits are combined in series to alleviate undesirable features from using a single circuit alone.

in 'trigger matching' mode. The time between the DAQ trigger (see section 3.5.1) and any signal from the silicon within the timing window (see section 3.5.2) could therefore be calculated and digitised.

Given the natural amplification provided by the nature of the detectors, the Split-pole data elements were treated differently. The signals from the two proportional counters and both ends of the plastic were sent through a TFA (Timing Filter Amplifier) to shape the signal before the peak was analysed by a 7th Silena-9418 ADC. As mentioned in section 3.3.2 the position element was calculated from the timing difference between the left and right signals in the first proportional counter and was also fed into the ADC.

A pulser module set to 5.1 kHz was run throughout the experiment to record the relative timing of each event for offline correction of the Split-pole's magnetic field variation. The pulser was fed into a CAEN V560 scaler for the DAQ to record. The path of these signals and the sequence of modules used have been outlined in Fig. 3.11.

Split-pole Trigger

The signals processed by the ADCs are only recorded to disk after the DAQ has been triggered. For this experiment, the trigger was provided by the Split-pole using a coincidence between one of the proportional counters (wire) and one of the plastic signals (PlasP). Copies of each signal were taken after amplification by the TFA and passed through a discriminator to provide logic pulses. The discriminators were set such that the wire pulse lay inside a 'gate' provided by the plastic signal. If both detectors fired, the coincidence unit produced a logic pulse to trigger the DAQ. Fig 3.12 shows the coincidence logic used between the wire and plastic signals and the relative timing of each (this is also in reference to point **a** in Fig. 3.13).

The data acquisition was controlled by a Silena-9418 Acquisition Control module (SAC) that accepts the trigger and manages the data transfer between the ADC, TDC and scaler modules within the VME (Versa Module Europa) bus crate. When the DAQ is triggered, the SAC duplicates the trigger signal to the ADCs. If the event is accepted, the SAC emits a COM signal to identify the DAQ as busy.

For this experiment, the 'Monitor 2' source was used as a secondary output for the COM signal and transmitted as a trigger for the TDCs, thus TDC data is only recorded if ADC

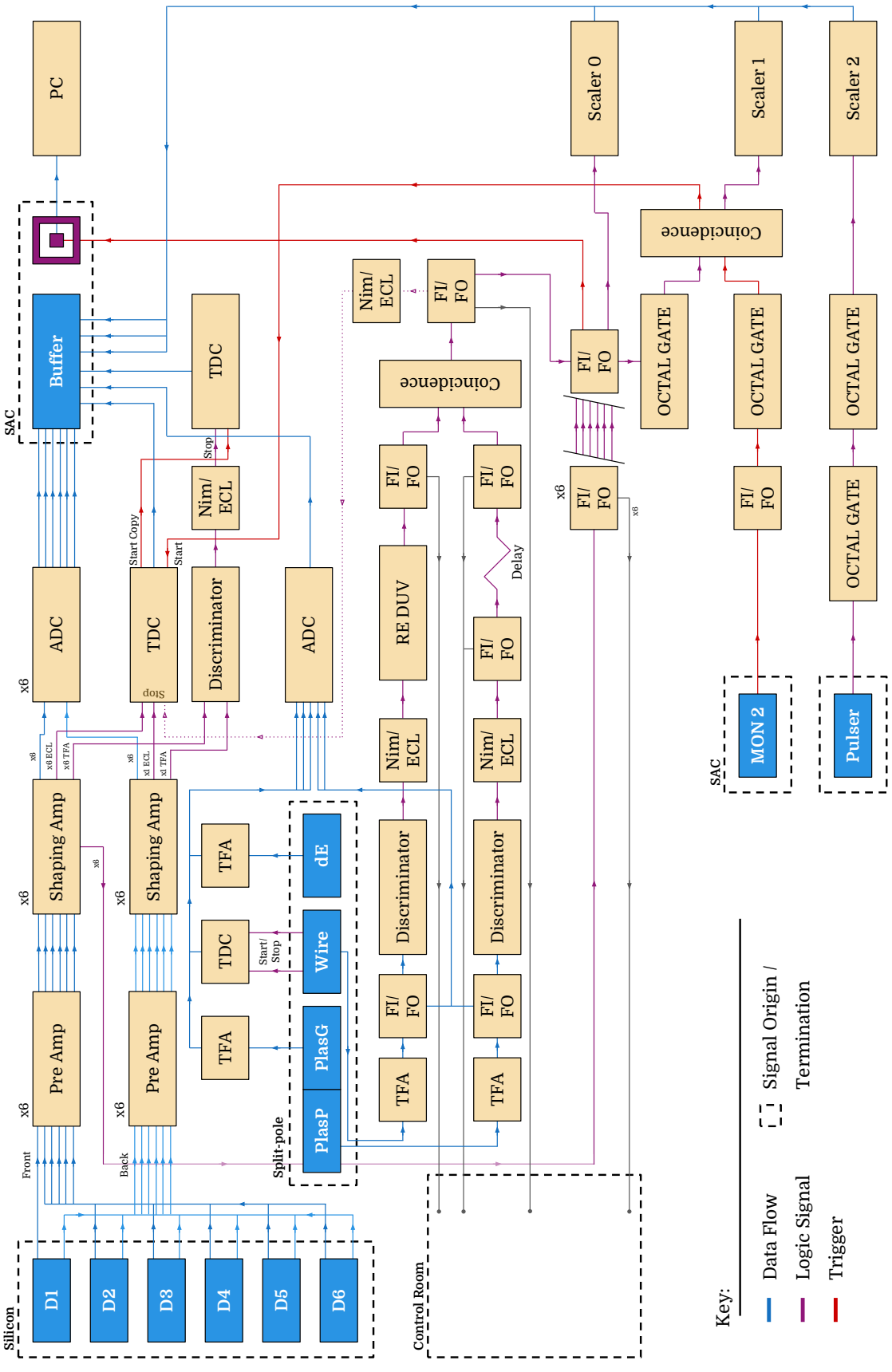

Figure 3.11: Signal analysis and trigger logic diagram used for the experiment. Signals used for physical measurements are shown in blue. The logic paths are shown in purple with the trigger signals highlighted in red. Several key signals were duplicated and passed into the control room for monitoring.

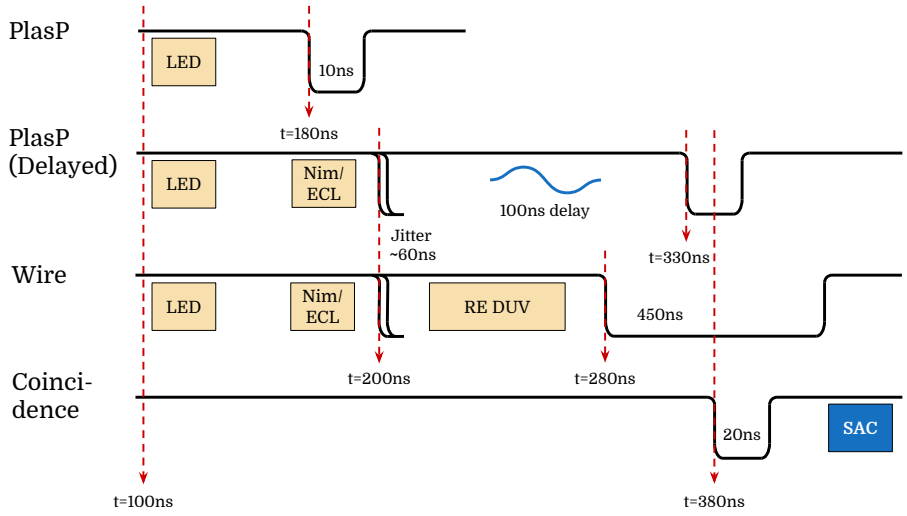

Figure 3.12: Splitpole signal logic used to produce the DAQ trigger (point **a** in Fig. 3.13). Relative timing between the wire and Plasic signals have been marked in addition to the width of the logic pulses. The signal widths were chosen to account for the natural jitter observed after the signal conversion.

data is recorded. A visualisation of this event sequence has been outlined in Fig. 3.13. The CAEN V560 scaler was used to count the triggers sent to the SAC and the triggers that were sent to the TDCs. In this way, the deadtime of the system could be calculated by comparing the two.

The SAC has a 40-MHz clock resulting in a 25-ns clock cycle. This causes a 25-ns jitter on the COM signal used to start the TDCs but can be removed by ensuring MON2 is in coincidence with a delayed copy of the trigger from the Split-pole before being used to trigger the TDCs. The trigger logic, used to remove the jitter, is shown in Fig. 3.14 located at point **b** in Fig 3.13.

Whilst this dealt with the TDC start signal jitter, the stop signals would still be susceptible. A copy of the DAQ trigger from the splitpole was meant to be sent into the DAQ to provide a reference for the silicon timing signals and subsequently remove the jitter. Unfortunately this signal was not diverted and caused the timing resolution to remain at approximately 20-25 ns rather than a potential resolution of 4 ns. Fortunately the decay particles could still be identified and the background from the lower timing resolution still be accounted for.

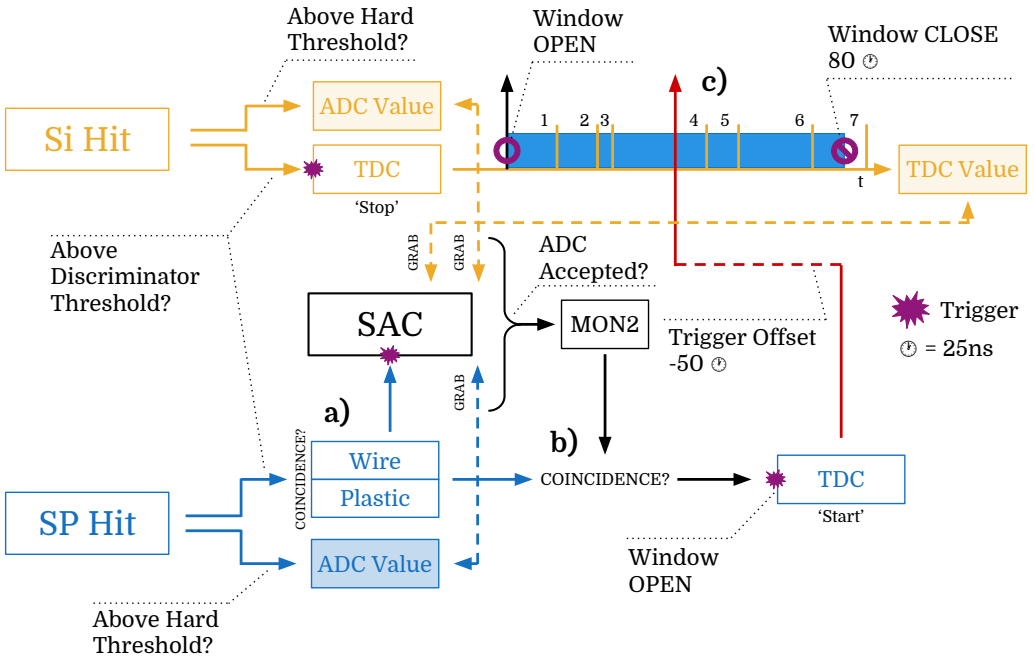

Figure 3.13: Flowchart of signal manipulation to select coincidence events. The relative timing between example Split-pole and silicon hits have been shown. Note that hit 7 is outside of the window and therefore would not be recorded. Points **a**, **b** and **c** have been expanded on in Fig. 3.12, 3.14 and 3.15 respectively.

MIDAS

MIDAS (Multi Instance Data Acquisition System) software provided a suitable interface for the electronic modules mentioned above and managed writing the data to disk. It was also used for online data analysis by sorting the data into histograms as it was recorded. The software regularly used for Split-pole measurements (NARVAL) was run in tandem with MIDAS to check consistency between the two. NARVAL is limited by input channels and was not able to accept all 196 channels from the silicon array.

3.5.2 Coincidence Window

As mentioned before, the experiment was designed to measure two particles from the same reaction in coincidence. The window of the event was therefore required to remain open long enough to accept signals from both the triton in the Split-pole and the ^{19}Ne decay particle in the silicon array. The tritons had a far longer flightpath to the focal plane detectors and, acting as the trigger for the DAQ, the silicon signals were necessarily

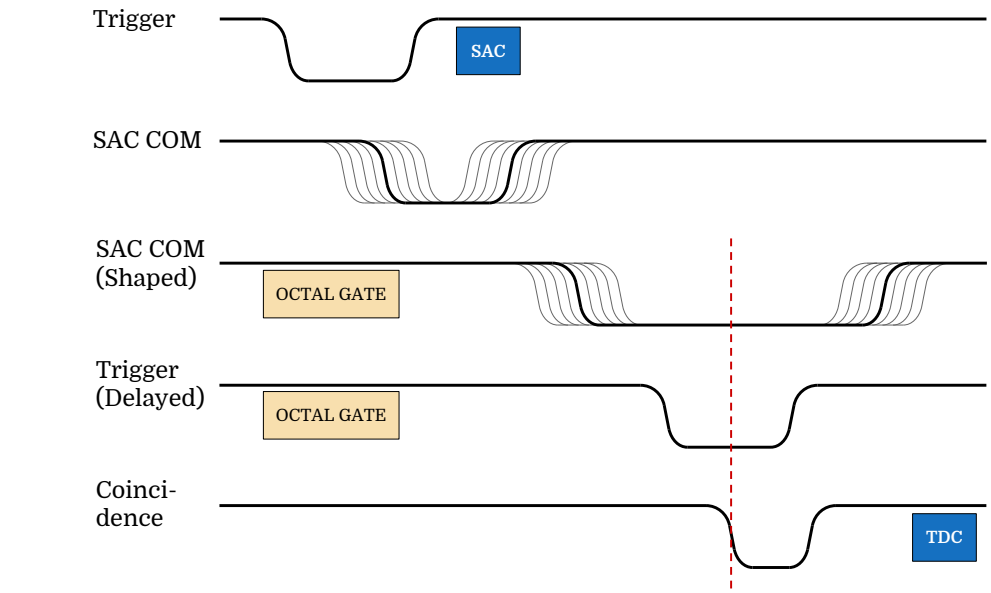

Figure 3.14: Logic used to place the trigger in coincidence with itself to remove SAC jitter (point **b** in Fig. 3.13).

delayed. This was achieved by extending the shaping time of the Mesytec STM-16+ amplifiers and by adjusting the CAEN V767 TDC window.

By placing an offset on the search window, decay hits in the silicon can be held in a buffer until a trigger signal from the triton is provided and the time difference calculated. The relation of the start and stop signals for the TDCs can be traced at point **c** in Fig. 3.13 and Fig. 3.15 shows a histogram of the TDC signals overlaid on the coincidence window. It is clear that coincident events have a similar flight time and form a peak above the random coincidence background.

3.6 Experimental Procedure

The experiment was performed over the course of 9 days segmented into a series of short 'runs'. Two weeks prior to receiving ^{3}He beam from the accelerator, the apparatus was assembled to test electronics and quality of the silicon semiconductors. A small amount of ^{1}H test beam was supplied by the lab during this time to assist in the coincidence set up and construction of the online sort code.

Before recording data from the reaction of interest, the six W1 silicon detectors were calibrated *in situ* using a digital pulse generator and a triple alpha-particle source (^{239}Pu,

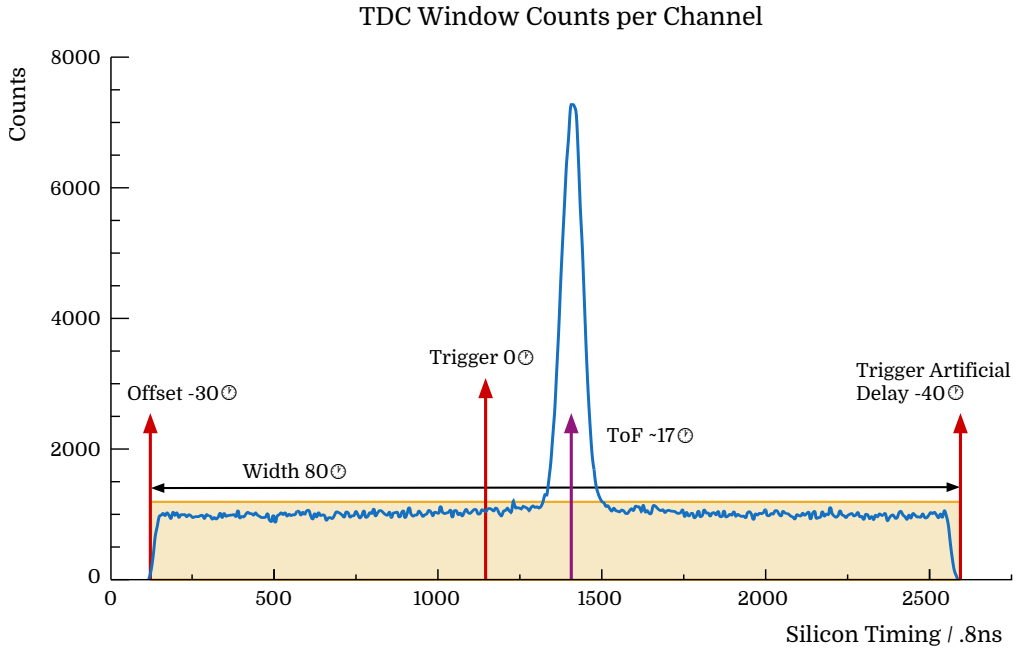

Figure 3.15: Coincidence timing window between Split-pole and silicon array events (point **c** in Fig. 3.13). Trigger, window offset and width are measured in 25ns clock cycles. The experimental time of flight peak is located approximately 17 clock cycles after the trigger.

^{241}Am, ^{244}Cm) placed at the intersection between beam and target ladder. Both were used to normalise the natural gain discrepancies between each semiconductor strip and any possible offset induced by the signal manipulation from the electronics (described in more detail in section 4.2.2).

To ensure minimal noise and maximum statistics from only the reaction of interest, the ^{3}He beam was tuned through into the reaction chamber into the centre of the target position with the narrowest beam spot possible. If part of the beam were to scatter off the aluminium target mount it could produce a high flux of particles within the chamber. For this reason, during the tuning process individual shields were placed over the silicon detectors to limit their exposure. The tuning target ladder consisted of the following:

- Quartz (45°)
- Empty Frame
- $^{\text{nat}}$C
- CaF_2 200μg cm^{-2} (M)[1]
- Empty Frame (M)

[1]For this experiment, some target foils were provided by the Maier-Leibnitz-Laboratory in Munich. These foils were mounted on alternative frames and have been highlighted with (M).

The primary tuning method was using a camera mounted on the ceiling of the chamber pointing at the target ladder. When hit with the beam, the quartz fluoresces allowing the beam spot to be observed. By monitoring the count rate in the Split-pole and silicon detectors, the empty frame was used as confirmation that the beam was not infringing on the edges of the ladder. The natural carbon and calcium-fluoride foils were used for measuring the resolution of the Split-pole before the silicon shields were removed. A poor resolution indicated an off-axis beam.

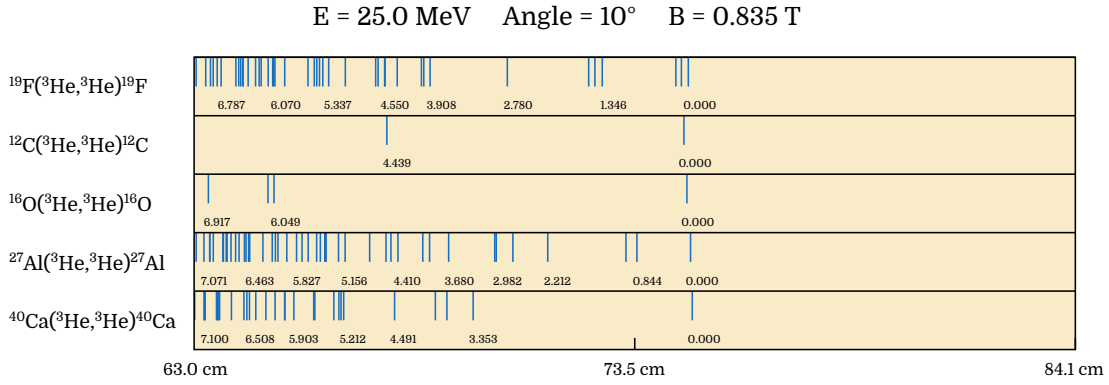

Figure 3.16: Expected focal plane position of populated states observed during tuning. Magnetic field set such that the ground states had smaller orbits and were within the plastic trigger range.

The splitpole was initially tuned to a lower magnetic field (∼0.83 T) to focus scattered ^{3}He onto the focal plane (see Fig. 3.16). The elastic and inelastic reactions provided higher statistics for the tuning process. The field was subsequently increased (∼1.42 T) to focus on reacted tritons (Fig. 3.17).

Once tuned, the chamber was vented, the individual shields removed and the target ladder replaced. The ladder used for tuning had been activated due to contact with the beam, therefore a new ladder was mounted with the frames listed below.

- $^{\text{nat}}$C
- Empty Frame (M)
- CaF_2 200μg cm^{-2} (M)
- CaF_2 100μg cm^{-2} (M)
- CaF_2 50μg cm^{-2} (M)

The carbon and empty frames were retained from the previous target ladder to confirm tuning throughout the experiment. Three different thicknesses of calcium fluoride were included to observe the compromise between statistics and resolution.

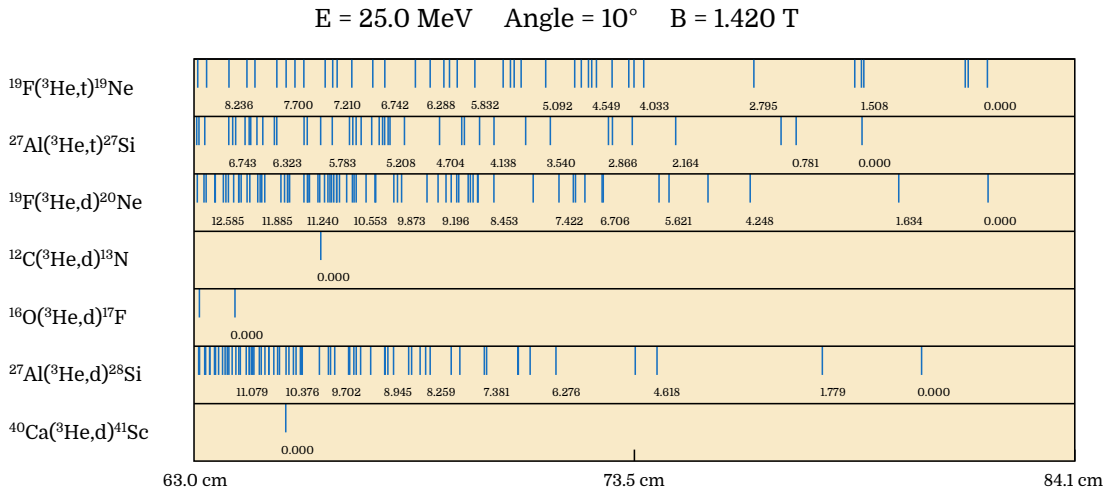

Figure 3.17: The expected populated states visible on the Split-pole focal plane. States of interest are shown in the top panel, contaminants are shown below. The primary source of background are deuteron reactants from elements within the target (F, Ca and C).

A short measurement of scattered beam off ^{nat}C was performed to confirm agreement between the two DAQs mentioned in section 3.5.1. The target was then swapped to the 200 μg cm^{-2} CaF_2 for recording data. The beam energy of 25 MeV and Split-pole angle at 10° were maintained throughout the experiment.

After approximately 48 hours (with 10 hours of ^{3}He beam on target) the ion source failed causing a reduction in beam intensity. With the reduction in statistics from the loss of beam, the best method to maintain an acceptable count rate was to increase the solid angle acceptance of the Split-pole. The horizontal and vertical slits covering the entrance were therefore widened. The wider entrance into the Split-pole produced a wider range of incident triton angles causing the focal point from the magnetic field to vary. The effect of this was to create asymmetric peaks in the Split-pole spectrum (see Fig. 4.12).

Toward the end of the experiment, the beam intensity was able to be raised slightly allowing the target to be changed from the 200 to the 100 μg cm^{-2} thickness. The higher resolution slightly offset the distortion caused by the wide Split-pole opening and additionally exposed a new layer of unreacted CaF_2 to the beam. After the allotted beam time, further calibration runs from the triple alpha-particle source and pulser walkthrough were performed to check any drift from the initial measurements.

Chapter 4

^{19}F(^{3}He,t)^{19}Ne Analysis and Results

4.1 ROOT Data Structure

Data collected by MIDAS (section 3.5.1) required translation into a human-readable format. A sorting program[1] reconstructed event fragments into a tree structure provided by the ROOT data analysis framework. The program read in hexadecimal 'words', linked by the same timestamp, constituting the channel address and corresponding data value. The hex values were converted to integers and assembled into the following 'branches'.

adcN	The number of ADC hits within the event.
adcList	An array listing the ADC channels that were hit.
adcData	An array listing the corresponding ADC values.
tdcN	The number of TDC hits within the event.
tdcList	An array listing the TDC channels that were hit.
tdcData	An array listing the corresponding TDC values.

The tree structure allowed the association of signals originating from the same event thus linking t and ^{19}Ne particle decay hits. Each Split-pole element was fed into a unique ADC channel and could be identified from the above branches. For a more simplistic analysis however, five individual branches were additionally created for each Split-pole signal.

[1] Initially written by Dr. T. Davinson but heavily modified for this work.

4.2 Detector Calibration

In order to correctly interpret the data, the integer values assigned to the detector signals (listed as channels[1]) had to be converted into their physical counterparts. For both the Split-pole and silicon array this involved measuring known signals with precise energies and comparing to the populated channel in the raw data file. The greater the number of reference signals, the greater the accuracy of the calibration.

4.2.1 Split-pole

Particle Identification

As shown in section 3.6 the reaction Q-values were such that there were two products from competing reactions incident on the Split-pole focal plane, only one of which was of interest. Identifying tritons from the ^{19}F(^{3}He,t)^{19}Ne reaction allowed all other data to be discarded, accelerating data sorting and isolating ^{19}Ne peaks for energy calibration.

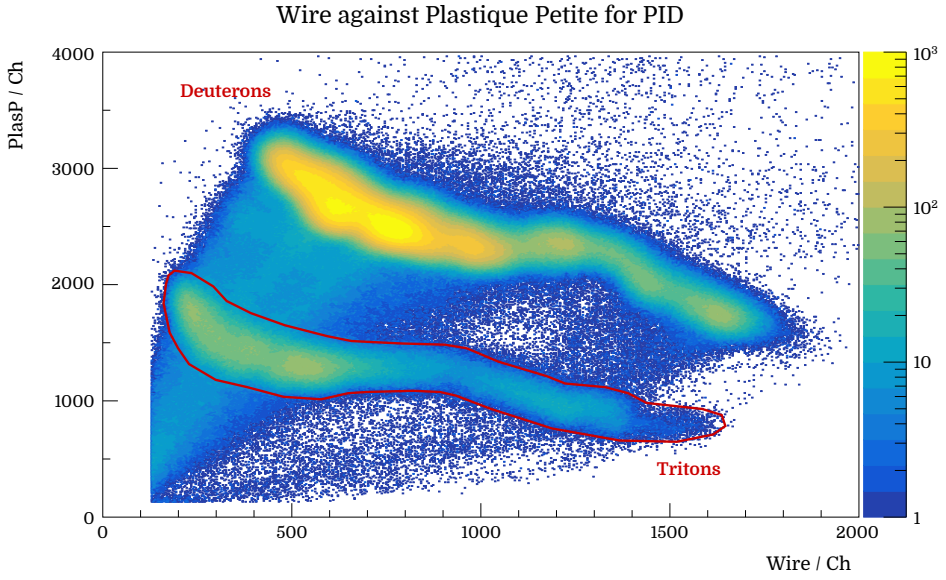

Figure 4.1: Split-pole Wire (ΔE) against Plastique Petite (ΔE) to separate particles by Z and A. The triton selection cut is highlighted in red. Background from partial energy deposition of deuterons 'bleeds' into the triton region.

Tritons were selected on matrix plots of energy (E) against energy loss (ΔE) and of energy loss against energy loss. The position (Pos), Wire and small plastic (PlasP) elements

[1]Not to be confused with the amplifier channels assigned to each silicon strip.

provided the greatest separation between deuterons and tritons. Fig. 4.1 and 4.2 show the sequential cuts made to the data to select on the tritons.

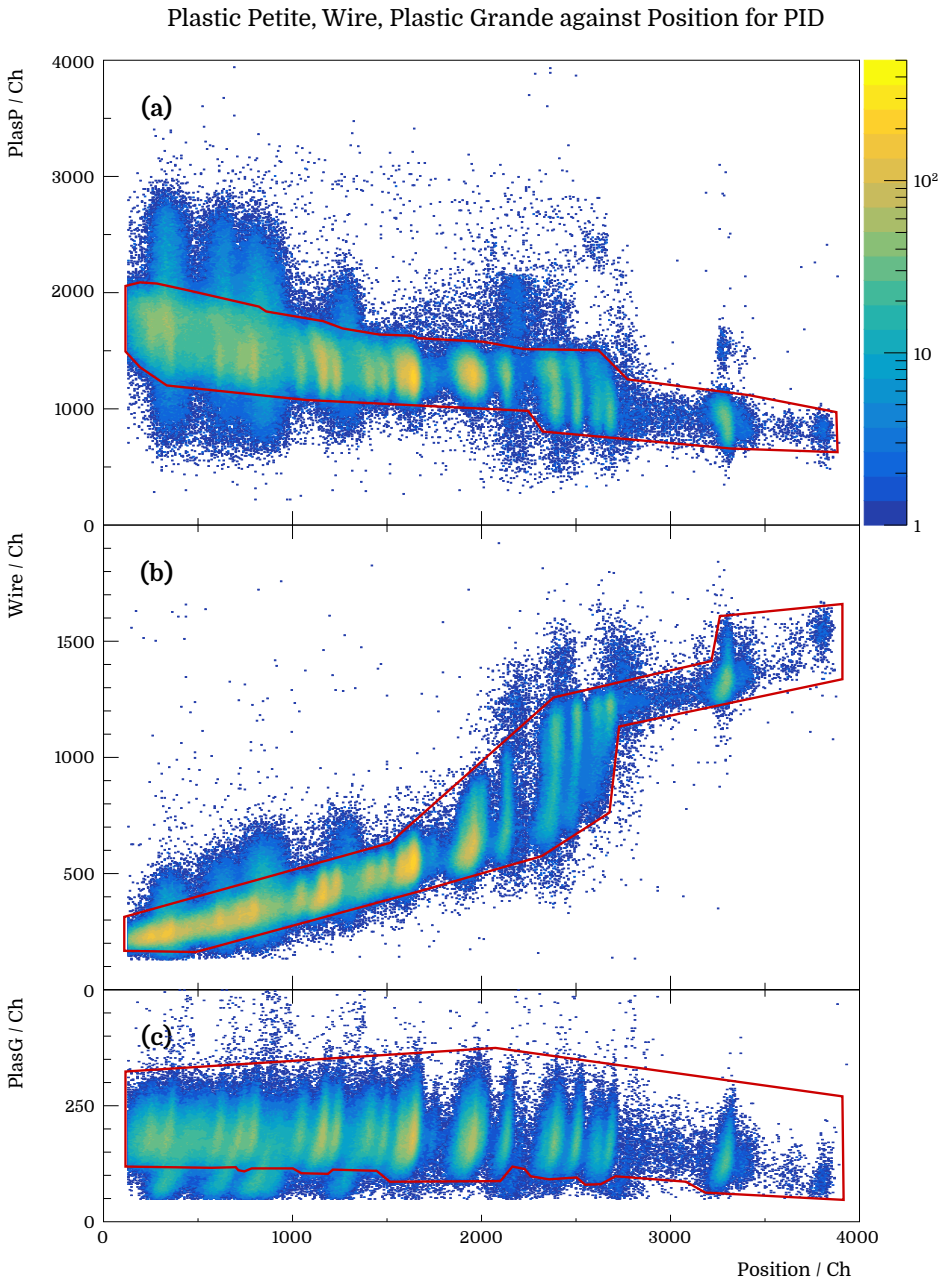

Figure 4.2: Split-pole Position (E) against Plastic and Wire signals (ΔE) for further particle identification. The graphical cuts in each panel are focused on tritons and remove the majority of the remaining deuteron background.

As a note of importance, Fig. 4.1 shows that whilst nominal energies of tritons and deuterons are well separated, ejectiles travelling out of plane[1] have caused deuterons to

[1]Particles travelling unparallel to the Split-pole do not deposit their full energy in the focal plane detectors.

'bleed' into the tritons, making complete separation impossible. The last cut highlighted in panel **c** of Fig. 4.2 used the large plastic (PlasG) to remove as much of this background source as possible. Section 4.4.2 will discuss the contribution and parameterisation of the remaining background.

Split-pole Position

As mentioned previously the high resolution of the Split-pole arises from its positional measurement of the tritons along the focal plane and, therefore, it was only this element that required an accurate calibration. As the position is dependent on the magnetic field (eq. 3.3) which was not stable during the course of the experiment, the channels required calibration into units of magnetic rigidity ($B\rho$) rather than energy.

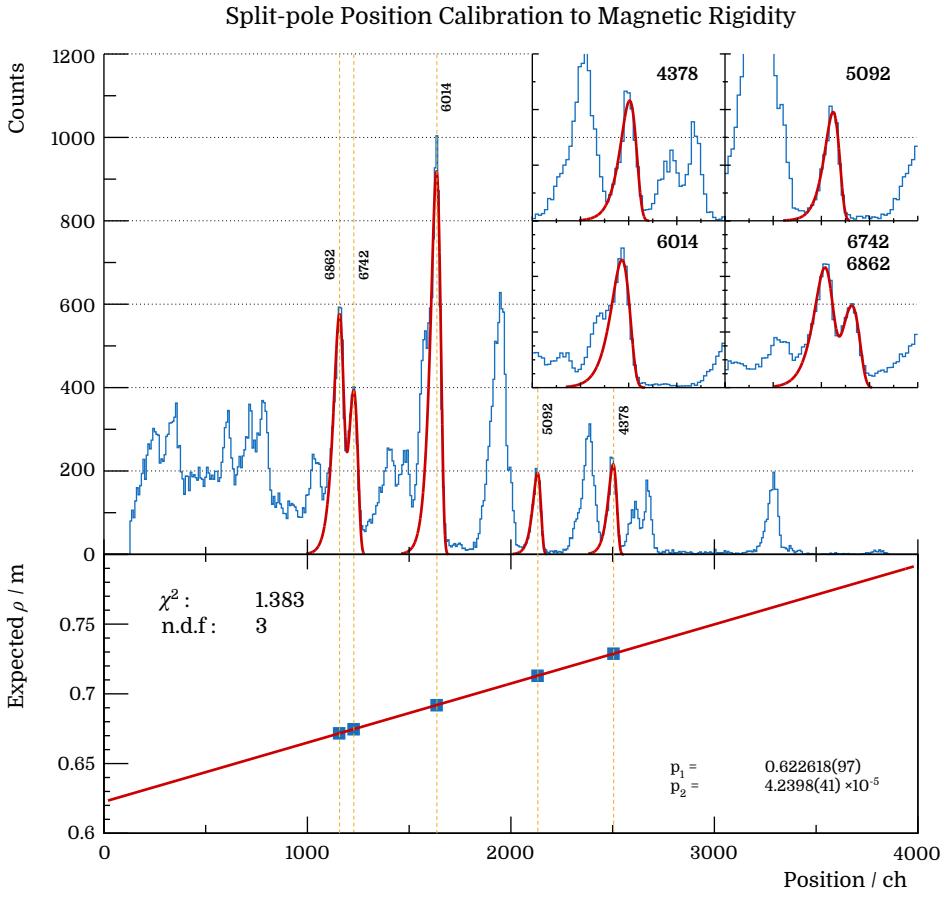

Figure 4.3: Upper panel: Uncalibrated Split-pole focal plane gated on tritons. The inset shows the peaks fitted to isolated states in ^{19}Ne. Lower panel: Corresponding peak centroid against the calculated value of ρ.

There are a number of isolated states in ^{19}Ne that have well known energies and are confirmed to be preferentially populated in the reaction of interest. A single run with sufficient statistics and a stable magnetic field in the Split-pole was chosen to find the channel position for each peak. Using two-body kinematics (described in detail in Appendix A) the expected orbital radius (ρ) was calculated, where B was equal to the average field strength of the chosen run, and compared to the channel number. Fig. 4.3 shows the peaks fitted for the calibration and their relationship to the expected value of ρ. The shape of the peaks is discussed later in section 4.4.1 The calibration is then applied to each Split-pole event using the equation

$$B\rho = \Big[\text{Offset} + (\text{Gain} \times \text{channel})\Big] \times B \ . \tag{4.1}$$

As mentioned in section 3.3.3 the magnetic field in the Split-pole can drift over the course of the experiment and even over each run reducing the resolution. The magnetic field term in eq. 4.1 corrects this drift when calibrating. The usual procedure for this correction is to apply the calibration event by event and confirm the change by plotting Pos against time where each peak position should remain 'flat'. However, because the field drift was so gradual over the experiment (Fig. 4.4), it was unnecessary to compensate for the small changes within each run. As such, the average field value from each run was used.

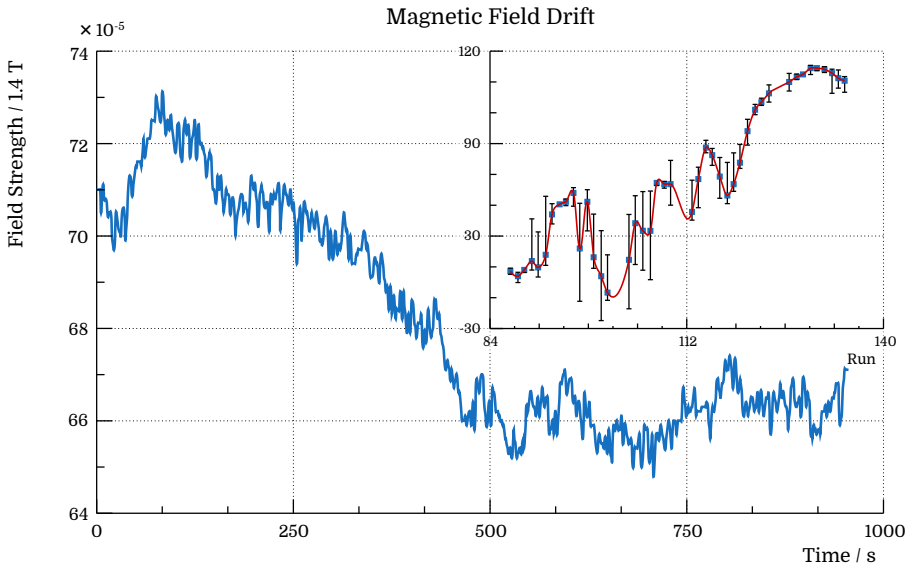

Figure 4.4: Magnetic field recording for run no. 111. The field has a maximum drift of 8×10^{-5} which is too small to correct for. Inset is the field drift across all runs. Whilst overall drift was on the order of 10^{-4}, individual variation for each run was limited to $\sim 10^{-5}$.

4.2.2 Silicon

Additionally, each strip of the six W1 silicon detectors required calibration to known energy values. To this end, a pulser module was used to simulate signal inputs into the preamplifiers at an amplitude reducing from 9 to 1 V (known as a pulser walkthrough). An example of an uncalibrated pulser spectrum is shown in the upper plot of panel **a** in Fig. 4.5. The channel number of each peak was plotted against the amplitude of the pulse (below) and a linear fit applied. Extrapolating the fit to 0 gave the offset value of each strip.

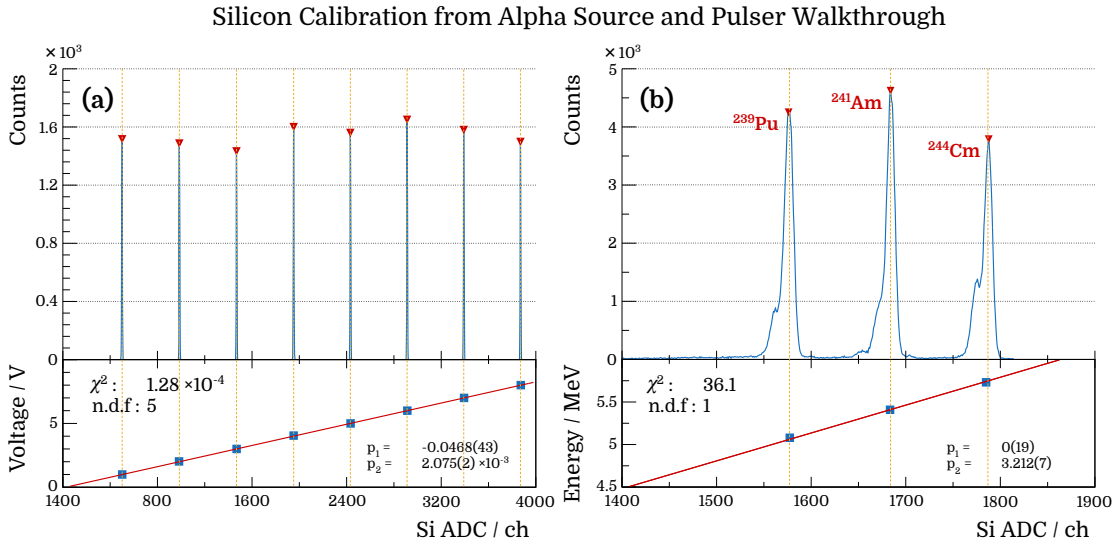

Figure 4.5: Silicon energy calibration using artificial pulses to obtain the electronic offset (panel **a**) and α-decay to measure the gain factor (panel **b**). The lower plots show the fit to ADC channel against expected value.

To account for distortions in the current read by each strip in the silicon wafer itself, signals originating from the α-decay of ^{239}Pu, ^{241}Am and ^{244}Cm (known as a triple alpha-particle source) were analysed. The source was fixed to the target ladder for approximately 12 hours for each calibration performed. The data were sorted, applying the offset from the pulser walkthrough in summation, and the peak positions from the spectra plotted against the precise energy of each α-particle decay. An example spectrum (upper) and linear calibration fit (lower) are shown in panel **b** of Fig. 4.5. Note that the smaller peaks were due to decay to excited states in the daughter nucleus and have not been used for calibration because of the lower statistics. The intercept parameter of the linear fit was fixed to 0 whilst the gradient (equivalent to the gain) was left free.

The measured offset and gain were applied to subsequent silicon data using the formula

$$E = (\text{channel} - \text{Offset}) \times \text{Gain} \ , \tag{4.2}$$

the result of which can be seen in panel **(a)** of Fig. 4.6.

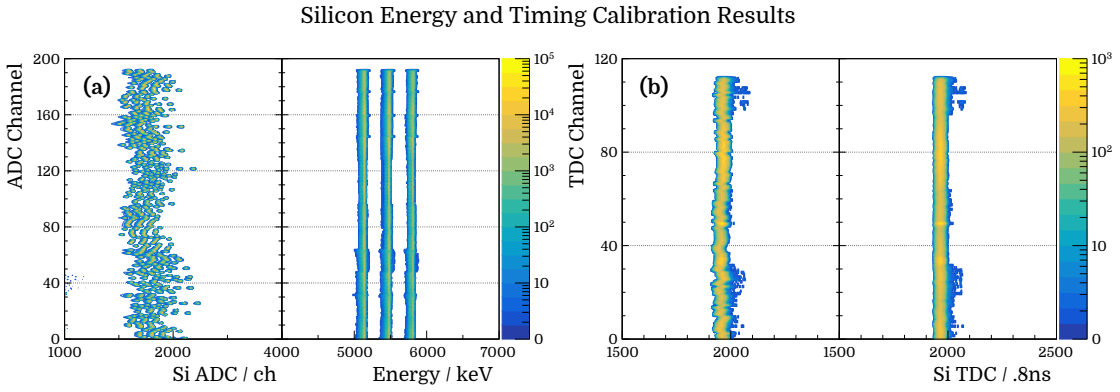

Figure 4.6: Effect of applying the energy (**a**) and time (**b**) calibration to triple α-particle source data. The left matrix shows before and the right shows after the calibration.

Silicon Dead Layer

Table 3.2 lists the silicon detectors used during this experiment. Two types of electrical contact were used; planar and grid, each with differing thicknesses. To improve the energy calibration, the energy losses of the alpha and proton particles passing through this 'dead layer' had to be accounted for. The measurement of the dead layer thickness was performed after the experiment in the nuclear labs at the University of York. The detectors were placed at 90° and 45° degrees to an alpha-particle source (to present differing depths of dead layer) and the energy of each isotope decay measured. Using the program SRIM (Stopping Range of Ions in Matter) to estimate the stopping power of alpha-particles through silicon, the energy difference between each detector orientation equated to the distance travelled by the particle. Simple trigonometric calculations produced the dead layer thickness for each detector that could be used in the calibration to 'add back' the lost energy according to the loss predictions from SRIM.

Timing Calibration

The values provided by the TDCs were calculated electronically where each channel was equivalent to 0.8 ns, thus there was no gain factor to consider. An arbitrary value for the central TDC channel was chosen to normalise against and the offset required for each strip determined from the peak centroid position difference. Whilst quantifying the time for each silicon detection was unnecessary, centralising the peak position simplified the data sorting process later. Fig. 4.6 shows the silicon energy (**a**) and silicon self-timing (**b**) against strip number.

4.3 True Event Conditions

Not all signals generated by the detectors and stored in the ROOT tree are considered true coincident reaction products. Hits in the Silicon array and Split-pole had to meet certain requirements in order to qualify. Fig. 4.7 shows the sequence of conditional statements required to sort the data into physical and non physical events. With the exception of triton identification (mentioned in section 4.2.1) each statement is discussed below.

```
Loop over events
  Loop over adc Multiplicity (5x SP Elements)
      If Check for 5 Split-pole elements
      If Within Triton Cuts
         Plot Focal Plane Spectrum (Singles)
    Loop over adc Multiplicity (2x Si Front and Back)
      Loop over tdc Multiplicity
         If Check for tdc element
         If Corresponding Front Back Hit in Detector
         If Equal Energy
         If adc/tdc Correlation
         If Si self timing peak
         If Alpha or proton locus
            Plot FP Spectrum (Alphas) (x12 Ang Bins)
            Plot FP Spectrum (Protons) (x12 Ang Bins)
```

Figure 4.7: Qualitative description of event selection sequence used in offline sort codes to gate on true coincidences. The three focal plane plots have been drawn in Fig. 4.11.

4.3.1 Extraneous Events

The first two conditions are used to remove events that do not have the relevant data for subsequent cuts and removing these at the top level expedited the sorting process. As all Split-pole elements were necessary to gate on tritons, events without data in all five branches were immediately rejected. The lack of signal detection in certain elements could be attributed to non-parallel particle trajectories generating signals below threshold from glancing interactions.

The measurement from the TDC is also crucial later in the sort code for identifying tritons and ^{19}Ne decays that originated from the same reaction. The window for ADC signals to be registered to the same event lasts for 5 μs, however the TDC timing window (Fig. 3.15) is limited to 2 μs. It was expected therefore that with a constant background of uncoincidental ^{19}Ne decays and β/γ decays from the faraday cup, approximately 60% of the data could be discarded immediately due to lacking timing information. Were even the timing recorded for these events, the discarded data would continue to be inadmissible under a later condition for being outside of the time of flight peak (section 4.3.4).

One final condition was that an event must contain at least one pair of hits in the Silicon array, both from separate sides from the same detector. Any other combinations of ADC channels were treated as background or noise.

4.3.2 Silicon Hit with Equal Energy

As the W1 detectors share the same silicon wafer between the front horizontal strips and the rear vertical strips, for every particle that ionizes the central depleted region, a signal of equal size is expected in both the front and back strips. For a proportion of the data however, the energies recorded in the front and back differ substantially. This can occur when a particle intercepts the detector within the interstrip region on one side but within the live area on the opposite side. The difference between the front and back energy was plotted and fitted with a standard Gaussian. Energy differences that were deemed too great were rejected (for the W1s used in this experiment a limit of 2σ was applied).

It was discovered during the post-experimental alpha-particle source calibration run that detectors 5 and 6 (see Fig. 3.7) had drifted in energy significantly since the initial calibration. The average energy difference (back subtracted from front) has been plotted against

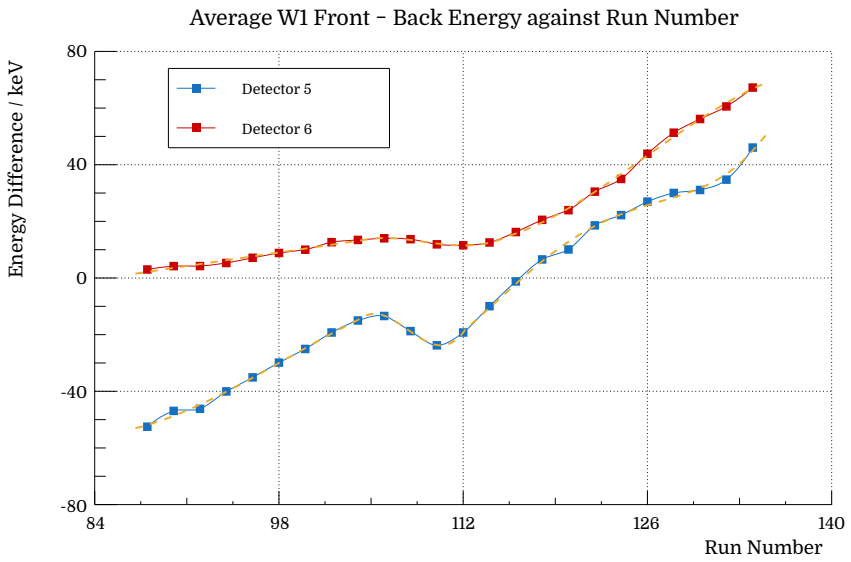

Figure 4.8: Mean energy difference between front and back signals against run number. Detectors 5 and 6 both exhibited drifts from their initial calibration over the course of the experiment. The approximate function used to describe the shift has been overlayed in yellow.

run number in Fig. 4.8. Given the close proximity of the detectors to the target foil, they likely experienced a greater flux of both ^{19}Ne decays and background radiation. This postulation is based on the general trend observed in Fig. 4.8 indicating residual charge held in the semiconductor, and also from the inverse drift seen during a period of lower beam intensity. Whilst unfortunate, the equal energy condition was easily modified to include this variation. The calibration was also affected, however the maximum energy difference observed was <100 keV and still allowed different decay particles to be distinguished.

4.3.3 ADC and TDC Correlation

As discussed in section 3.5.1, when a signal is processed by the shaping amplifier, both the amplitude and relative time of the signal are stored by the ADC and TDC respectively. It is important, therefore, when analysing the data to ensure that front/back hits in the silicon are only accepted if the corresponding TDC channel was also recorded in order to remove random noise from the system. From prior conditions, the data were already well correlated and this step removed only a small percentage of the total events.

4.3.4 Coincidence Timing

The crucial cut made to the data is on the time difference between the DAQ trigger and a particle detection in the silicon array. Whilst not strictly recording the flight time of the triton through the Split-pole, the term Time of Flight (ToF) is apt for describing the observed peak in the timing spectra. The DAQ configuration, discussed in the experimental setup, ensured that the ToF peak generated by silicon signals was centred in the TDC window after the DAQ was triggered by a triton. Fig. 3.15 shows the observed peak clearly above the coincident background. The peak was well described by a Gaussian distribution and events that resided within 2σ of the centroid were accepted.

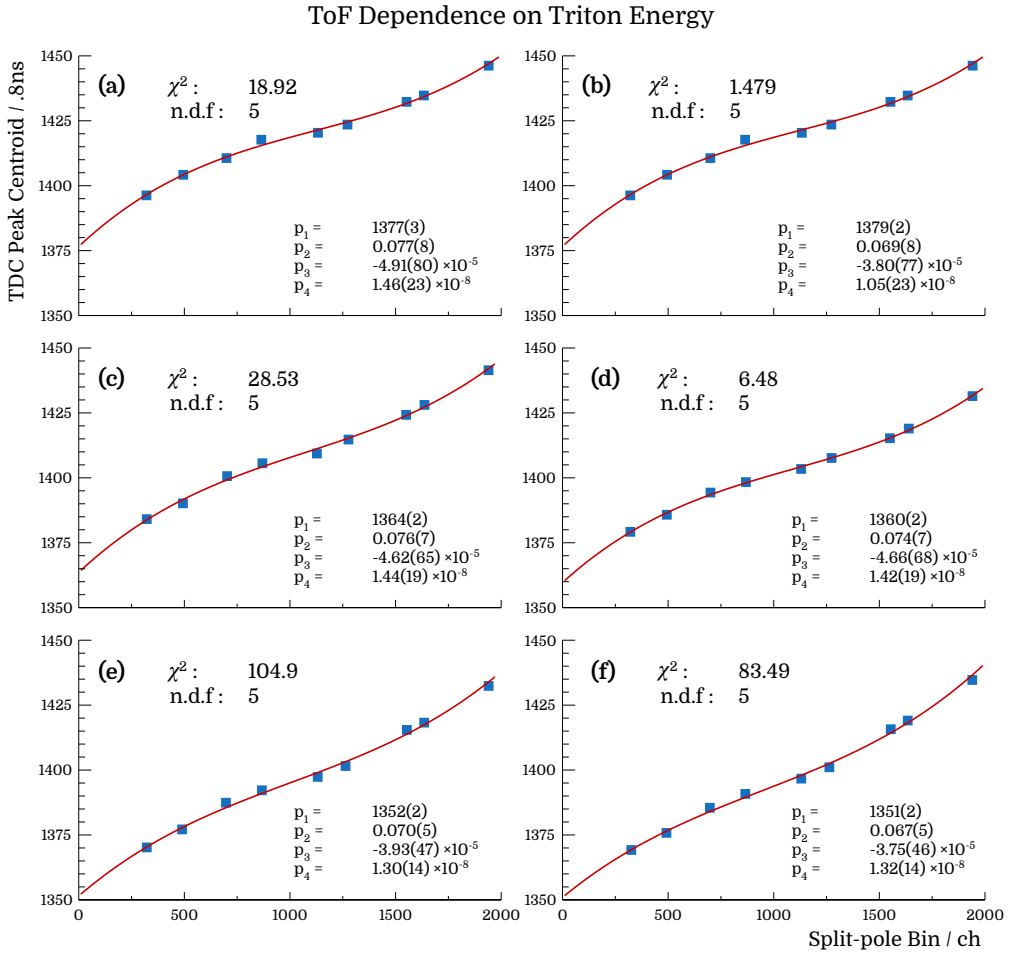

Figure 4.9: Measured timing peak centroid against Split-pole position (rebinned) for detectors 1-6 in panels **a-f** respectively. The 3rd order polynomial fit shows a predictable trend that unless accounted for would artificially lower the timing resolution to 60ns and introduce background events.

Whilst a single peak fit was acceptable for online analysis of the data, the resonance energy range of interest meant that the tritons would have a wide spread of orbital trajectories through the Split-pole. The ToF peak centroid would therefore contain a significant dependence on the triton energy. The Split-pole position spectrum was rebinned and the ToF peak position measured for events in each bin. Fig. 4.9 shows the ToF dependence on the position for each of the W1 detectors. It was important to find the individual dependence for each detector as their position inside the chamber had a bearing on the ToF recorded. Ideally, the dependence would be found for each pixel in the silicon array, however, the inherent timing resolution of the DAQ limited further improvement in accuracy.

The simulation of the reaction (discussed in section 3.4.3) estimated the correlation between the triton energy and the decay energy of the alpha and proton particles. After making the cut on the timing peak and removing the majority of the random coincident background, the alpha-particle and proton kinematic loci can be seen in an EvE plot very similar to that in Fig. 3.10. The EvE plot for detector 3 has been drawn below (Fig. 4.10) for events both including and excluding the ToF cut.

4.3.5 Kinematic Selection of Decays

The final cut made to the data was on the now exposed alpha-particle and proton loci. As calculated in the Monte-Carlo simulation, the particles measured in each detector pair have different energies due to the differing kinematics. Graphical cuts (see Fig. 4.10) made on the kinematic loci both separated protons from alphas and removed some of the residual background. Remaining background events are from beneath the ToF peak and can only be removed later. Projecting the Split-pole energy (position) for each cut, an estimate of the comparative decay strength for each state in ^{19}Ne can be seen in Fig. 4.11.

For this experiment, voltage thresholds on the shaping amps were set such that the majority of the low-energy background events were excluded from the data. The limit of this threshold is clearly visible from the EvE plot and shows the lowest populated state in ^{19}Ne for which decay detection was still possible. Unfortunately this meant that proton-decays from states of particular interest (near threshold) could not be observed. It should be noted, however, that proton yields from such states were expected to be very low and that, given the total beam time from the experiment, statistics would have been insufficient for accurate measurements of their branching ratios.

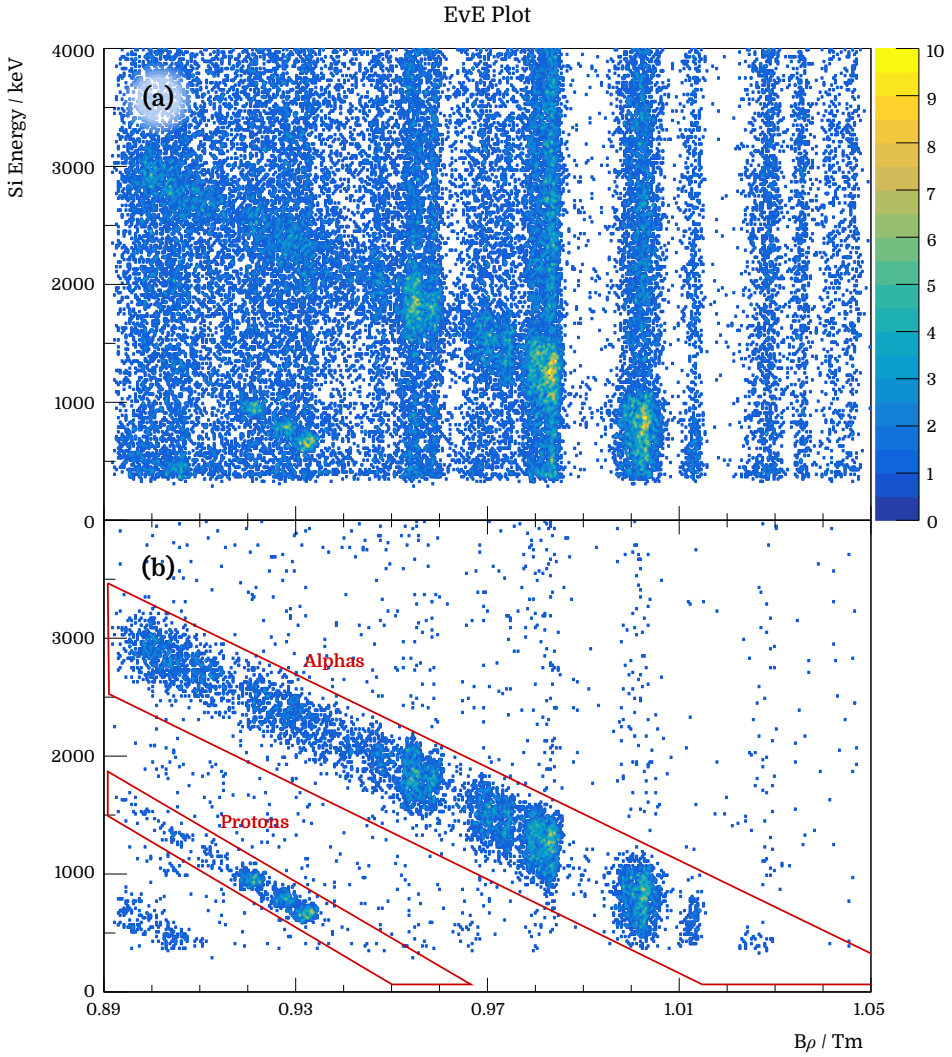

Figure 4.10: Silicon energy against Split-pole energy ($B\rho$) before (panel **a**) and after (panel **b**) the ToF cut is applied. Only data from a single detector (D4) have been shown to reduce the kinematic variation. Once the coincidental background has been removed, the alpha-particle and proton decays originating from ^{19}Ne become clear.

All events that met this final condition were considered true decay coincidences and were subsequently counted in the following analysis. If an event contained two distinct hits in the silicon where both met all the requirements, there was no further way of identifying the correct coincidence and the event was therefore discounted from both the triton and ^{19}Ne decay statistics. Approximately 0.5% of events after the last cut were removed because of this ambiguity.

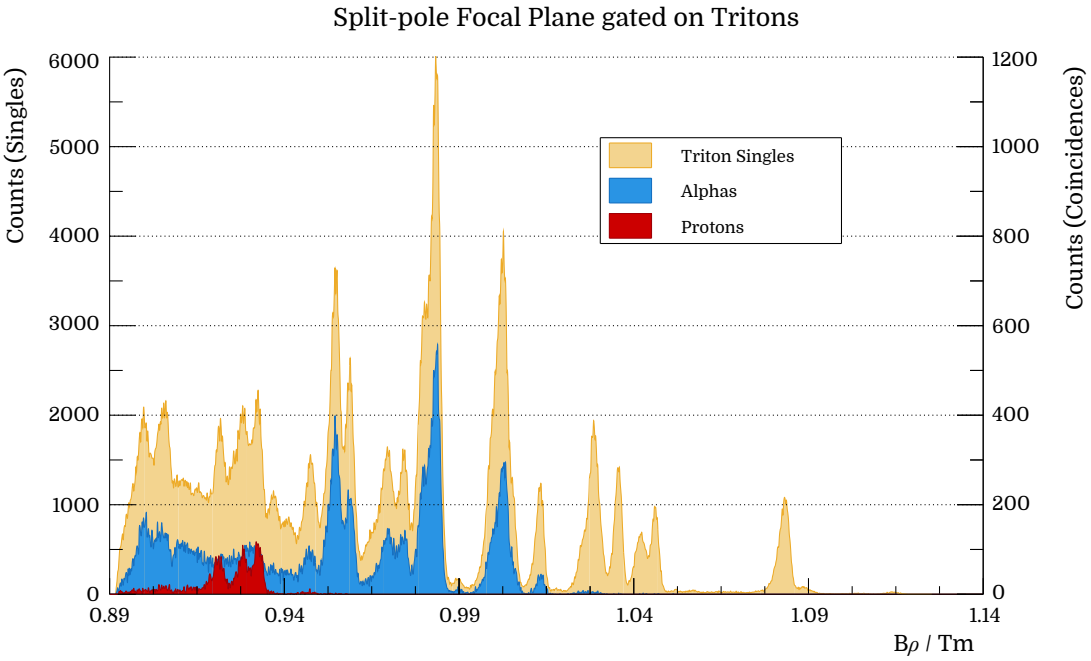

Figure 4.11: Split-pole focal plane showing the three plots referenced in Fig. 4.7: events proven to be tritons, events containing a proven α-particle detection and events containing a proven p detection. Coincident events have been scaled to better display the data.

4.4 Focal Plane Fit

After the singles and coincident spectra had been extracted from the data, a single function built from a series of individual peak functions was fit to the tritons coinciding with the populated states in ^{19}Ne.

4.4.1 Peak Asymmetry

Under normal operating conditions for the Split-pole, it is expected that the tritons originating from a single state would form a Gaussian distribution along the focal plane. As explained in section 3.6 it was necessary for the aperture slits in front of the splitpole to be opened to their widest setting in order to compensate in the loss of statistics from the lower beam intensity. The consequence of this was that the ejectiles from the same populated state had a different distribution when incident on the focal plane. Due to the wider acceptance of reaction kinematics, the tritons were not focused onto a single point thus lowering the Split-pole's resolution. The asymmetry of the aperture slits meant that

the analysed tritons also had an asymmetric distribution and could not be described by a single standard Gaussian function (see Fig. 4.12).

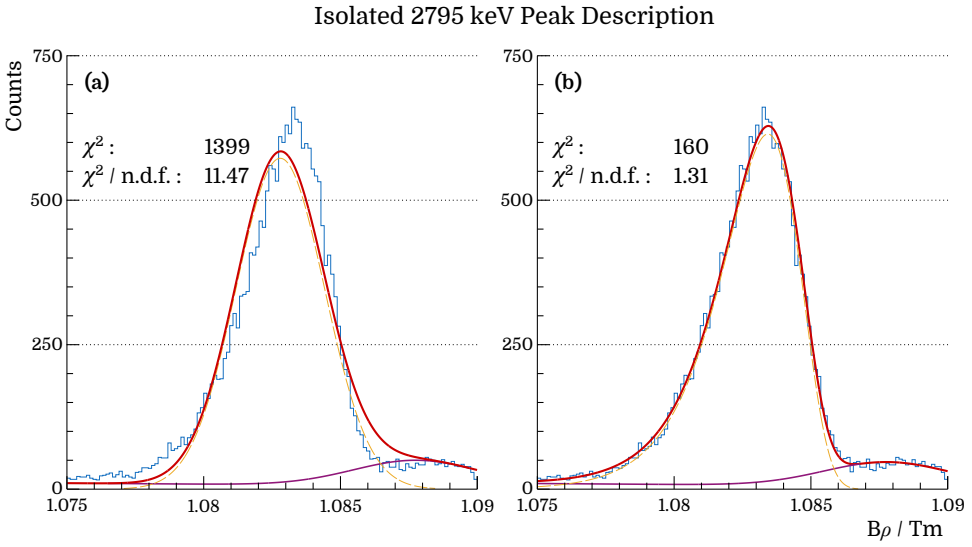

Figure 4.12: Focal plane spectra fit for the isolated 2795 keV state in ^{19}Ne. Symmetric and asymmetric functions have been used in panels **(a)** and **(b)** respectively.

The solution was therefore to apply either an exponentially modified Gaussian distribution, or a skewed Gaussian distribution function. From localising the fit to a single isolated peak, it was found that a skewed normal distribution best described the data with the following function,

$$f(x) = a \exp\left[\frac{\left(\frac{x-b}{c}\right) - e^{\left(\frac{x-b}{c}\right)}}{2}\right] , \tag{4.3}$$

where the peak height (a_0) and position (μ) are related to the parameters a, b and c by the following,

$$a_0 = \frac{2a}{e} , \tag{4.4}$$

$$\mu = b + c\ln(2) . \tag{4.5}$$

The standard deviation (σ) of the peak however retains its usual relationship to the parameter c. It was expected that for states with widths significantly larger than that of the Split-pole resolution, the distribution of tritons on the focal plane would become more symmetric in nature and the additional exponential term in eq. 4.3 could be removed.

4.4.2 Deuteron Background Subtraction

As explained in section 4.2.1, every effort was made to remove the 'bleeding' deuteron background caused by an incorrect measurement of the particle's energy loss. Whilst cuts to the data removed the majority, the remaining background still had to be quantified when fitting both the singles and coincidence focal plane. The first step was to understand the physical composition of the background. In the same manner as Fig. 4.1 cuts were made to; the deuteron locus, just above the triton locus and just below the tritons. Fig. 4.13 displays the position spectra from the three cuts and shows that the background is proportional along the length of the focal plane (i.e. the effect is not limited to the most populated peaks originating from the ^{13}N, ^{17}F and ^{41}Sc ground states - see Fig. 3.17).

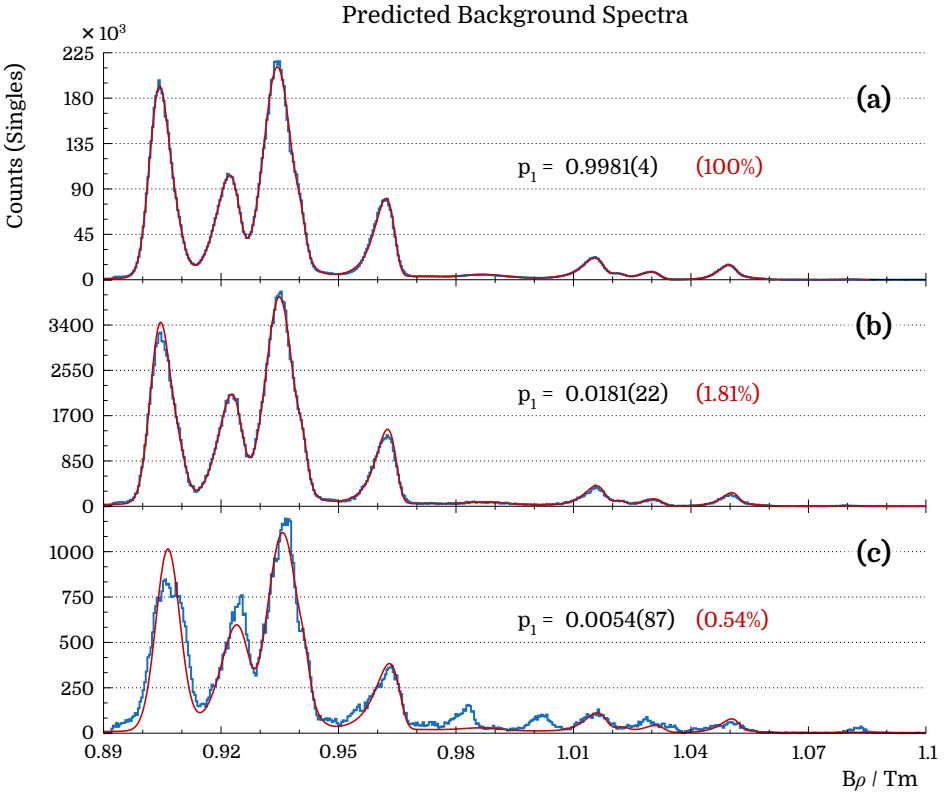

Figure 4.13: Focal plane position spectra gated on **(a)** deuterons, **(b)** 'above' the triton cut and **(c)** 'below' the triton cut. The background remains proportional across the entire focal plane and can be described using a re-normalised function used to fit the deuteron spectra.

The simplest way to quantify the background within the triton locus was to describe the deuteron spectra with a single function and include it into the triton fitting routine. The background function could then be re-normalised to its best-fit value. It was important

to estimate the intensity of the background to provide suitable boundary conditions for the normalisation parameter. Table 4.1 shows the normalisation (p_1) for a series of cuts (visualised in the corresponding Fig 4.14) made above and below the tritons in addition to the extrapolated value within the triton locus (BG).

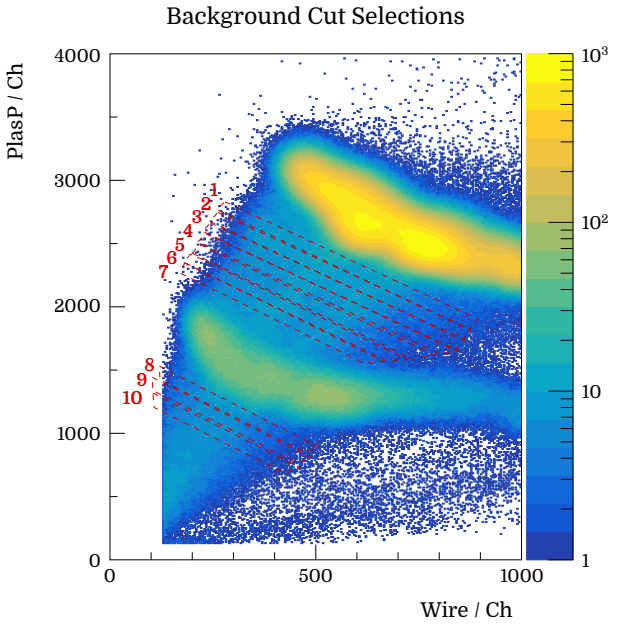

Figure 4.14: Cut sections taken between particle loci for characterising the deuteron background contribution.

Cut	Norm / %	Width / arb
1	0.390	66
2	0.367	66
3	0.352	66
4	0.328	62
5	0.293	68
6	0.225	65
7	0.196	64
BG	1.240	549
8	0.111	64
9	0.081	66
10	0.070	67

Table 4.1: Table showing measured deuteron bleeding and the extrapolated triton background.

4.4.3 Final Fit Routine

Given that the width of the majority of states in ^{19}Ne are below the resolution of the splitpole, the width (parameter c in eq. 4.3) was kept constant between all narrow states by confining to a single shared free parameter. Wide states were treated separately where width parameters were bounded by their currently accepted errors. The final function used to fit the triton position spectrum can be seen in Fig. 4.15 where the total function is highlighted in red, the individual states are highlighted in yellow and the background is in purple. The normalisation parameter for the background was minimised to 1.39% - an acceptable value close to that predicted in Table 4.1. Appendix D shows improvements to the fit at $B\rho = 0.965$ and 0.95 Tm from the inclusion of previously missing states. The states used in the fit function are listed in Table 1.2.

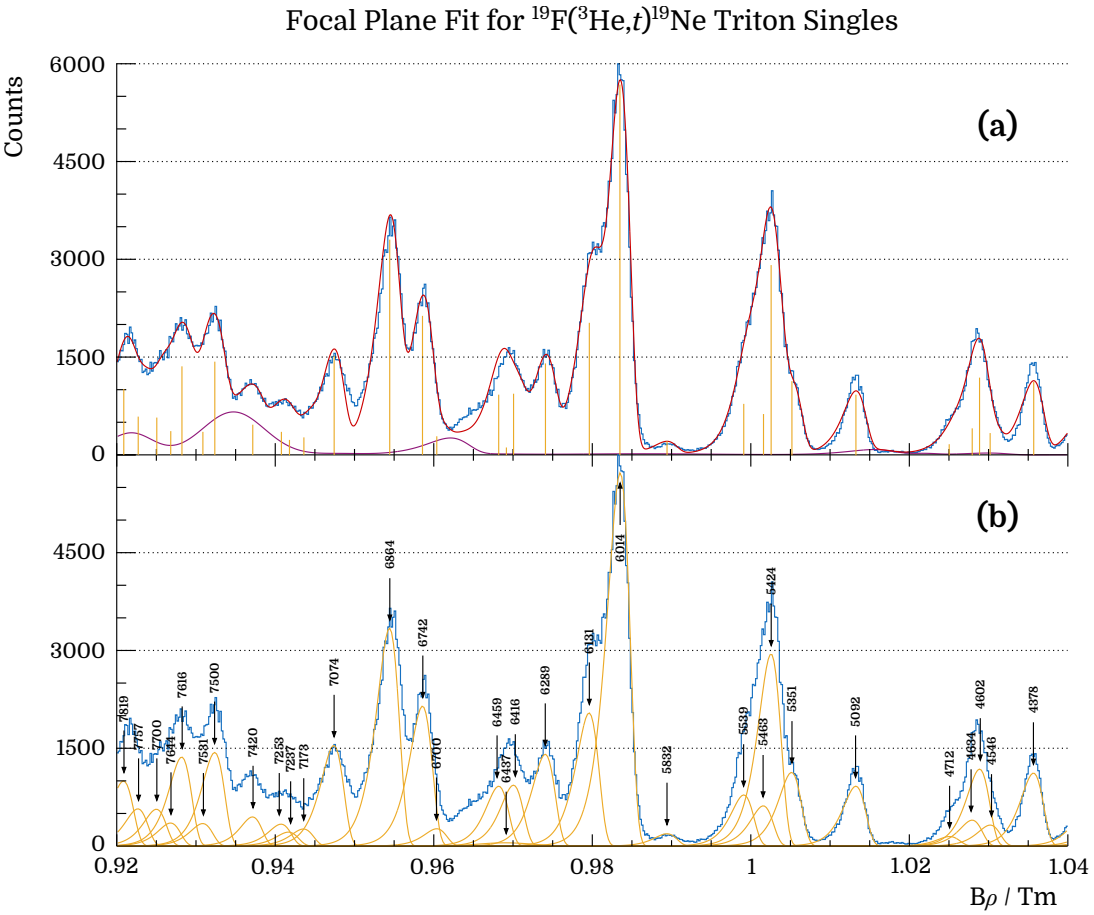

Figure 4.15: Final fit function for triton singles spectra. The top panel shows the total function in red with the deuteron background highlighted in purple. The lower panel shows the individual contributions from each state.

4.4.4 Broad Subthreshold $1/2^+$

Investigation into a postulated broad threshold [56] was only conducted midway through the data analysis. Following discussions with Boulay *et al.* [60] the region below the proton threshold was studied more closely during the focal plane fitting routine. As shown in panel **(a)** of Fig. 4.16, the region below the 6014 keV state could not be described well using only the listed states in Table 1.2. An additional 3 parameters were included in the routine to describe a broad state that, if the fit from Boulay is correct, is mostly hidden by the 6014 keV energy level.

The three parameters were set to those measured in ref. [60] at the beginning of the fit routine but left free and unbounded. Initially the function was treated as a symmetric distribution, however from the first results of the fit and from the width calculation in ref.

[60], the width of the state proved close enough to the Split-pole resolution to warrant an asymmetric description. Panel **(b)** of Fig. 4.16 shows the results of the new fit function.

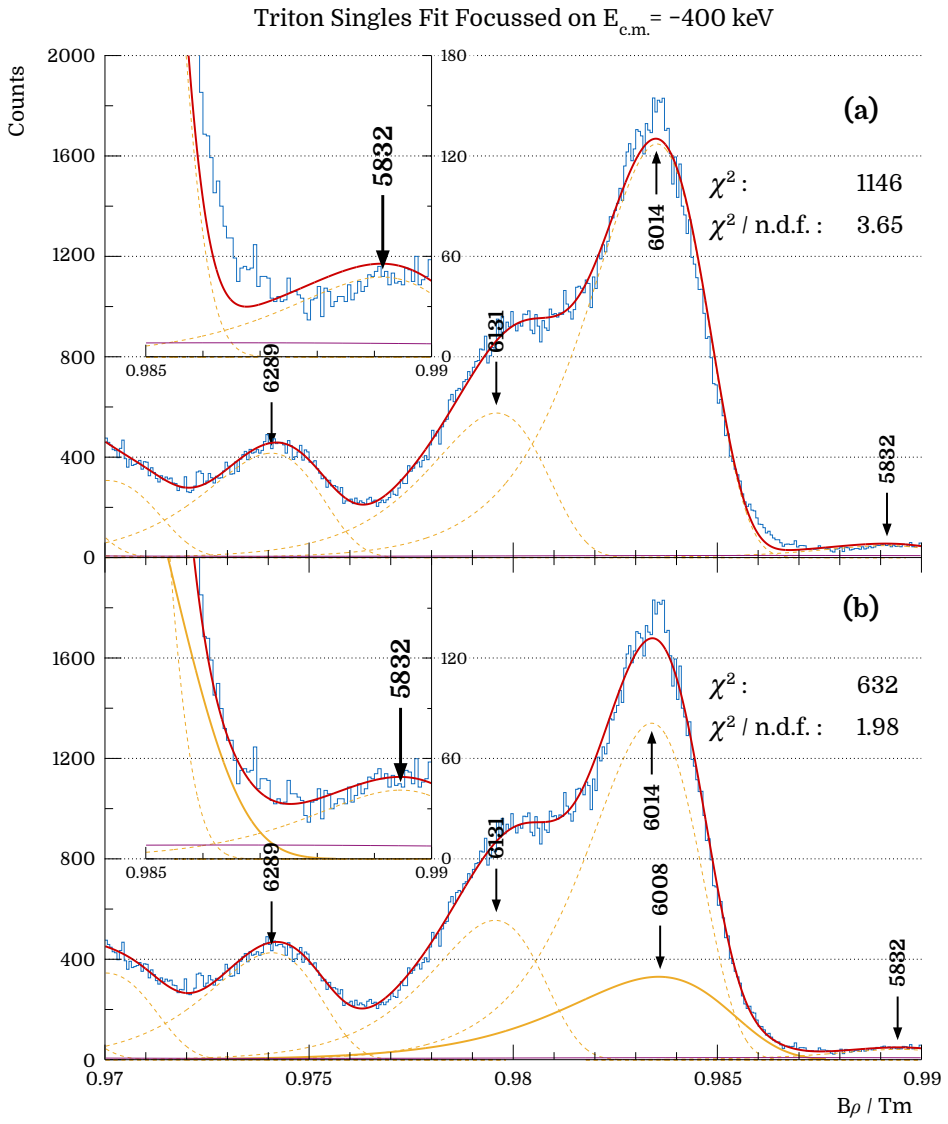

Figure 4.16: Fitted Split-pole focal plane spectra focused on the −400keV subthreshold region. The inclusion of a broad state with parameters close to those of a postulated energy level improves the fit probability considerably.

The reduction in the reduced χ^2 value from 3.65 to 1.98 is a strong indicator that the new state is present and populated to some degree by the charge exchange mechanism used in the experiment. The table below (Table 4.2) shows the state parameters postulated by Dufour & Descouvemont [56], those found by Boulay *et al.* [60] and the parameters extracted from the fitting routine in this work. A detailed discussion of this state has been provided in Chapter 6. Whilst the fitting procedure used for the coincidence spectra has not been discussed until the following section, it should be noted that when the same

parameters are applied to the α-particle coincidence spectrum, a similar improvement to the reduced χ^2 is observed changing from $\chi^2/\nu = 1.49$ to $\chi^2/\nu = 1.25$.

Dufour & Descouvemont [56]	E = 6001 keV	Γ_t = 231 keV
Boulay *et al.* [60]	E = 6020(13) keV	Γ_t = 110(29) keV
This work	E = 6008(20) keV	Γ_t = 124(25) keV

Table 4.2: Table listing the predicted and measured parameters for the broad $1/2^+$ subthreshold resonance in ^{19}Ne. The measurement for this work is in good agreement with the previous observation [60].

4.5 Angular Distributions

If each state were to decay isotropically, the only correction to apply would be the total silicon array efficiency and thus the branching ratios could be determined almost directly. However, as explained in section 2.4, it was expected that the majority of states decay via channels with non-zero values of orbital angular momenta, producing distinctive intensity distributions dependent on theta ($\theta_{\text{c.m.}}$). It was therefore necessary to re-bin the silicon array into distinct angular regions and count the decays detected for each. Due to the dependence of the reaction kinematics on the silicon geometric efficiency, simulations for each ^{19}Ne state of interest were conducted separately. An example of the angular binning used has already been mentioned in section 3.4.3 and shown in Fig. 3.9.

4.5.1 Coincidence Fitting

Once the singles spectrum was fitted accordingly, the parameters describing the width and mean of the ^{19}Ne states were duplicated and used in a secondary function to fit either the proton or alpha-particle coincidence spectra. The normalisations of each peak remained the only free parameters in the secondary fit in order to account for the variability of each state's decay channel intensity. Multiple coincident spectra, each gated on a single angular bin, were fit with the secondary function using the log likelihood method to alleviate the lower statistics caused by re-binning the spectra. Remaining with the 6864 keV state used to demonstrate the Monte-Carlo simulations, an example of the fitting process for the coincident spectra is shown in Fig. 4.17.

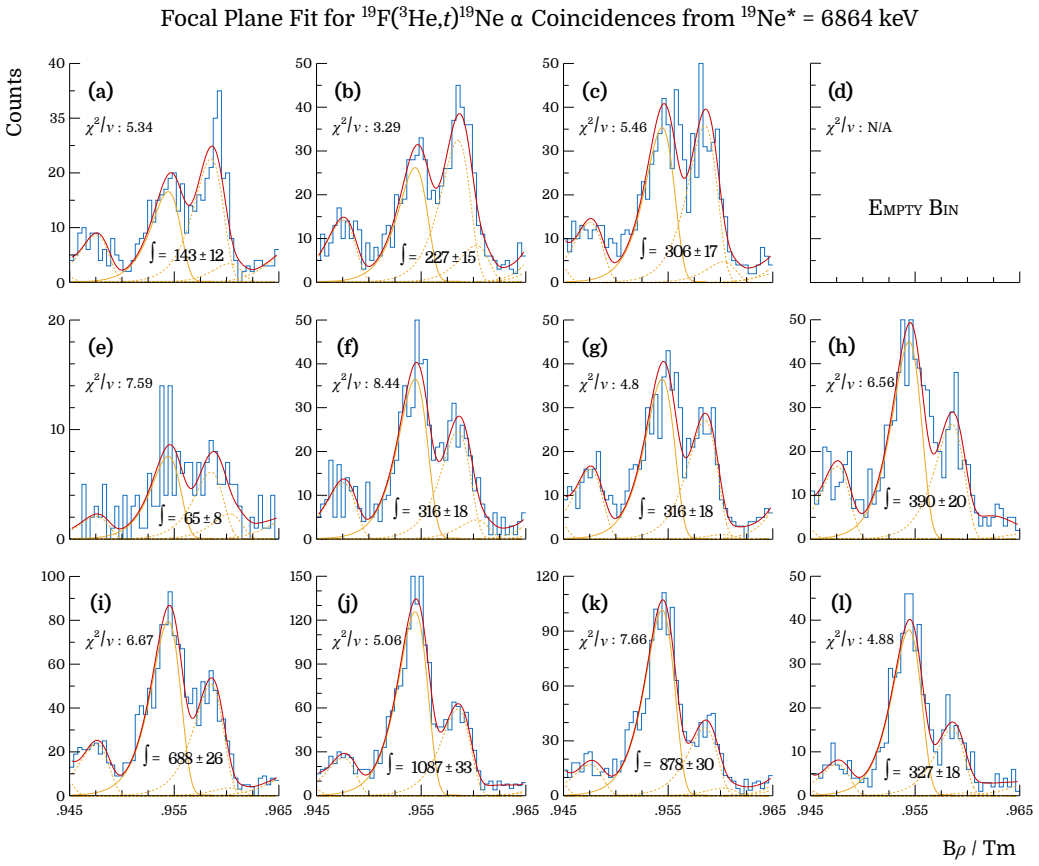

Figure 4.17: Fit function applied to 12 angular bins for coincident α-decay from the 6864 keV resonance. The statistics from the state of interest (indicated by the solid yellow line) have been calculated from the integration of each function between $\pm 2\sigma$. Bin no. 4 **(d)** spans the inter-detector region and as such contains no counts.

The coincident statistics (as shown in the example for 6864 keV) were calculated by inputting the fit parameters for the state of interest into eq. 4.3 and integrating between $\pm 2\sigma$. The error originating from the fit was found to be negligible and, therefore, not included in the subsequent analysis (section 4.5.4).

4.5.2 Coincidental Coincidence Background

As mentioned in section 4.3.5, the timing cut used to select true coincident events within the ToF window also included background Si hits that happened to correspond with the flight time of the triton. These 'coincidental coincidences' could not be physically removed from the data set and so had to be accounted for statistically. The background was therefore averaged within the Si timing spectra and integrated over the accepted ToF region.

The background intensity was significantly dependent on the properties of each W1 detector, specifically their thickness, the shaping amp. energy threshold and their placement within the chamber. An appropriate background level therefore needed to be found for each angular bin. Due to earlier simplifications of the sort code, only hits accepted as true coincidences were assigned angular coordinates. This prevented the ToF spectra from being drawn gated on each bin. The solution was therefore to draw the spectra for each detector gated on the state of interest, calculate the background and subtract the proportion of background counts from the angular bin total depending on the proportion of the detector visible in that angular range (repeated for each detector). The code used has been displayed in Appendix B.

4.5.3 Reaction Normalisation

Rather than plotting the absolute values of the ^{19}Ne decay statistics, the angular bin values were chosen to be normalised against the triton singles counts calculated from integrating the states peak in the singles focal plane fit between $\pm 2\sigma$. This, in principle, would allow the overall normalisation of the angular distribution fit to remain proportional to the decay probability for that channel (i.e. the alpha-particle or proton branching ratios) and not on any population preference caused by the (^{3}He,t) reaction. This will be discussed in greater detail in section 4.6.3.

4.5.4 Error Propagation

Accounting for the various corrections and calculations made to the statistics, the error associated with the data point for each angular bin was determined via the following sequence (the code for which has been included in Appendix B).

1) **Coincidence Fit**	Statistical error ($\sqrt{n}$).
2) **Background Subtraction**	Absolute error from background estimate added in quadrature.
3) **Efficiency Normalisation**	Fractional error from ϵ_{geo} added in quadrature.
4) **Reaction Normalisation**	Fractional error from singles statistics ($\sqrt{n}/n$) added in quadrature.

4.6 Results

Using the angular distribution theory for particle decay as discussed in section 2.4, the distribution plots for selected states were fitted with a series of Legendre polynomials (eq. 2.38). The highest polynomial term (k_{max}) signifies the orbital angular momentum carried away by the decay channel (equal to twice its value, $2l$) and the coefficients for each term contain information on the magnetic substate populations and competing channel spins.

For several reasons, not all resonances used in the focal plane fit for the t singles have been analysed in the distribution plots. Firstly, resonance decays with α-particle and p decay energies close to or below the silicon detection threshold (see Fig. 4.10) evidently cannot be plotted in coincident spectra. This has prevented states below 5.7 MeV and 7.2 MeV, decaying via α-particle and p emission respectively, from being analysed. Crucially this prevented the 7076 keV ($E_{c.m.} = 665$ keV) Γ_p measurement. Additionally, the isolation of coincident decay spectra for a single state was not always possible due to a lower Split-pole resolution than expected and, for states above 7.0 MeV, an increase in level density. Finally, states of particular interest didn't always contain sufficient statistics. Whilst the bin count was reduced to compensate, this limited the maximum polynomial order for the fit, inhibiting the analysis of high spin, low count states.

The following sections detail the distributions and subsequent polynomial fits for those resonances that could be meaningfully observed from the experiment. Discussion of these states is limited to just the fitting procedure and further analysis is given in Chapter 6.

4.6.1 Angular Distributions Below $E_x = 6411$ keV

6014 keV ($E_{c.m.} = -397$ keV)

The 6014 keV state was the most populated within the focal plane limits and, whilst unimportant for the $^{18}F+p$ nova reaction rate (Chapter 5), was a good test for the analytical methods used in this work. It is known to have a J^π of $3/2^-$ [52] implying an l value for the α-decay of 2. As the distribution in Fig. 4.18 shows, the best description arises from $k_{max} = 4$ with a reduced chi-squared (χ^2/ν) of 0.89. Use of higher order terms result in either a coefficient of 0 (i.e. the polynomial order is not used) or an increase in χ^2/ν. Note that the error in $\theta_{c.m.}$ for Fig. 4.18 - 4.25 is attributed to the width of the bin.

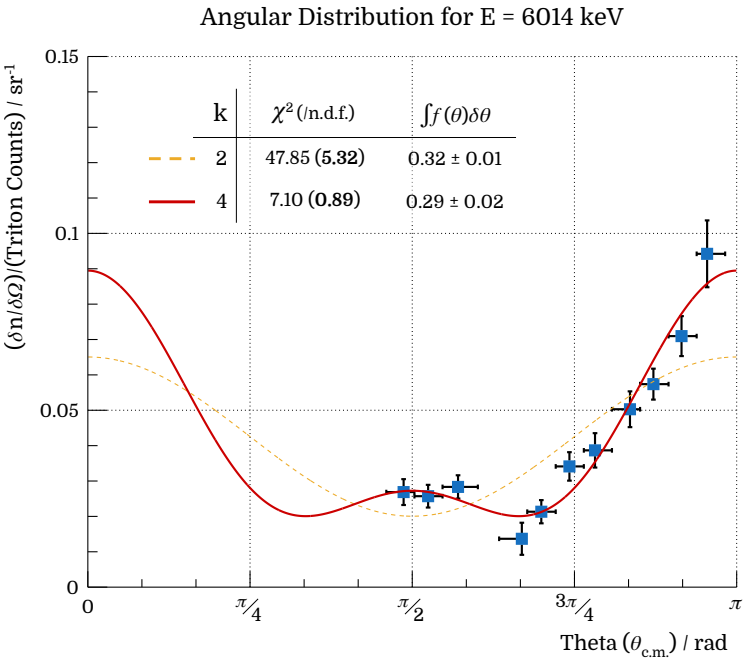

Figure 4.18: 6014 keV α-decay angular distributions separated into 12 bins (bin no. 4 lies between detectors). Implies a spin of $J^\pi = 3/2^-$ or $5/2^-$.

6289 keV ($E_{c.m.} = -122$ keV)

Fig. 4.19 shows the distribution from the 6289 keV state separated into 9 angular bins. The data are difficult to describe and only when $k_{max} = 10$ does the fit become acceptable.

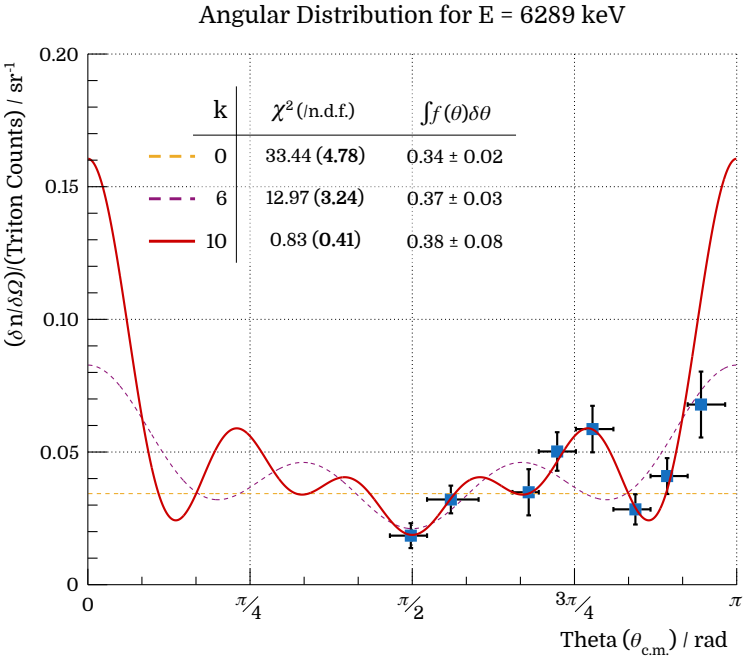

Figure 4.19: 6289 keV α-decay angular distributions separated into 9 bins (bin no. 3 lies between detectors). Implies a spin of $J^\pi = 9/2^+$ or $11/2^+$.

As the number of free parameters in the function (6) was close to the number of data points, the silicon array was rebinned into 12 angular regions (not shown) despite the lower statistics to confirm the fit parameters. The fit returned an almost identical function with a slightly higher χ^2/ν of 1.27. The data were also fitted with values of $k_{max} = 12$, 14 and 16, however they returned a χ^2/ν of 1.58, 1.52 and 2.28 respectively.

Whilst the distribution could potentially be described as isotropic as would be indicitive of $J^\pi = 1/2^-$ (shown in Fig. 4.19), the fit likelihood and the periodic, rather than random, nature of the data, imply that this is very unlikely to be the case.

4.6.2 Angular Distributions Above E_x = 6411 keV

6742 keV ($E_{c.m.}$ = 331 keV)

The first resonance above the proton threshold to be meaningfully analysed was that of the 6742 keV state, previously been measured to have a J^π of $3/2^-$ [26] like the 6014 keV state before. A comparison of fits to the α-decay distributions are shown in Fig. 4.20 where the best fit, having a χ^2/ν statistic of 0.41, is from the $l = 2$ ($k_{max} = 4$) legendre polynomial function. Reassuringly, the distribution is identical to that of the 6014 keV.

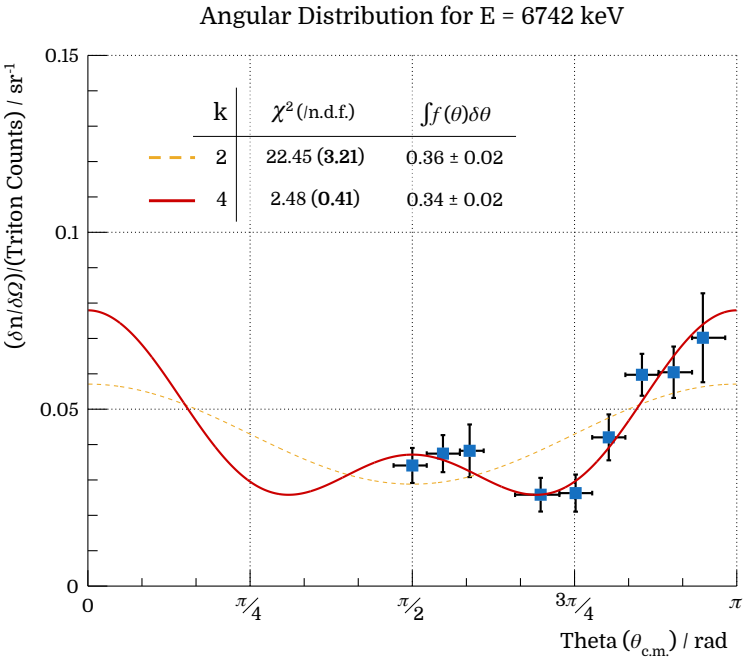

Figure 4.20: 6014 keV α-decay angular distributions separated into 10 bins (bin no. 4 lies between detectors). Implies a spin of $J^\pi = 3/2^-$ or $5/2^-$.

6864 keV ($E_{c.m.}$ = 453 keV)

The 6864 keV state is the second resonance above threshold that can be unambiguously identified. It is thought to be the isospin analogue of the $J^{\pi} = 7/2^{-}$, E = 6927 keV state in ^{19}F [36] which, according to Table 2.1, would therefore be expected to have a distribution matching $k_{max} = 8$. The angular distribution (see Fig. 4.21) is, however, suitably described using only four terms ($k_{max} = 6$) where the 5th term is always minimised to 0. This would therefore imply either a positive parity for the state or a lower spin of $5/2^{+}$.

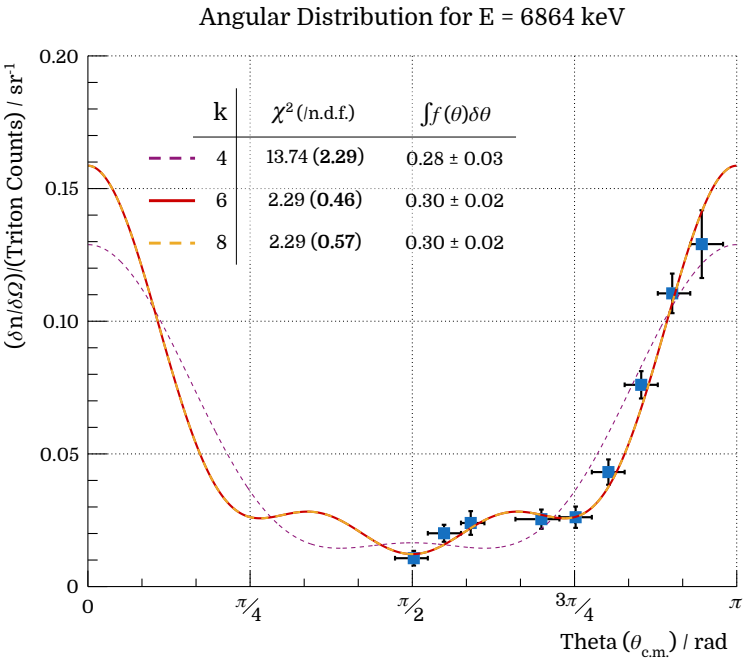

Figure 4.21: 6864 keV α-decay angular distributions separated into 12 bins (bin no. 4 lies between detectors). Implies a spin of $J^{\pi} = 5/2^{+}$ or $7/2^{+}$.

7076 keV ($E_{c.m.}$ = 665 keV)

The angular distribution data for α-decay from the 7076 keV state are shown in Fig. 4.22. The state has been well studied and is known to have a spin parity of $3/2^{+}$. The $l = 1$ (k_{max} = 2) function fitted in the figure is a clear improvement over the isotropic description, indicating an agreement with its known spin-parity. This $E_{c.m.}$ = 665 keV resonance was one of the states of particular interest to this experiment. Unfortunately, p-decay from the state was only partially observed[1] and only in D1&2 preventing a comprehensive description of its distribution or decay rate.

[1] Shaping amp. energy thresholds lay in the centre of the locus for proton decay energies.

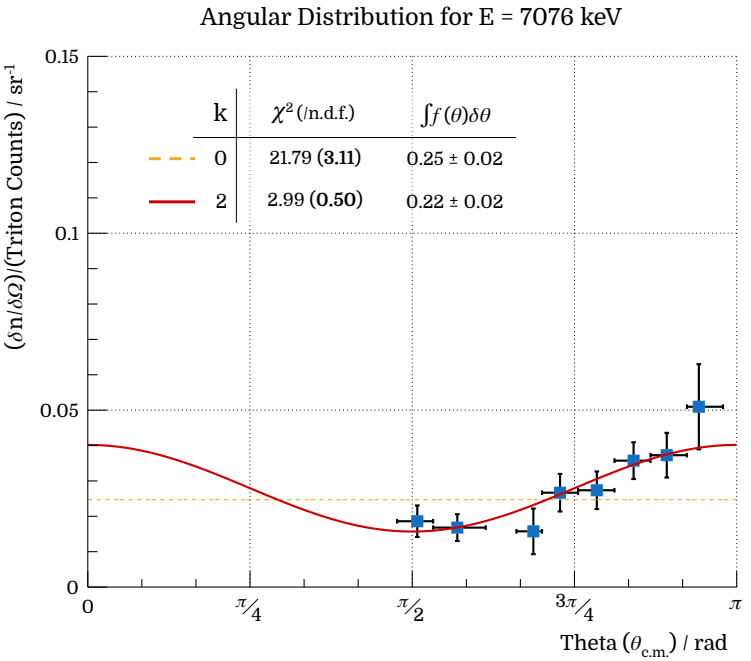

Figure 4.22: 7076 keV α-decay angular distributions separated into 9 bins (bin no. 3 lies between detectors). Implies a spin of $J^\pi = 1/2^+$ or $3/2^+$.

7420 keV ($E_{c.m.} = 1009$ keV)

The 7420 keV state is known to be of spin $7/2^+$ [39], agreeing with the α-particle distribution from this work (Fig. 4.23) that required a $k_{max} = 6$ function to fit the data.

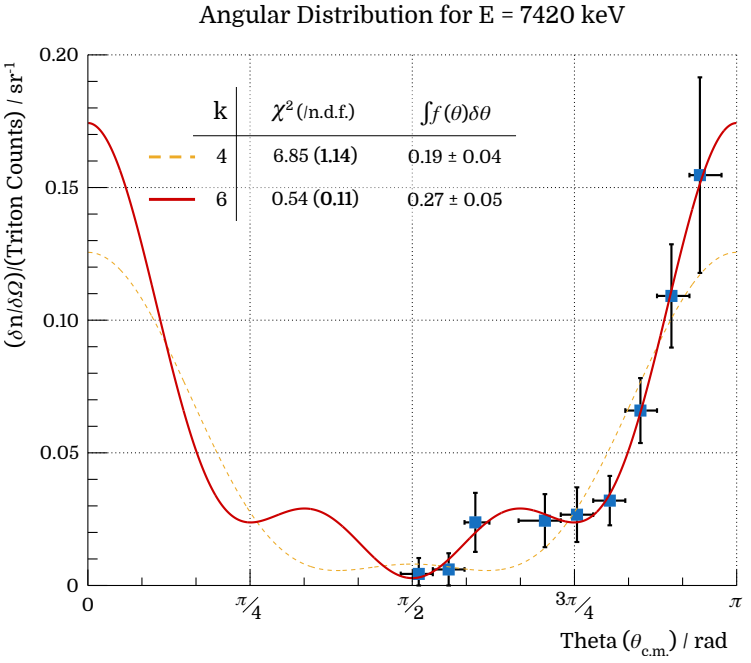

Figure 4.23: 7420 keV α-decay angular distributions separated into 10 bins (bin no. 4 lies between detectors). Implies a spin of $J^\pi = 5/2^+$ or $7/2^+$.

The shape of the fit is the same as that from the 6864 keV angular distribution which, as previously stated, is expected to be of spin $7/2^-$. Given the similarity between the two, this adds further support to the suggestion of a parity reassignment to the 6864 keV state. The 7420 keV was not observed in the direct reaction by Murphy *et al.* [59] and concluded not to exist. Fig. 4.15 shows that no other state in the region ($B\rho \simeq 0.9375$) could constitute the observed peak in the data. In addition this work's J^π assignment, consistent with the state's previous measurement, adds support to its existence.

7500 keV ($E_{c.m.}$ = 1089 keV)

The first state with sufficient p-decay strength to be measured in this work was the 7500 keV state. Previous analysis has shown the state to be $5/2^+$ [59] which would imply a distribution function of $k_{max} = 6$ for the α-particle and $k_{max} = 4$ for the p decay (assuming only the lowest l-value channel is taken). Fig. 4.24 shows the agreement of the data with the expected distribution function for both the α-particle, **(a)**, and proton, **(b)**, decay.

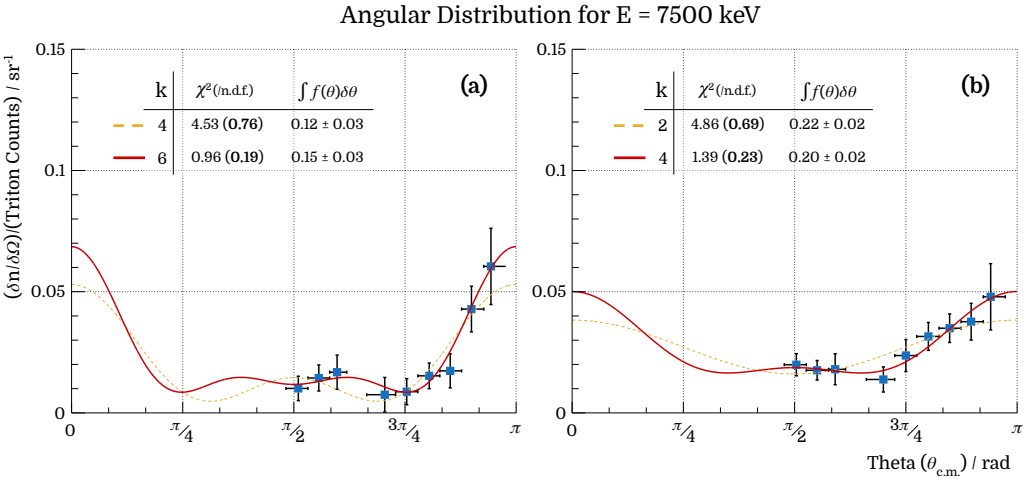

Figure 4.24: 7500 keV angular distributions for **(a)** α-decay and **(b)** p-decay separated into 10 bins (bin no. 4 lies between detectors). Implies a spin of $J^\pi = 5/2^+$ or $7/2^+$ (for higher l-values $J^\pi = 1/2^+$ or $3/2^+$).

7616 keV ($E_{c.m.}$ = 1205 keV)

The 7616 keV state was the highest energy state for which angular distributions could be successfully extracted. Both the α-particle and p angular distributions could be measured although, due to infringing states and lower statistics, branching ratios would have been

spuriously calculated. Known to be $3/2^+$ the state was expected to decay with an l-transfer of 1 for the α-decay ($k_{max} = 2$) and 0 for the p-decay ($k_{max} = 0$). Both of the expected distributions are reproduced by the data in Fig. 4.25.

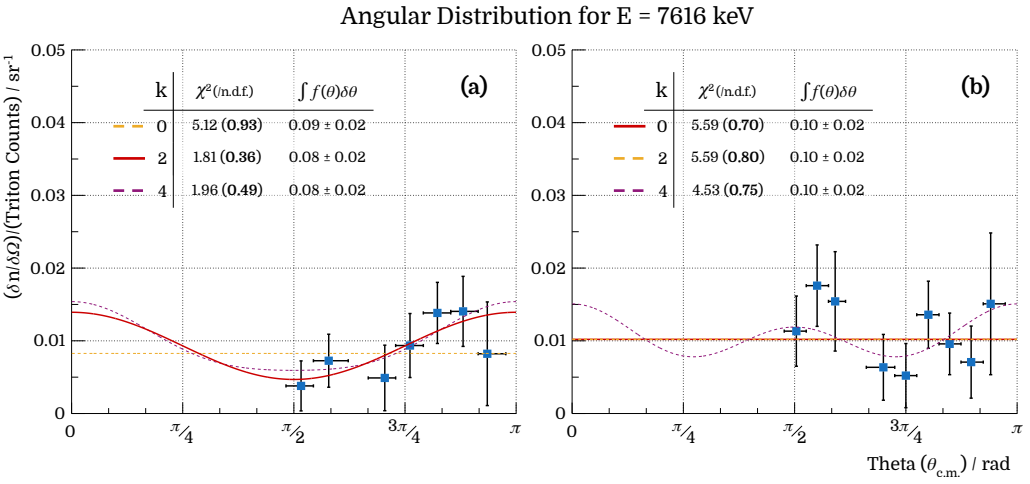

Figure 4.25: 7616 keV angular distributions for **(a)** α-decay and **(b)** p-decay separated into 8 and 10 bins respectively (bin no. 3 and 4 lie between detectors). Implies a spin of $J^\pi = 1/2^+$ or $3/2^+$.

4.6.3 Branching Ratios

The counts in each angular bin were normalised to the counts measured in the triton singles spectrum, i.e. the angular distribution data show a comparison between the number of decays detected and the number of times the state in ^{19}Ne was formed. The normalisation is such that extrapolating and integrating $W(\theta_{\text{c.m.}})$ over 4π sr (see eq. 4.6) for each level yields the branching ratio ($b_{p,\alpha}$) for the decay from the measured channel

$$b_{p,\alpha} = \int_{\theta=0}^{\pi} 2\pi \sin(\theta) W(\theta) d\theta \ . \tag{4.6}$$

The results from the integration of each function displayed have been shown in Fig. 4.18 - 4.25 alongside their χ^2/ν value. The quoted uncertainties for each calculated branching ratio originates from the uncertainties in the fit parameters. Surprisingly, however, the calculated ratios are well below their expected rates. For example, the 6864 keV state is known to decay via α-particle emission 92.5% of the time, whereas the value extracted from this data set place the ratio at 30(2)%.

A study of ^{19}Ne made by Visser *et al.* [82, 83] at Yale University used a similar technique of coincident triton and α/p measurement and found decay branching ratios, after normalisation, in agreement with the existing literature. A comparison of the two data sets has been made in Fig. 4.26 for the 6742, 6864, 7076 and 7500 keV states measured in both experiments. The inconsistencies in branching ratios are clearly not continuous and have a dependence on excitation energy which complicates the problem significantly.

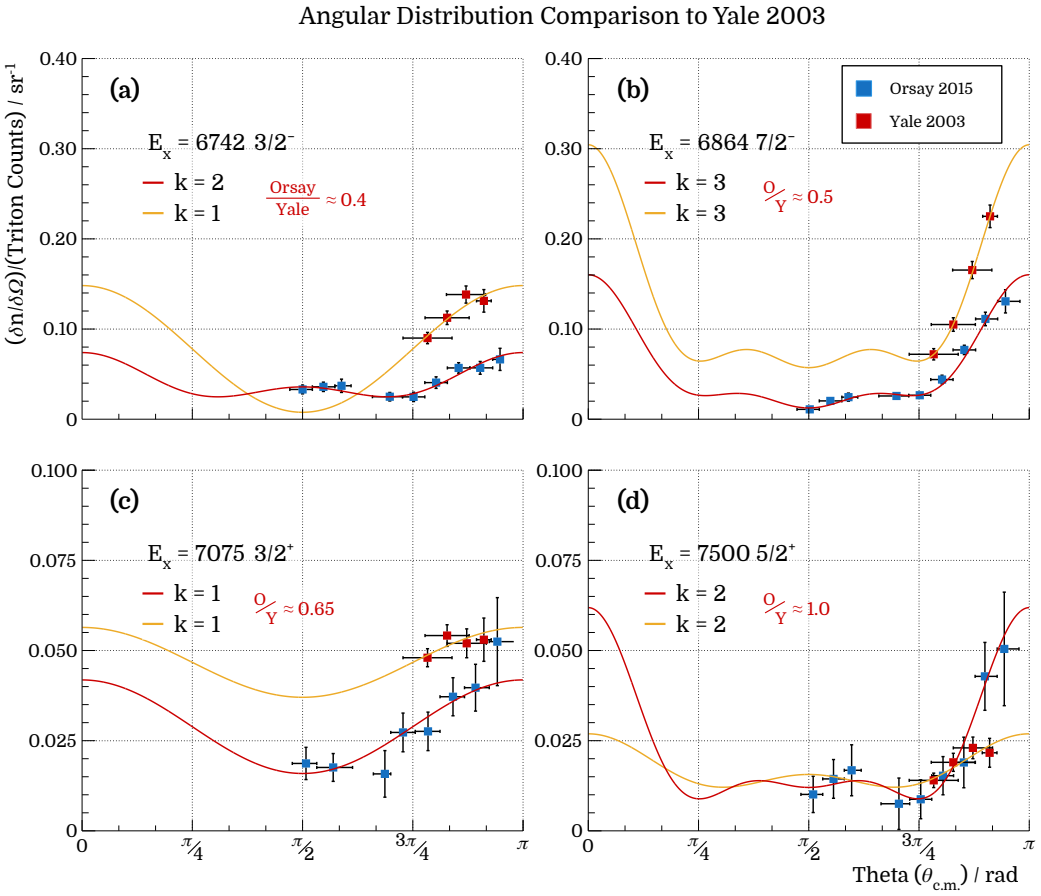

Figure 4.26: Angular distribution comparisons for α-decay from 6742, 6864, 7076 and 7500 keV states in ^{19}Ne (panels **(a)** - **(d)** respectively) between Orsay (2015) and Yale (2003). Yale data have been taken from ref. [82] where functions fit to the data have been approximated to those in the literature for guiding purposes only.

Given the number of previous measurements, as well as predictions of the states' partial widths from mirror state assignments, the discrepancy is most likely to be a fault in either the data measurement itself or its subsequent analysis. Discussion as to the cause of the discrepancy has been provided in Chapter 6.

Chapter 5

Reaction Matrix Analysis

An analysis of the ^{18}F(p,α)^{15}O reaction was conducted using the reaction matrix (R-Matrix) mathematical formalism, outlined in section 2.3, in order to understand the implications for the reaction rate at novae temperatures from the experiment discussed in the last two chapters. The results from this work were combined with new parameters and states from recent publications yet to be included in such a calculation[1] to provide the most comprehensive view of the currently predicted rate. The parameters for all states in ^{19}Ne between 6 to 8 MeV were investigated[2], including their current uncertainties, to establish the known limits on the cross section and identify the principal components for its remaining ambiguity.

5.1 AZURE2

The multi-channel, multi-level R-matrix calculations were performed using the AZURE2 [84] code designed specifically to model low energy nuclear reactions of charged particles. Whilst AZURE2 can make use of the phenomenological nature of R-Matrix (resonance parameters can be extracted from reaction measurement inputs over a range of channels, energies and angles) its value to this work lay in its ability to calculate cross sections from resonance parameters and extrapolate their contribution to the energy region of interest.

[1] Further details are given in Table 1.2.
[2] The impact of states outside this range were found to be negligible.

5.1.1 Input Parameters

AZURE2 requires the following inputs in order to parameterise the compound nucleus and compute the cross sections.

1) **Entrance Channel Particle Pair**
   - Ground state spin-parity
   - Separation energy

   Exit Channel Particle Pair
   - Ground state spin-parity
   - Separation energy

   Channel Radius

2) **Compound Nucleus State**
   - Excitation energy (E_x)
   - Spin-parity (J^π)

3) **Channel Spin**
   - Partial width ($\Gamma_{a,p}$)
   - Interference ($^+/_-$)

1) The particle pairs were selected for the reaction of interest (^{18}F+p and ^{15}O+α) and the channel radius was calculated to be 5 fm (an average of the entrance and exit channel found using eq. 2.26)[1].

2) Nuclear states of the ^{19}Ne compound nucleus (constructed from the particle pairs) are then entered with their excitation energy and spin-parity.

3) AZURE2 uses the states' J^π and ground state spins of the particle pairs to calculate all available channels (with spin s and orbital momentum l[2]). A partial width must be entered for each channel where the interference term of the channel is indicated by a change of sign. Neighbouring same-spin states with the same interference sign produce a constructive interference, whilst differing signs produce a destructive interference.

[1] Previous calculations have shown that cross sections can be sensitive to the chosen channel radius and, as it is only a tool of the formalism and has no exact value, it must be included in uncertainty estimates. After the final calculation from this work was performed, the channel radius was varied from 4-6 fm and no such sensitivity was found.

[2] For γ-decays, the channels are listed by multipolarity.

Given the low energy of the reaction, the assumption was made that all decays occurred through the lowest l-value channel and the partial width for all other channels was left at 0 eV. Bound levels can also be passed to AZURE2, however, as inputting a partial width for the channel would have no physical meaning, AZURE2 uses asymptotic normalisation coefficients (ANC) to define the state's contribution to the cross section above threshold (see section 2.3.1). The ANCs can be viewed as the single proton tail amplitude of the ^{19}Ne wave function when the ^{18}F core and proton are separated by a large distance (in relation to the strong force interaction radius).

5.1.2 Output

Once the reaction has been constructed using the inputs listed above, AZURE2 outputs cross sections and S-factors calculated over a specified energy range to a data file read by the ROOT analysis framework used previously. For the majority of the analysis, this was the only output used where S-factors produced by different sets of parameter inputs were compared to one another. AZURE2 also has the ability to calculate reaction rates (to be input into ROOT) directly from its computed cross sections using eq. 2.12 shown in Chapter 2.

As discussed in section 6.3.2, some additional modifications to the calculation were required in order to match or predict experimental data. In most experiments, the true cross section is never measured directly. The observed yield is unavoidably affected by the finite energy resolution of the beam and the finite thickness of the target. If the cross section changes slowly in energy, compared to the energy resolution and the target thickness, then the shape of the yield approaches the shape of the true cross section. The cross section distortion can be simulated by AZURE2 by convoluting the cross section with the Gaussian function,

$$g(E - E_0) = \frac{1}{\sqrt{2\pi}}\sigma_b \exp\left[-\frac{(E - E_0)}{2\sigma_b^2}\right] \tag{5.1}$$

where σ_b is the energy width of the experimental beam.

5.2 Parameter Variation

The calculations used an initial set of parameters taken from Table II in ref. [66] to confirm agreement with previously published work and to provide a starting set of parameters on which to build. From the list of energy levels in Table 1.2 each resonance was investigated for its contribution to the S-factor and those with a negligible effect (usually those of high spin) were omitted. Due to some states response being affected by the presence of other states or by their parameter uncertainties, this was an iterative process. Those that remained are listed in Table 5.1 and their individual contributions to the reaction S-factor shown in Fig. 5.1.

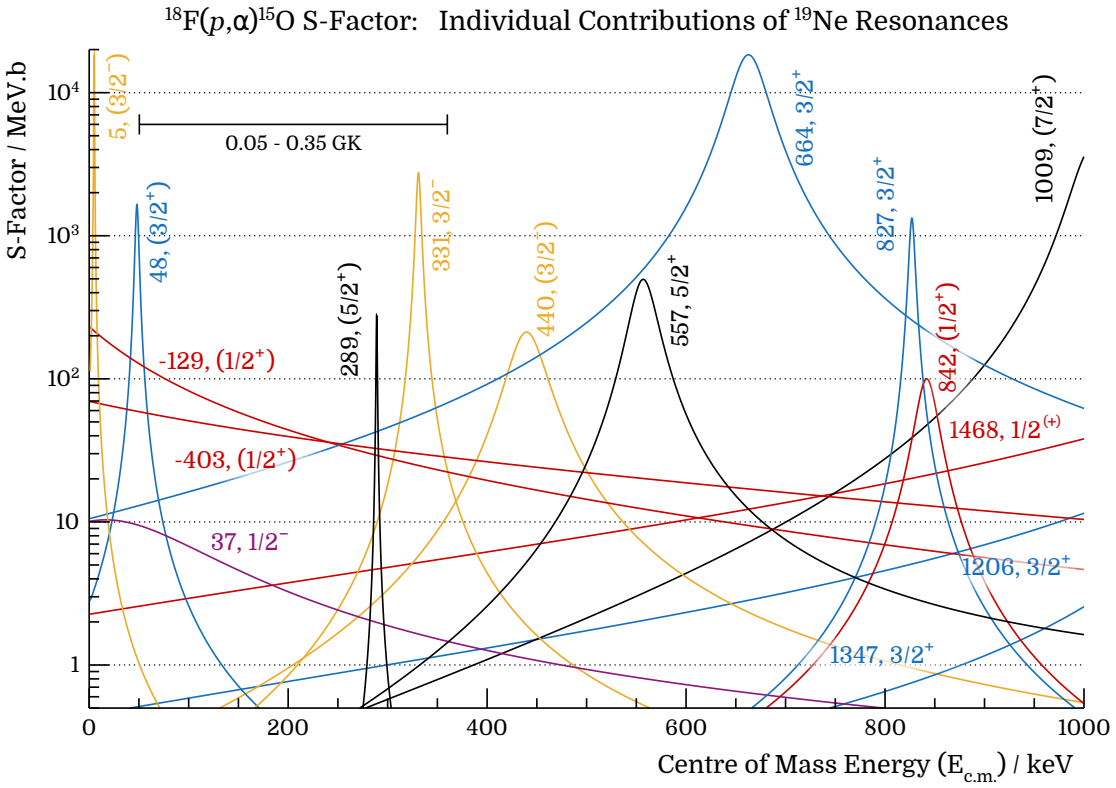

Figure 5.1: S-factor calculated for each state in Table 5.1 when set as the only input. The contribution of each state, grouped in colour by J^{π}, is shown explicitly. The novae temperature range has been indicated above.

Further calculations were then performed, outlined in the sections below, to investigate the S-factor's sensitivity to each parameter uncertainty and to highlight states of particular interest for further experimental study.

$\mathbf{E}_x$ / MeV	$\mathbf{E}_{\text{c.m.}}$ / keV	$\mathbf{J}^\pi$	$\mathbf{\Gamma}_\alpha$ / keV	$\mathbf{\Gamma}_p$ / keV
6.008(20)[a]	-403	$(\frac{1}{2}^+)$	124(25)	ANC = 4[b] $\text{fm}^{-\frac{1}{2}}$
6.282(2)[c]	-129	$\frac{1}{2}^+, \frac{9}{2}^+, \frac{11}{2}^+$	11.624, ...	ANC = 73.069[d] $\text{fm}^{-\frac{1}{2}}$, ...
6.295(2)[c]	-116			
6.411	0	$^{18}\text{F} + p$		
6.416(3)	5	$\frac{3}{2}^-, \frac{5}{2}^+$	0.5(5), 0.126(126)	$[47(47), 1.2(12)] \times 10^{-51}$
6.437(9)	26	$\frac{1}{2}^-$	220(20)	$1.1(11) \times 10^{-20}$
6.459(3)	48	$\frac{3}{2}^+, \frac{5}{2}^-$	4(4), 5.5(55)	$[2.35(4), 8.4(84)] \times 10^{-14}$
6.700(3)	289	$(\frac{5}{2}^+)$	1.2(10)	$1.2(12) \times 10^{-5}$
6.742(2)	331	$\frac{3}{2}^-$	5.2(37)	$2.22(69) \times 10^{-3}$
6.851(4)	440	$(\frac{3}{2}^-)$	40(20)[e]	$9.7(97) \times 10^{-3}$
6.968(19)	557	$(\frac{5}{2}^+)$	29(25)	$4.7(47) \times 10^{-2}$
7.076(2)	665	$\frac{3}{2}^+$	23.8(12)	15.2(1)
7.238(6)	827	$\frac{3}{2}^+$	6.0(52)	0.35(35)
7.253(10)	842	$(\frac{1}{2}^+)$	23(20)	0.2(2)
7.420(14)	1009	$\frac{7}{2}^+$	71(11)	27(4)
7.616(5)	1206	$\frac{3}{2}^+$	43(15)	2(1)
7.758(6)	1347	$\frac{3}{2}^+$	5(2)	42(10)
7.879(26)	1468	$\frac{1}{2}^{(+)}$	130(108)	228(50)

[a] New state observed in this work. [b] Taken from ref. [60].
[c] Input as single state with energy ambiguity investigated. [d] Taken from ref. [58].
[e] Measured Γ_t from ref. [57] taken as Γ_α.

Table 5.1: Table of ^{19}Ne states, used as input parameters for AZURE2, that contribute the most to the $^{18}\text{F}(p,\alpha)$ reaction rate in novae. The sensitivity of the rate to the uncertainties shown in the table are explored in the following sections.

5.2.1 Interference ($^+/_-$) Sensitivity

All previous studies of the reaction rate have pointed towards interference between similar spin states being the primary cause for uncertainty in the novae energy region. It was important, therefore, to find the minimum and maximum terms between all relevant spin parity states so further parameter variation could be observed at each extreme. Interference from states of spin 5/2 and above were quickly found to have no impact on the S-Factor and therefore all terms have been discounted from further analysis. Below are the possible interferences from Table 5.1.

			Max	Min[1]
•	$\mathbf{1/2^+}$ 4 states	8 sequences	++−−	+−+−
•	$\mathbf{3/2^+}$ 5 states	16 sequences	−++++	−−+++
•	$\mathbf{3/2^-}$ 3 states	4 sequences	−++	++−

[1]Maximum and minimum terms as applied to the novae temperature range only.

Fig. 5.2 shows the primary uncertainty bands for each J^{π}. It should be noted that a $1/2^{-}$ state seen in ^{19}F has yet to be observed at its predicted energy of 6939 keV ($E_{c.m.}$ = 528 keV) in ^{19}Ne. For that reason the state has not been included in the R-matrix calculations, however the interference between the 26, 528 and 1233 (as $1/2^{-}$) is not negligible (see Appendix C) and must be considered if the resonance were to be discovered.

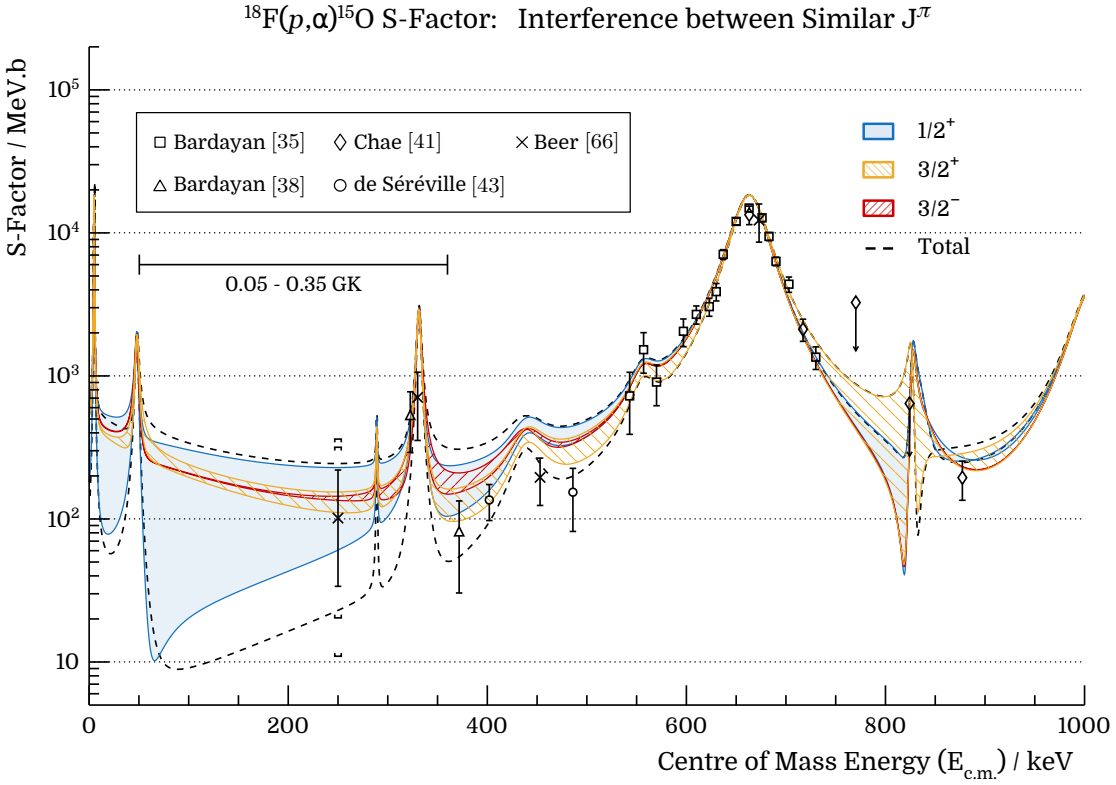

Figure 5.2: S-factor uncertainty from spin parity interference. Each J^{π} was investigated separately and those not being varied were fixed to positive terms. Comparison to R-matrix calculations performed by Bardayan *et al.* (Fig. 1.10) shows the additional uncertainty that arises from the presence of the subthreshold $1/2^{+}$ resonance seen in this work (Fig. 4.16).

The minimum and maximum terms from the $1/2^{+}$, $3/2^{+}$ and $3/2^{-}$ spin-parities were applied simultaneously to find the total potential range in S-factor also shown in Fig. 5.2 as a dashed line. Interference terms from each state cannot be measured experimentally and must be analysed qualitatively by comparing to direct reaction measurements. Comparison to previously published data [35, 38, 41, 43, 66], particularly at $E_{c.m.}$ = ∼400 keV, immediately excludes several of the more constructive interference terms and as such have been discounted from the remaining analysis. The remaining terms providing the maximum and minimum S-factor curves allowed by the data are as follows,

Max:	$1/2^+$	$++-+$	**Min:**	$1/2^+$	$+-+-$
	$3/2^+$	$--+++$		$3/2^+$	$--+++$
	$3/2^-$	$++-$		$3/2^-$	$++-$

and have been marked in the remaining figures as a dashed line.

5.2.2 Energy (E_x) Sensitivity

For the majority of narrow states, their relatively small uncertainty in excitation energy, <10 keV, proved inconsequential to a change in S-factor. The two broad $1/2^+$ resonances, $-401(20)$ and 1468(26) keV, additionally, did not meaningfully increase or decrease the S-factor despite their larger uncertainty.

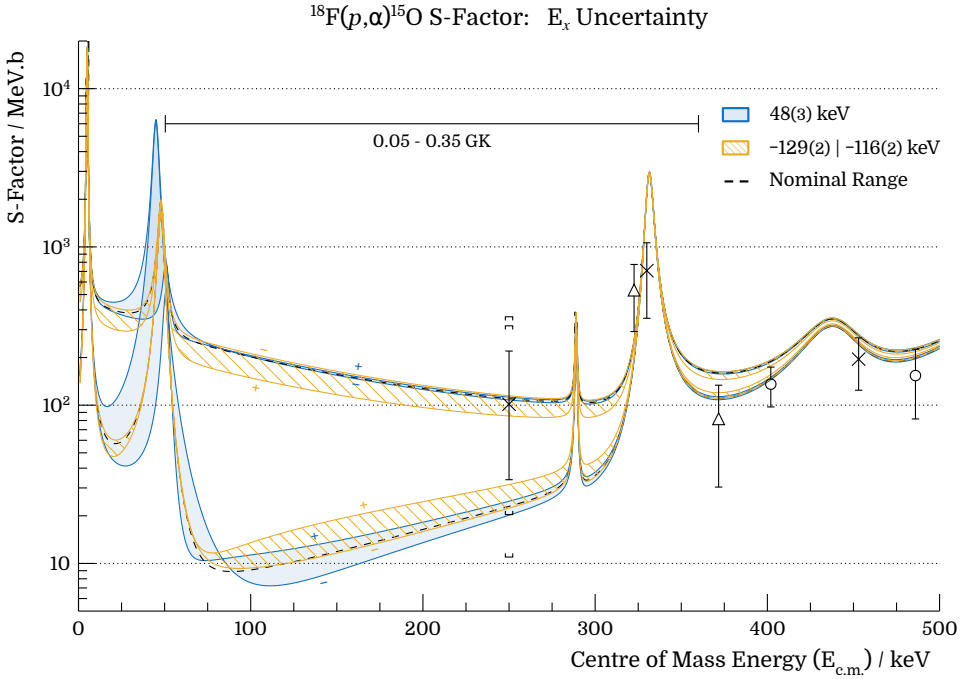

Figure 5.3: Change in maximum and minimum S-factor from uncertainty in resonance energy.

48 keV A significant change was caused by the 48 keV resonance shown in Fig. 5.3 where the destructive interference from the $3/2^+$ resonance is highly sensitive to the small (± 3 keV) shifts in the pole energy.

-129 keV The potential of a subthreshold doublet [57], whilst beneficial for explaining its spin ambiguity, does create a large energy uncertainty for the position of the potential $1/2^+$ state. Also plotted in Fig. 5.3, it can be seen that the energy range of $-129 - 2$ keV to $-116 + 2$ keV translates into a significant variation in the S-factor.

The changes made to the pole positions of the states must be viewed with caution, however, as most partial width assignments for the states in ^{19}Ne have been taken from their mirror analogues. Strictly speaking, therefore, changes to the energy cannot be made without changes to the width. The calculations for the subthreshold ANCs are particularly sensitive to the resonance energy.

5.2.3 Width (Γ) Sensitivity

Γ_α After investigating each resonance, the only sensitivity found to the alpha-particle partial width was from the two broad $1/2^+$ resonances. Only when the widths from both were set to their terminus did the S-factor vary appreciably within the novae temperature range (see Fig. 5.4).

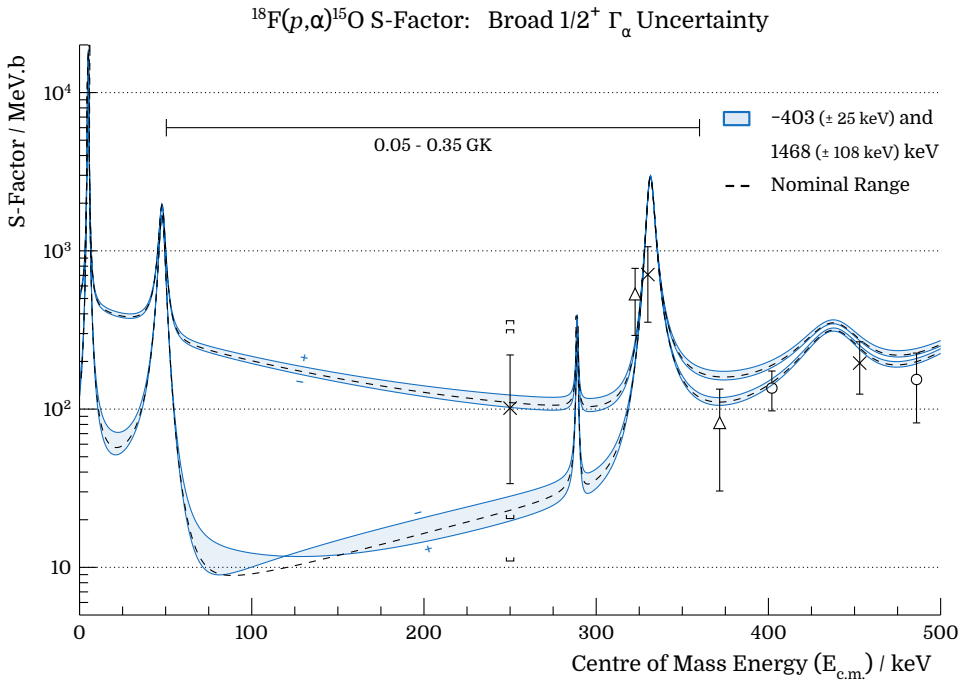

Figure 5.4: Change in maximum and minimum S-factor from uncertainty in α-particle partial width.

Γ_p From eq. 2.24 it can be shown that a resonance's strength for a particular reaction is more dependent on the channel with the narrower partial width. It was therefore expected that the S-factor uncertainty would be increased significantly due to unmeasured Γ_p in the ^{19}Ne resonances. Widths taken from mirror states were varied by an order of magnitude in each direction whilst measured widths were limited to their uncertainty. Large fluctuations in the S-factor were observed for the majority of resonances, as expected

from their narrower proton widths, but were localised to the resonances energy region. The Γ_p uncertainties from the 26 and 48 keV were the only resonances to affect the rate in the inter-resonance region within the temperature range of interest (see Fig. 5.5).

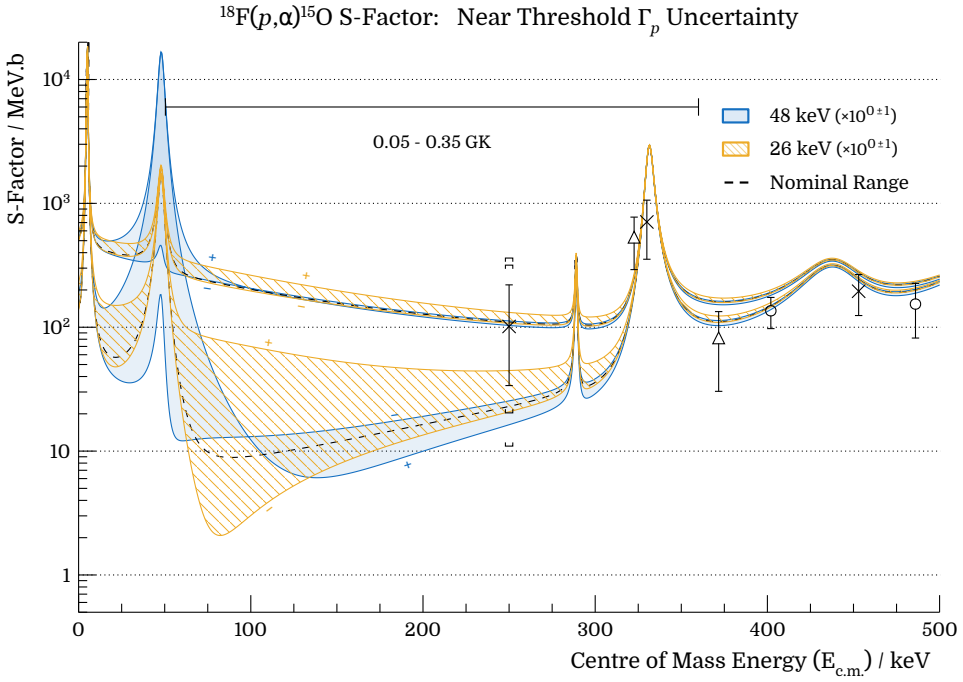

Figure 5.5: Change in maximum and minimum S-factor from uncertainty in p partial width.

440, 557 keV Because of the importance of the data to exclude interference patterns that are not in agreement, the two new states providing structure to the 400 to 600 keV region

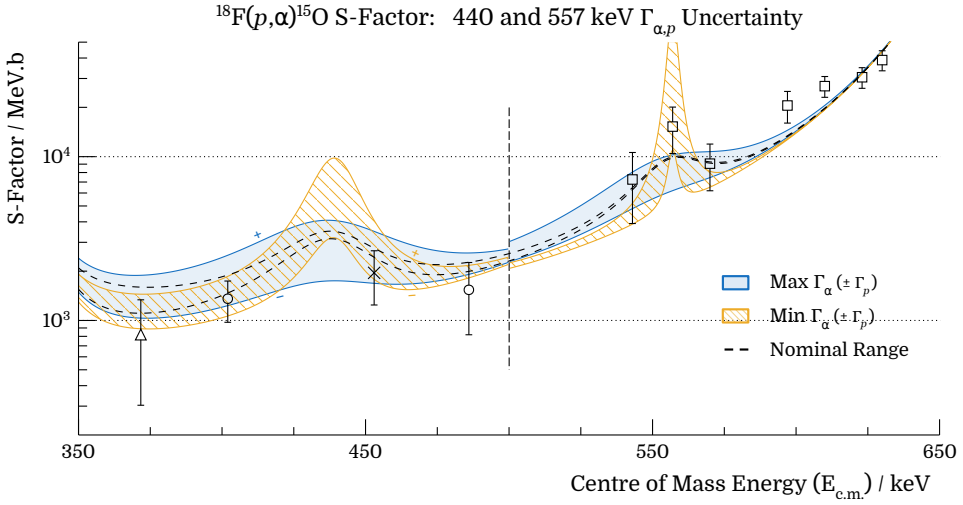

Figure 5.6: Change in S-factor from 440, 557 keV partial width uncertainty. The plots show a variation in proton width when $\Gamma_\alpha^{\mathrm{Max}}$ (blue) and $\Gamma_\alpha^{\mathrm{Min}}$ (yellow). The calculations for each resonance have been plotted separately.

were scrutinised more closely. Fig. 5.6 shows the full Γ_α uncertainty from Table 5.1 and a Γ_p uncertainty of a factor of 2. Whilst providing scope to better describe the data, crucially no interference terms can be excluded or new terms included within the current width constraint.

ANCs Finally, the S-factor sensitivity to the subthreshold resonances ANC values were considered. Whilst a more rigorous analysis of the ANC uncertainties is advised, the calculations performed in the current work (shown in Fig. 5.7) demonstrates that the S-factor is highly sensitive to small changes in the coefficients and, therefore, also in the reduced widths and single particle wave function calculations. As neither ANC value has been published with uncertainties, the ANC for -403 keV initially taken from ref. [60] was varied by ± 1 fm$^{-1/2}$ and the -122 keV ANC (initially taken from ref. [58]) was varied by ± 5 fm$^{-1/2}$.

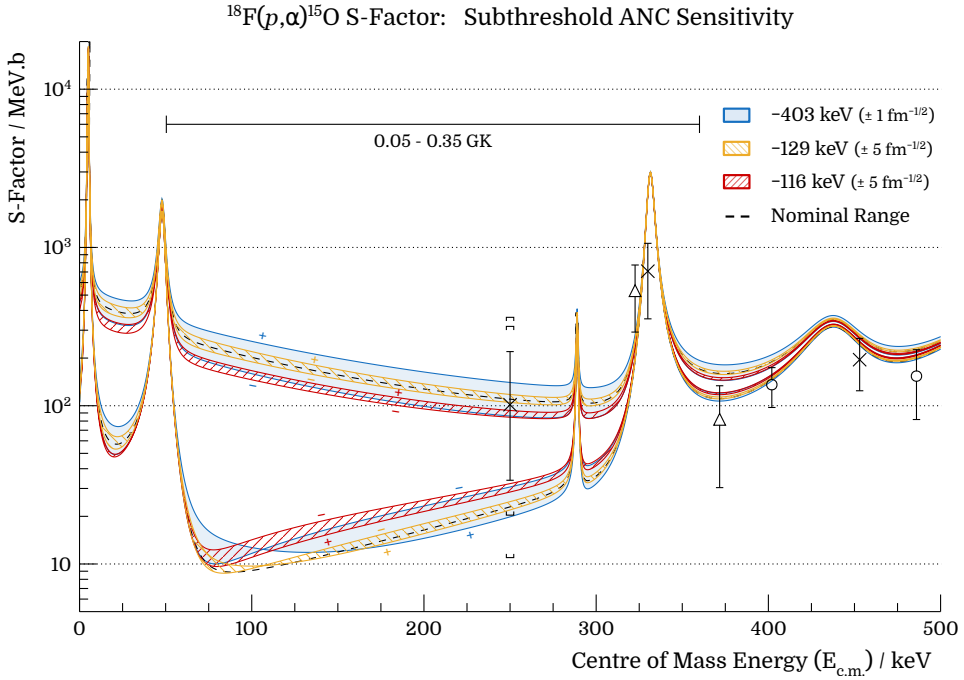

Figure 5.7: Change in maximum and minimum S-factor from adjustments in subthreshold asymptotic normalisation coefficient.

5.2.4 Spin-Parity (J^π) Sensitivity

Resonances at -129, 5 and 48 keV all have multiple possible spin-parities and the presence of the broad $1/2^+$ subthreshold currently remains tenuous. The last investigation made into the ^{18}F(p,α) cross section focused on its sensitivity to the spin parity assignments

of these states. The changes to the S-factor uncertainty from the −129 and 48 keV J^π alterations have been plotted in Fig. 5.8. The J^π of the 5 keV resonance was found to have no bearing on the reaction probability for novae temperatures and has not been included. Changes to the spin-parity of a state modified the interference sequences, therefore, the terms were reanalysed to find the new maximum and minimum contributions.

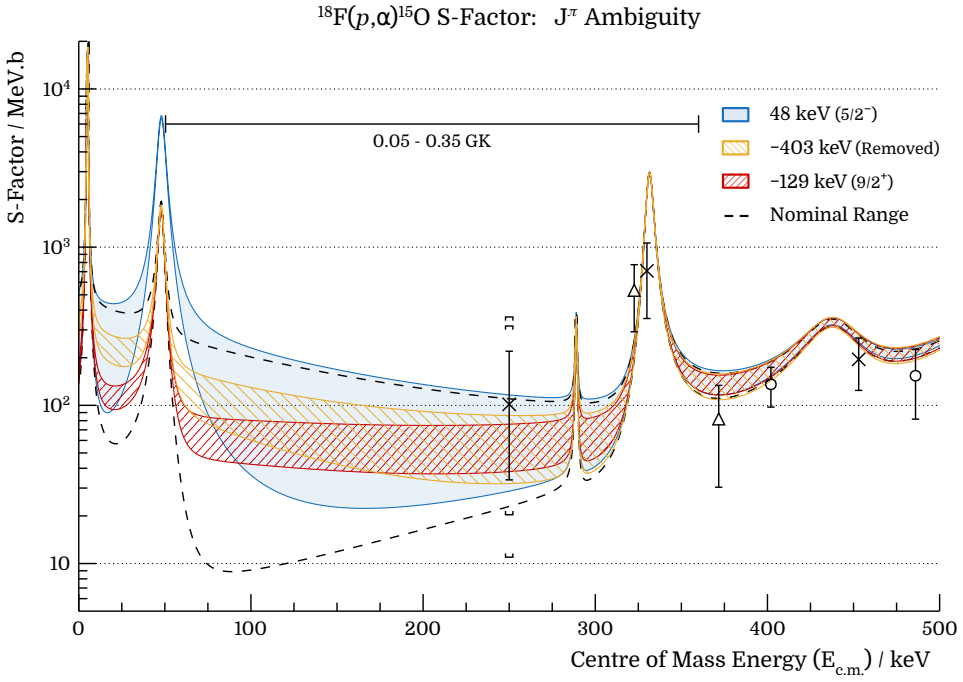

Figure 5.8: S-factor uncertainty from a change in J^π. Removing a $1/2^+$ or $3/2^+$ interference term constrains the S-factor significantly.

Fig. 5.8 also shows the effect when the −403 keV resonance is either higher in spin or is removed entirely (both produce the same result). The results from the J^π change show the dominating effect from the $1/2^+$ interference whereas the S-factor uncertainty is constrained considerably if just one of the $1/2^+$ subthreshold states is removed from the sequence. The change to the above threshold resonance is caused primarily from the new Γ_p and Γ_α widths that accompany the new J^π. Though not shown, the constraint from each spin-parity change could potentially be compounded.

$3/2^+$ Location

Given the ambiguity that remains with the position of the $3/2^+$ states (known to be present from the mirror nucleus), the $3/2^+$ interference was investigated further with the following candidate resonances used to either replace, or include with, the 48 keV resonance.

5 keV (Γ_α = 270 eV, Γ_p =2.2E-34 eV) The $3/2^+$ assignment was not included in Table 5.1, however this remains one of the few possible mirror states for the ^{19}F 6497 keV state.

−129 keV (Γ_α = 440 eV, ANC = 51.67 fm$^{-\frac{1}{2}}$) Previously measured as $3/2^+$ [53], this assignment has not been completely ruled out. Though unlikely to be the second state in the doublet, it was only input in place of the previous $1/2^+$ assignment.

−282 keV (Γ_α =0.7 eV, γ_p = 143 eV) The first of two subthreshold states that could be spin $3/2^+$, suggested by [52], if no above threshold resonances are available. Given the un-calculated ANC, this also remained a variable parameter in the calculations.

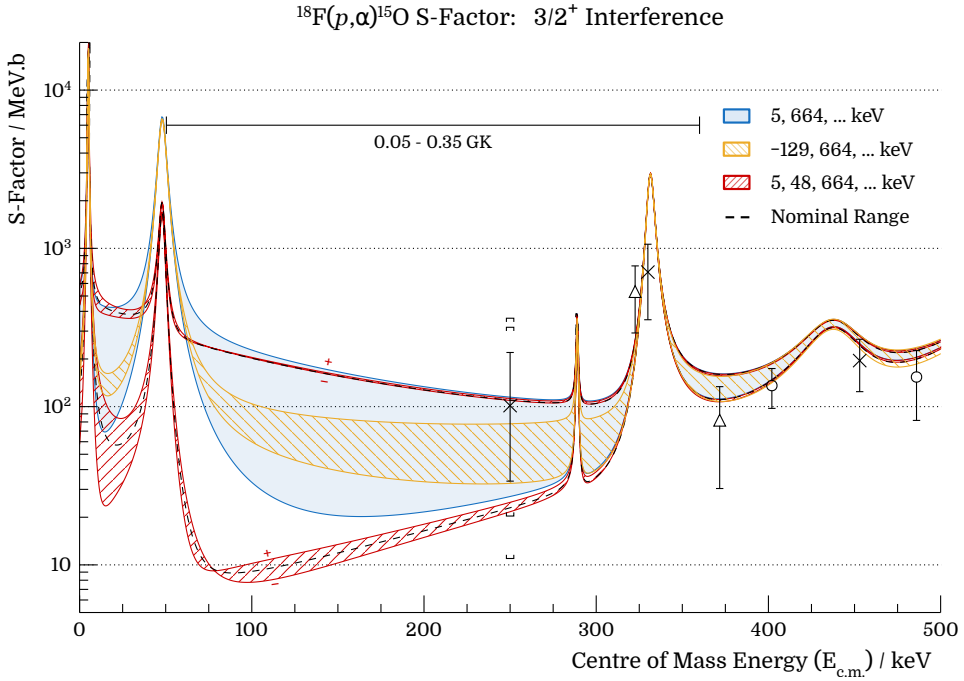

Figure 5.9: S-factor uncertainty for new $3/2^+$ interference sequences. The addition of the 5 keV resonance slightly increases the variation in S-factor whilst replacing the 48 keV with any other possible $3/2^+$ resonance almost entirely removes the $3/2^+$ interference effects from the nova temperature region.

Fig. 5.9 shows some of the results from the analysis. Only the 5 keV resonance provided further interference terms that increased the uncertainty noticeably (the figure shows the difference between adding as constructive or destructive interference). The curves showing the effect of replacing the 48 keV with the 5 keV are almost in agreement with Fig. 5.8 where the 48 keV was simply changed to its possible assignment of $5/2^-$ i.e. the $3/2^+$ interference is far less consequential if the 48 keV is not included in the sequence.

The change from the −129 keV used in replacement of the 48 keV is dominated by the removal of the $1/2^+$ interference term and the $3/2^+$ interference in the remaining uncertainty is negligible. The subthreshold state (not shown) produced no interference with the

665 keV $3/2^+$ resonance (when used to replace the 48 keV), nor with the 48 keV $3/2^+$ when used in conjunction despite the further variation of its Γ and E_x parameters.

5.3 $^{18}F(p,\alpha)^{15}O$ Reaction Rate

Calculations of the $^{18}F(p,\alpha)$ reaction rate at novae temperatures were performed by numerical integration of eq. 2.12 by AZURE2. Fig. 5.10 shows a comparison of upper and lower reaction rate limits between the uncertainty from

- The nominal minimum and maximum interference terms (section 5.2.1)
- The subthreshold $1/2^+$ E_x
- The 26 keV Γ_p
- The 48 keV Γ_p

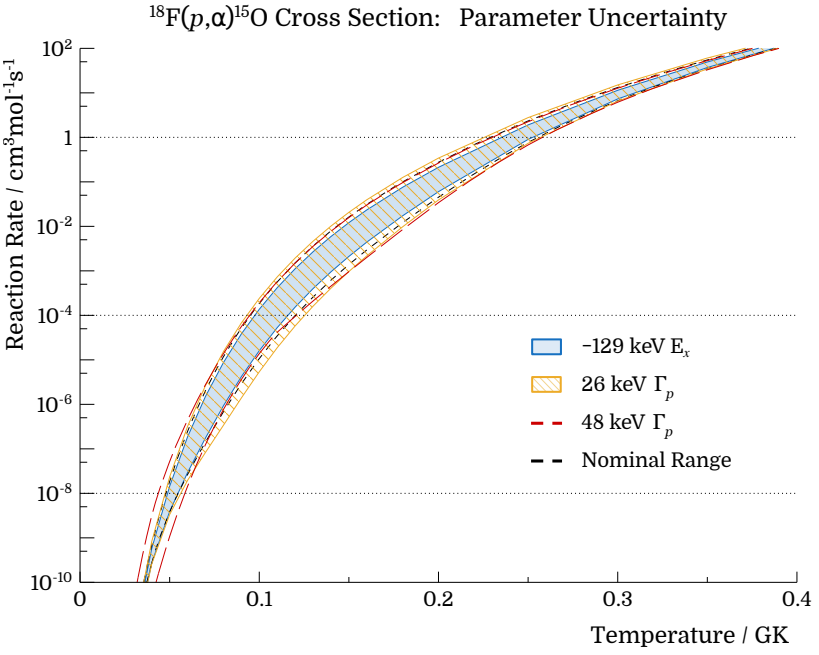

Figure 5.10: Reaction rate for $^{18}F(p,\alpha)$ showing the proton width variation in the 26 and 48 keV states that increase uncertainty, and the change in energy for the -129 keV state (to -116 keV) that decreases uncertainty.

and Fig. 5.11 shows a comparison between the uncertainty from

- The nominal minimum and maximum interference terms
- The 48 keV spin change from $J^\pi = 3/2^+$ to $J^\pi = 5/2^-$
- The -129 keV spin change from $J^\pi = 1/2^+$ to $J^\pi = 9/2^+$
- The removal of the -403 keV resonance

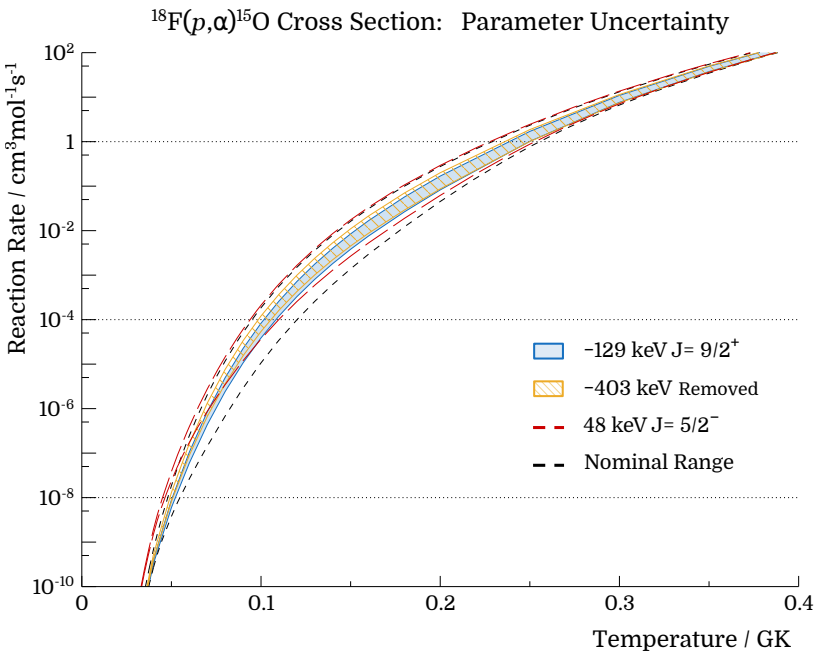

Figure 5.11: Reaction rate for ^{18}F(p,α) showing the spin-parity changes that decrease uncertainty.

Whilst the S-factor was found to be sensitive to other parameter inputs, the change to the rate was deemed either too small, such as the addition of the 5 keV resonance to the $3/2^+$ interference (Fig. 5.9), or too improbable, such as the extreme alpha-particle widths of both broad $1/2^+$ resonances (Fig. 5.4).

Fig. 5.10 and 5.11 show that the principal uncertainty in the rate lies between 0.1 and 0.3 GK while the extreme ends of the novae temperature range are relatively constrained due to the presence of the 48 and 331 keV resonances. Only the uncertainty in the 48 keV proton width creates a larger disparity between the upper and lower rate limits below 0.075 GK. The rate across the entire nova temperature window is constrained significantly when the -129 keV resonance is assigned to $J^\pi = 9/2^+$ (as was found in this work), the -403 keV is assigned a higher spin (or removed), or the 48 keV is given its second J^π assignment of $5/2^-$. Given their influence on the $1/2^+$ and $3/2^+$ interference and the interference's dominating effect on the S-factor uncertainty (discussed in the previous section), this is not surprising.

The nominal upper and lower rates calculated from the parameters as quoted in Table 5.1 and used for comparison throughout this chapter were also analysed against the reaction rate values calculated by Iliadis *et al.* in the most recent compilation paper [85] (also used

in the STARLIB reaction rate library [86]). The two rates differ in their calculation in a number of areas leading to a significant contrast in the reaction rate across the entire nova temperature as displayed in Fig. 5.12. Below are listed some comments on the STARLIB reaction rate made by Iliadis *et al.*, followed by distinctions compared to this work.

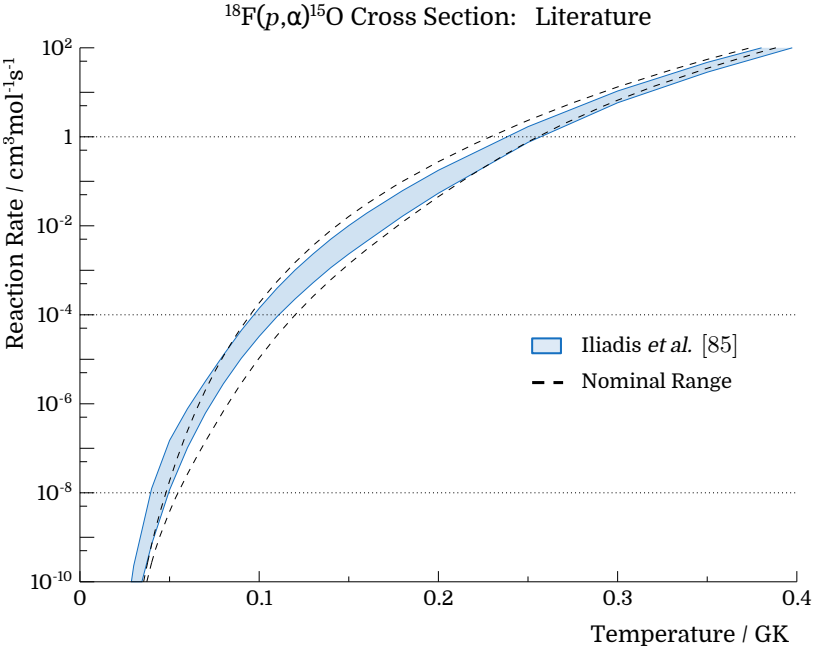

Figure 5.12: Reaction rate for ^{18}F(p,α) from this work plotted against the currently accepted reaction rate from Iliadis *et al.* [85].

Most resonance energies are taken from Utku *et al.* [36] The energies used in this work have been updated from Neseraja *et al.* [50] depending on the accuracy of the measurement (see Table 1.2). The differences in most energies are inconsequential to the rate, however, the observation of a triplet above the p-threshold caused the 8 and 38 keV resonances to be re-assigned energies of 5 and 48 keV respectively and thus required a re-calculation of their partial widths.

8 keV resonance was assumed to be $J^\pi = 3/2^+$ The 8 keV (now measured to be 5 keV) has been re-assigned to $J^\pi = 3/2^-$ and used as such in this work. The reassignment removed its interference with other $3/2^+$ resonances and is partially the reason for the more constrained reaction rate below 0.05 GK shown in the figure.

Unobserved levels in ^{19}Ne compared to ^{19}F were ignored. Several resonances have now been observed since the publication of ref. [85]. Those of which are used in the calculations from this work include the $3/2^+$ resonance at 1347 keV, the $5/2^+$ 557 keV and the $3/2^-$ at 440 keV. The presence of the latter two have prevented interference terms from being excluded due to the now constricted S-factors over the direct measurement data (see Fig. 5.6).

Resonances above 900 keV are not included. This means that some $3/2^+$ resonances, known from this work to have noticeable interference effects across the energy range of interest, were not accounted for. Crucially, however, this also implies that the broad $1/2^+$ resonance at 1468 keV was not included nor, given its very recent observation (and confirmation in this work), was the subthreshold $1/2^+$ at -403 keV and its subsequent interference. These states have been included in this work, however, and in turn have increased the reaction rate uncertainty.

5.3.1 ^{18}F as a Nova Observable

The ^{18}F(p,α)^{15}O reaction rate is directly proportional to the abundance of ^{18}F calculated from novae reaction networks [37, 38, 59]. An increase to the reaction rate at novae temperatures would lead to the destruction of a greater number of ^{18}F nuclei and thus reduce the expected ^{18}F abundance in a nova outburst. Alternatively, a reduced rate would mean more of the ^{18}F was retained to then decay via β^+ emission, generating a more intense 511 keV gamma source.

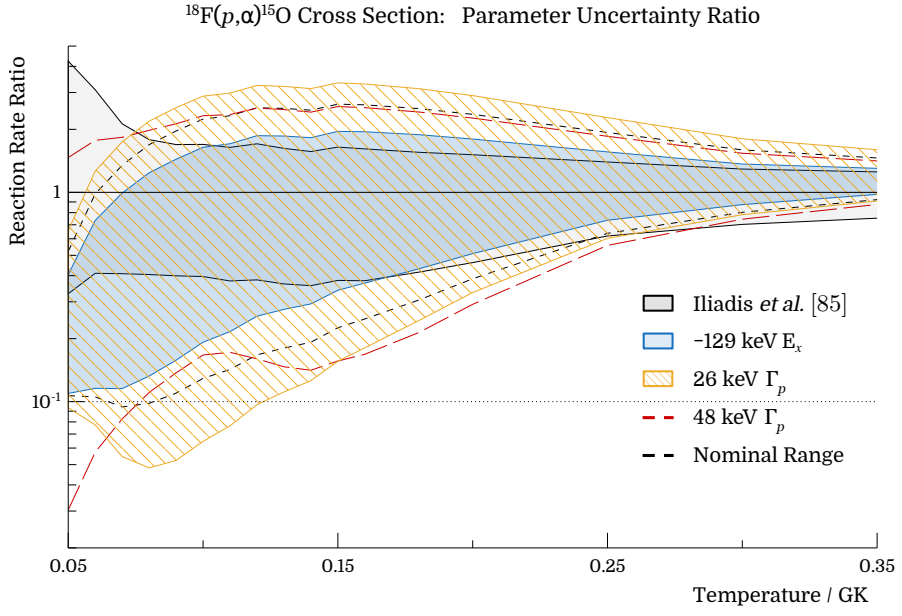

Figure 5.13: Ratio of reaction rate plots from Fig. 5.10 against the rates from STARLIB (calculated by Iliadis *et al.* [85]).

The upper and lower rate limits from Fig. 5.10 and 5.11 have been normalised against the nominal ^{18}F(p,α) STARLIB reaction rate and plotted in Fig. 5.13 and 5.14 respectively. The two figures show the implications of the key results from this work more explicitly, both in comparison with the different parameter inputs from section 5.2 and with the currently

accepted rates in the literature. As discussed, the additional uncertainty in comparison to the literature originates primarily from the $1/2^+$ interference, and the reduced rate at lower temperatures originates from the changes to the 5 and 48 keV resonance parameters.

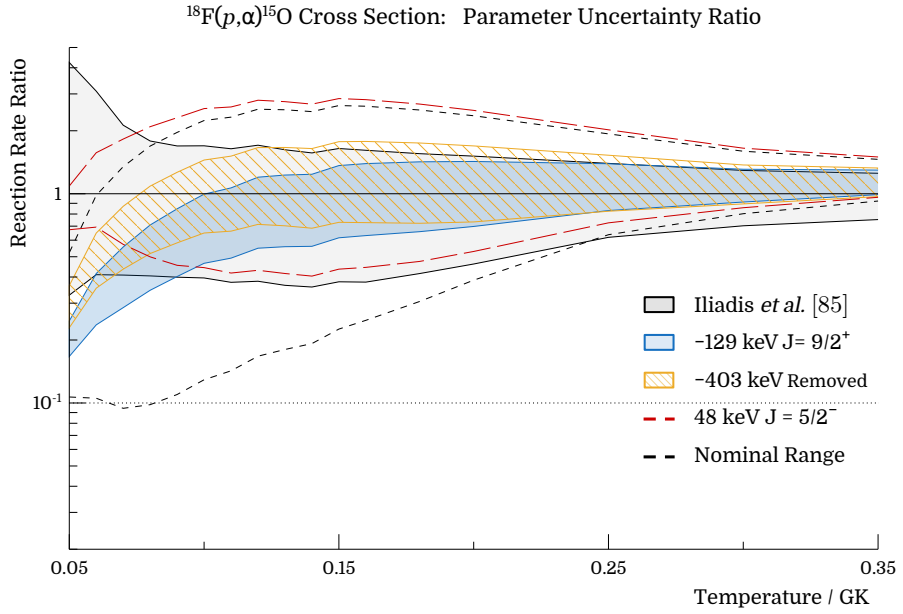

Figure 5.14: Ratio of reaction rate plots from Fig. 5.11 against the rates from STARLIB (calculated by Iliadis *et al.* [85]).

NuGRID

The nominal minimum and maximum reaction rates taken from this work have been used as part of a reaction network, programmed to follow the temperature and density profiles of a novae outburst. The nova model was constructed by the NuGrid collaboration [87] using published reaction rates as the nuclear physics input and temperature and density profiles (trajectories) calculated from tracer particles in hydrodynamic simulations to provide the astrophysical environment. The abundances of each isotope are then calculated based on the temperature and density of the nova for each time step. The reaction rates from this work[1] were input into three different trajectories based on novae simulations performed by Denissenkov *et al.* [89] and the final ^{18}F abundances from each are presented in Table 5.2.

[1]The reaction rates required parameterisation into the REACLIB format using eq. 1 from ref. [88].

Nova	Mass / $M_\odot$	T / GK		$t-T_{Max}$ / s	^{18}F / Mass Fraction		
		Initial	Max		Min	Max	Min/Max
CO[a]	1.15	0.012	0.236	2850	2.47×10^{-4}	2.81×10^{-5}	8.82
ONe[b]	1.15	0.012	0.263	3600	3.92×10^{-7}	5.40×10^{-8}	7.30
ONe[c]	1.3	0.012	0.355	900	3.36×10^{-6}	6.86×10^{-7}	4.90

[a] Trajectory from Fig. 8 in ref. [89]
[b] Trajectory from Fig. 7 in ref. [89]
[c] Trajectory from Fig. 13 in ref. [89]

Table 5.2: ^{18}F abundance estimates from post processing simulations using three different nova trajectories. The accretion rate for all three is 2×10^{-10} $M_\odot yr^{-1}$.

SHIVA

As a second source for abundance calculations, the reaction rates from this work were also passed to Professor Jordie José[1] for input into a one-dimensional hydrodynamic simulation performed using the SHIVA code [12]. A model of a 1.25 $M_\odot$ ONe white dwarf accreting H-rich material from its stellar companion at a rate of 2×10^{-10} $M_\odot yr^{-1}$ was computed using three sets of $^{18}F(p,\alpha)^{15}O$ reaction rates from this work. The first is the 'nominal' rate where resonance contributions are calculated using their quoted values in Table 5.1. The second set has assumed the -129 keV resonance to be of spin $J^\pi = 9/2^+$ as was concluded from this work (see Fig. 4.19), i.e. a change to the $1/2^+$ interference. The final set has assumed the 48 keV resonance to be of spin $J^\pi = 5/2^-$, i.e. a change to the $3/2^+$ interference. Table 5.3 shows the differences to the ejected ^{18}F mass fractions 1 hour after peak temperature was reached in the nova model. Note that a maximum cross section corresponds to a minimum ^{18}F abundance as the reaction rate is destructive in nature.

Set	^{18}F / Mass Fraction			Factor Difference	
	Min	Nom	Max	Min/Max	Nom/STARLIB[a]
1	2.53×10^{-5}	1.55×10^{-5}	5.68×10^{-6}	4.45	1.50
2	1.52×10^{-5}	1.21×10^{-5}	9.04×10^{-6}	1.68	1.18
3	1.87×10^{-5}	1.19×10^{-5}	5.18×10^{-6}	3.61	1.16

[a] STARLIB rate [85] as the input produced a mass fraction of 1.03×10^{-5}.

Table 5.3: ^{18}F abundance estimates from a one-dimensional hydrodynamic simulation of an ONe nova.

[1] Catedràtic de Universidad, Universitat Politècnica de Catalunya, Spain.

Chapter 6

Discussion

6.1 ^{19}Ne Nuclear State Parameters

The levels of ^{19}Ne between 6 and 8 MeV are discussed below with references to their measurement in this work and their influence on the uncertainty of the ^{18}F(p,α)^{15}O astrophysical S-factor.

6.1.1 Resonances Below E_x = 6411

6008 ($1/2^+$) The suggested presence of this subthreshold resonance has increased the uncertainty of the ^{18}F(p,α) reaction rate in novae from a factor of 5 [61] to over an order of magnitude (Fig. 5.13). Evidence of a state at this energy has been confirmed on the basis of an improvement to the fitting minimisation from $\chi^2/\nu = 3.65$ to $\chi^2/\nu = 1.98$ shown in Fig. 4.16. A wide resonance in this energy region cannot be explained by the presence of any other known state in ^{19}Ne and as such is assumed to be the predicted $1/2^+$ resonance from Dufour & Descouvemont [56]. Whilst tentative as a single measurement, the parameter results from the fit (left as free parameters with no upper or lower limits) are in excellent agreement with those from Boulay *et al.* [60] and is in good agreement with the predicted energy position in ref. [56]. A small improvement in the fit ($\chi^2/\nu = 1.49 \rightarrow 1.25$) was also seen in the α-particle coincidence data, although, because of the dominating 6014 keV state, fits to the smaller angular bins could not be made conclusively, removing the possibility of angular distribution measurements. The inclusion of the resonance in

the R-matrix calculations produces a wide range of interference patterns (Fig. 5.2) from the interaction between the 6008, 6282, 7253 and 7879[1] keV states. The ANC (4 $fm^{-\frac{1}{2}}$) describing the resonances contribution to ^{18}F proton capture was calculated in ref. [60] from the single particle wave function and corrected by the spectroscopic factor in ref. [56]. R-matrix analysis showed a small sensitivity in the S-factor to both the ANC (Fig. 5.7) and the α-particle width (Fig. 5.4), though S-factor alterations from energy and width uncertainties were found to be negligible. The substantial contribution the resonance makes to the S-factor uncertainty is best shown in Fig. 5.8 where the resonance has been removed from the AZURE2 parameter inputs. If the resonance is assumed to have $J^\pi \neq 1/2^+$ then it no longer has any contribution to the S-factor producing results similar to its removal.

6014 3/2$^-$ α-particle decays from the 6014 keV state were the first to be above the energy threshold in all six detectors and as such, were the first angular distributions to be comprehensively measured. The high population of the state provided ample statistics, and the $l = 2$ fit to the data (see Fig. 4.18) was made with a high level of confidence. Whilst the spin-parity assignment is physically limited to the possibility of two values, previous measurements of the state suggest $J^\pi = 3/2^-$ in agreement with the data from this work. The mirror assignment suggested in Fig. 1.9 to the 6088 keV state in ^{19}F is contingent on both the equivalent J^π and the expected discrepancy in energy caused by the difference in Coulomb potential. No partial width information is available for either state, however, the state was input into AZURE2 using an upper limit on its total width[2], and was found not to contribute to the S-factor either directly or through interference.

6072 3/2$^+$, 5/2$^-$ | 6097 7/2$^+$, 9/2$^+$ | 6132 3/2$^+$, 5/2$^-$ The three subthreshold resonances situated below the newly suggested doublet could not be resolved effectively from the experimental work in this thesis. This was due to their small energy separation, their large population from the charge exchange reaction (causing intrusion on other states) and the interference from the tail of the 6014 keV state. As such, the spectrum in Fig. 4.15 was described using only the 6132 keV state. A new $3/2^+$ spin measurement by Laird *et al.* [52] for the 6072 and 6132 keV states provided further analogue possibilities for the, now questioned, 6497 and 6528 keV states in ^{19}F. From the R-matrix analysis in this work, it was found that such an assignment played a negligible role in the $3/2^+$

[1] Above threshold broad $1/2^+$ state predicted by Dufour & Descouvemont.
[2] Γ_t was limited to <14 keV due to the energy resolution in the measurement by Laird *et al.* [52].

interference, either used in conjunction with existing $3/2^+$ states or as replacements for the $3/2^+$ states above threshold (detailed in section 5.2.4). Shown in Fig. 1.9, the mirror assignments for these states were suggested solely on the value of their spin. The parities of the assigned pairs do not agree and no comparison can be made to their widths or spectroscopic factors. The assignments suggested are only intended as an exercise to highlight the current disagreements between the two mirror nuclei and the necessity for further scrutiny.

6282 | 6295 ($1/2^+$, $9/2^+$, $11/2^+$) The 6289 keV resonance was only recently observed to be a doublet by Parikh *et al.* [57], providing an explanation of the conflicting measurements by Laird, Bardayan *et al.* [61] and the measurement from this work. Angular distributions, shown in Fig. 4.19, are extracted from the α-particle decays of this state (taken to be a singlet of $E_x = 6289$ keV as resolved by the experimental data in this work) and suggest an l-value of 5, corresponding to a $J^\pi = 9/2^+$ or $11/2^+$. Fits to the data of both an isotropic and $l = 1$ ($J^\pi = 1/2^+$) distribution do not fit adequately and return χ^2/ν values an order of magnitude higher than that of the $l = 5$ fit. The analysis from this work can therefore affirm that the observed resonance cannot be a single state of $J^\pi = 1/2^+$. However, the existence of a second state, close in energy, is readily explained by all measurements of the resonance performed to date. Data by Adekola *et al.* [53] and Bardayan were taken using ^{18}F(d,n) and ^{20}Ne(p,d) reactions respectively whilst the data in this work and that of Laird, populated ^{19}Ne using the ^{19}F(^{3}He,t) reaction. It is feasible that the two reactions preferentially populated states depending on the required l-transfer. This leaves two options for interpreting the angular distributions in this work. Either the $J^\pi = 1/2^+$[1] is far lower in intensity and the distributions represent the spin from the second state, or both are populated to some proportion and the α-particle decay measurements are mixing from both. Unfortunately, given the resolution and asymmetry of the focal plane, resolving two peaks at $B\rho \simeq 0.975$ Tm with 13 keV difference was not possible. The statistics were also too low to reliably scan across small bins within the peak observing changes to the distribution. Investigations into the resonances' astrophysical importance considered both assignments of $J^\pi = 1/2^+$ and $J^\pi = 9/2^+$, $11/2^+$. The R-matrix calculations were performed using a spin parity of $1/2^+$ and an excitation energy of 6282 keV as the starting input parameters. Considering the $1/2^+$ resonance to be located at the higher energy of 6295 keV yielded a constriction in the S-factor uncertainty (see Fig. 5.3)

[1] It has been assumed that one of the states in the dublet retains its $J^\pi = 1/2^+$ assignment based on the strong measurements by Adekola and Bardayan.

due to the reduced interference with the 6008 keV $1/2^+$ subthreshold resonance. Some sensitivity to the proton's ANC was observed in Fig. 5.7 but no distinction could be made from changes to its α-particle width. If the resonance is treated as a single $J^\pi \neq 1/2^+$ state then the $1/2^+$ interference uncertainties are reduced substantially (Fig. 5.8 and 5.9).

6.1.2 Resonances Above $E_x = 6411$

6416 3/2⁻, 5/2⁺ The first resonance above threshold was unable to be isolated effectively on the focal plane due to the proximity of the 6416, 6440 and 6459 keV states. Since its measurement of $J^\pi = 3/2^-$ by Adekola, the state is no longer expected to contribute substantially to the S-factor. From this work, it was found that the ^{18}F(p,α) reaction rate was sensitive neither to its unknown partial widths nor its interference with other $3/2^-$ states. Treated as a $3/2^+$ state (shown in Fig. 5.9) its relevance increased, showing interference with both the 6459 and 7076 keV states. The 6497 keV state in ^{19}F, previously considered to be the analogue of the 6416 keV state in ^{19}Ne, was investigated for its measurement reliability. The first measurement of the analogue (^{15}N(α,γ)^{19}F) by Aitken *et al.* [90] identified a state at 6500 keV with J = 3/2. Angular distributions of the measurements were professed to appear in a subsequent publication, however, no such article exists. The second measurement, made by Dixon & Storey [91], agreed with the spin assignment of 3/2 from Aitken and inferred a positive parity, justifying that a negative parity would imply an M2 γ-ray transition strength of >6 W.u. to the 197 keV state. No data on the M2 transition strength have been published, however, and it is the view of this author that the possibility of a negative parity has not been excluded. If this is the case, then the mirror assignment between the 6416 keV state in ^{19}Ne and the 6497 keV state in ^{19}F may be retained, discontinuing the search for its missing $3/2^+$ analogue.

6437 1/2⁻ The population of the broad $1/2^-$ state just above threshold was too low to extract angular distributions. Aside from potential interference effects (discussed with the 6939 keV state), the state's primary contribution to the S-factor uncertainty lies in its unknown p width that dominates the strength of the resonance. Because of this uncertainty, the cross section changes substantially across the region of interest due to the state's high energy tail. The variation performed in this work (see Fig. 5.5) applied an order of magnitude difference to the p width which, whilst not unreasonable, is certainly toward the extremes of probability.

6440 11/2$^+$ As mentioned, isolation of the new state within the triplet (observed by Laird) was not possible and as such was omitted from the fitting routine. Its high spin and narrow width prevent the state from contributing toward the reaction rate and no change was observed from its inclusion or exclusion from the AZURE2 input parameters.

6459 3/2$^+$, 5/2$^-$ The highest energy state in the triplet is the 6459 keV. In the absence of angular distribution measurements from this work, the parameters of the state were taken from previous measurements by Adekola and Laird. In conjunction with the wide 7076 keV state, there is a large uncertainty in the direct capture rate from the possible interference between the two states when treated as $J^\pi = 3/2^+$ (see Fig 5.2). Variation in the state's unknown p width, estimated from its analogue in ^{19}F, causes further uncertainty in the reaction rate due, in part, to the state's location just below novae burning energies, and to the $3/2^+$ interference. If the $J^\pi = 5/2^-$ assignment from Laird is adopted then new width parameters, deduced in ref. [52], simultaneously produce a greater resonance strength and remove the $3/2^+$ interference (see Fig. 5.9). The $3/2^+$ assignment to the ^{19}F analogue state ($E_x = 6528$ keV) was investigated like the 6416 keV state before. The first observation by Smotrich *et al.* [92] (reanalysed by Bardayan *et al.* [40]) found a spin parity assignment of $3/2^+$. The second measurement by Dixon & Storey showed compelling evidence of a $3/2^+$ measurement in Fig. 4 of [91], indicating that its currently accepted assignment is correct. This would therefore imply that the original measurement of the ^{19}Ne 6459 keV level is correct, or that an alternative, $J^\pi = 5/2^-$, analogue state be assigned. The latter option is unlikely as no state in this region of ^{19}F is spin $J^\pi = 5/2^-$.

(6504) | 6537 (7/2$^+$, 9/2$^+$) The new 6537 keV resonance (found recently by Cherubini *et al.* [62]) is listed in this work as a replacement of the 6542 keV state given its similarity in energy, however (as quoted in ref. [62]), the spin of the state could not be confirmed beyond a $7/2^+$ or $9/2^+$ assignment and therefore the observed resonance could be either state. Inclusion of either state in the R-matrix calculations from this work suggested no contribution. The newly observed state was not included in the fitting routine as publication of the discovery was made subsequent to the analysis of the data. From Fig. 4.15, however, a poor fit to the data (inexplicable by background sources) suggests the presence of a further resonance within the spectra. Appendix D shows the focal plane re-fitted with states missing during the analysis of the data.

6700 ($5/2^+$) The 6700 keV resonance was observed in this data, although the population of the state was too low for angular distribution measurements. Its contribution is apparent from Fig. 5.1 though, as previously mentioned, no interferences with other $5/2^+$ resonances were observed from the R-matrix calculations. Its unknown p width taken from its mirror state in ^{19}F adds some uncertainty to the S-factor, though the width of the resonance and lack of interference mean that the reaction rate is predominantly unchanged.

6742 $3/2^-$ α-particle distribution data for decays from the 6742 keV state, plotted in Fig. 4.20, suggest a decay with an $l = 2$ transfer corresponding to a J^π of $3/2^-$ or $5/2^-$. This is in agreement with previous measurements of $J^\pi = 3/2^-$ and the distribution of the 6014 keV state ($J^\pi = 3/2^-$) measured earlier. The resonance lies within the novae temperature range and so contributes directly toward the ^{18}F(p,α) reaction rate. Its interference with the $3/2^-$ resonance at 6416 keV is negligible across the region of interest, however, with the discovery of the doublet by Parikh, there is substantial interference with its broad 6851 keV neighbour. The effect of this interference is discussed alongside the 6851 keV state.

6851 ($3/2^-$) Found recently by Parikh, the missing $3/2^-$ state has been measured at E_x = 6851 keV to have Γ_t = 40 keV. The width of the resonance, shown in Fig. 5.1, adds a substantial contribution to the S-factor just above the nova temperature range where direct measurements of the reaction have been made. If this resonance were not present (as in the calculations from Fig. 1.10), interference terms would be more separated and fewer terms would be comparable to the data. The resonance also interferes with the 6742 keV state below, creating further uncertainty in the S-factor at this energy and allowing other $1/2^+$ and $3/2^+$ interference patterns to be included. The p width of the state is taken from its mirror assignment and the α-particle width (assumed to be the total width measurement from Parikh) is subject to a large error. Both of these parameters were explored in Fig. 5.6 and show how the data can be described by both the minimum and maximum interference terms (listed on page 108) within the boundaries of their errors. An accurate measurement of the resonance's parameters could be successful in isolating interference terms using existing direct measurments.

6864 $7/2^+$ Angular distribution measurements of α-particle decays from the 6864 keV state have been shown in Fig. 4.21. Legendre polynomial fits to the data show a minimum χ^2/ν when terminated at k = 6. This would imply an $l = 3$ transfer from the decay and therefore a spin of $J^\pi = 5/2^+$ or $7/2^+$. Previous measurements of the state however,

including those by Visser *et al.* [83] and Laird, suggest a J^π of $7/2^-$. Such a spin would require a 4^{th} order polynomial and a local maximum in α-particle counts at $\theta = \pi/2$, unlike the minimum seen in Fig. 4.21. The similarity of the state's distribution to that of the 7420 keV resonance, also thought to be $J^\pi = 7/2^+$, adds credit to this work's assignment. Its analogue state in ^{19}F at $E_x = 6927$ keV is unambiguously measured to be $J^\pi = 7/2^-$ [29] suggesting that the measurement from this work is mistaken. The contribution of this resonance, as either $7/2^+$ or $7/2^-$, is negligible to the ^{18}F(p,α) reaction rate and was excluded from the calculations in Chapter 5.

(6939) (1/2$^-$) | ***6968 (5/2$^+$)*** The observation of a resonance at 6968 keV by Cherubini, with an indirectly measured $J^\pi = 5/2^+$, provided a good candidate for the missing 7054 keV resonance. The resonance at its current excitation energy, shown in Fig. 5.6, explains the structure of the data measured by Bardayan *et al.* [35], but is unable to assist in the constraint of interference terms. The state was also included in a new focal plane fit shown in Appendix D. The 6939 keV state (still missing) is expected from its mirror state to have $\Gamma_\alpha = 99$ keV and $J^\pi = 1/2^-$. These parameters present a non-negligible contribution to the direct capture rate due to interference between the 6437 and 6939 keV states. The $1/2^-$ interference terms have been omitted in the current work due to insignificant interference between the known 6437 and 7644 keV states, however, Appendix C shows the S-factor calculations when including the missing $1/2^-$ state.

7076 3/2$^+$ The 7076 keV state ($E_{\text{c.m.}} = 665$ keV) is the dominant feature of direct reaction rate measurements whose tail remains significant at astrophysical energies (Fig. 5.1). Its mirror analogue in ^{19}F (predicted by Bardayan *et al.* [40]) is one of the few resonances in the mirror nucleus yet to be observed. The angular distribution from this work (Fig. 4.22) suggests an $l = 1$ transfer indicative of the accepted $J^\pi = 3/2^+$ assignment. As energy thresholds in the electronic signal processing were set too high, the low energy p decays from the 7076 keV state were not able to be detected. A measurement of the Γ_α/Γ_p ratio would have been advantageous, in the first instance for confirming the accuracy of the angular distribution fitting and, in the current situation, for understanding the discrepancy between the erroneous branching ratios. Because of the resonance's spin assignment, the $3/2^+$ interference patterns were formerly thought to provide the largest uncertainty to the reaction rate. Since the re-assignment of the 6416 keV to $3/2^-$ and the introduction in this work of the $1/2^+$ interference, the role of the $3/2^+$ interference has been diminished. Fig. 5.2 best shows this re-assignment of priorities, where the effect of the $1/2^+$ in the

novae temperature range is an order of magnitude higher than that of the $3/2^+$. Fig. 5.9 also shows that if the interference from the 7076 keV state is between any state other than the 6459 keV, then the $3/2^+$ interference is almost entirely removed.

7173 11/2$^{(-)}$ This state was observed in the experimental work, although no contribution to the reaction rate seen from R-matrix calculations as expected of its high spin. Low statistics and proximity to the 7238 and 7253 keV states also prevented measurements of its p or α-particle angular distributions.

7238 3/2$^+$ | 7253 (1/2$^+$) The interference between the 7076 and 7238 keV states extend down to the astrophysical energies thanks, to the width and strength of the former. The effect of the 7253 keV resonance on the $1/2^+$ interference only becomes influential when the interference between the two broad $1/2^+$ resonances is destructive. At these cross sections, its presence can increase uncertainty in the region of interest by up to a factor of 3. Despite a smaller contribution to the direct capture uncertainty at lower energies, the interference patterns from both the 7238 and 7253 keV states remain important as there could be opportunities, such as those taken by Chae *et al.* [41], where measurements above the 7076 keV state could help to isolate interference terms below. Due to the low population of the states and their proximity to one another, the extraction of angular distributions in this work from either state was not possible.

7420 7/2$^+$ The 7420 keV state was isolated sufficiently on the focal plane for α-particle decay distributions to be extracted. The distributions, shown in Fig. 4.23, are in agreement with the spin assignment from Bardayan *et al.* [39] and contradicts the conclusion from the last measurement of the state by Murphy *et al.* [59] who concluded that the resonance did not exist. The partial widths of the state, measured by Bardayan, mean that the resonance is notably strong and has been included in the R-matrix analysis for the structure it provides at $\sim$1 MeV (see Fig. 5.1). Its widths retain a small uncertainty, and whilst not influential to the reaction rate for nova burning, could misguide direct measurements such as those by Chae if not constrained further.

7500 5/2$^+$ The 7500 keV state is strongly populated in comparison to other states within the region allowing both α-particle and p decays to be measured. Fig. 4.24 shows the distribution pattern of each where, if the p is assumed to decay via the lowest orbital momentum transfer, Legendre polynomial fits to each are in agreement. A fit of $l = 3$ and $l = 2$ for the α-particle and p distributions respectively imply a J^π of $5/2^+$ or $7/2^+$.

Investigation of the state in R-matrix calculations showed no direct contribution from the state and, as noted in section 5.2.1, there was no $5/2^+$ interference to be considered.

7531 5/2⁻ | (7558) (5/2⁻) The 7531 keV resonance was included in the fitting routine for the ^{19}F(^{3}He,t) experimental data and Appendix D shows the inclusion of the missing 7558 keV state. Neither the observed nor the missing resonance contribute to the ^{18}F(p,α) reaction rate between 0.05 and 0.35 GK, however, the existence of the missing state is postulated by the observation of its mirror state in ^{19}F, the J^π of which is unmeasured. If this were to be changed from its current assignment of $5/2^-$ to one of known interference contributions, its importance to the ^{18}F destruction in novae may increase.

7616 3/2⁺ Detections of both α and p particles from the 7616 state were able to be made, shown in Fig. 4.25. Because of the low count rate, the Legendre polynomial fits to the data are the least confident in this work. Only a small improvement in χ^2/ν identifies the best fit, however, the fit does correspond to $l = 2$ and $l = 0$ for the α-particle and p data respectively which ultimately correspond to the accepted J^π of $3/2^+$. The partial widths, measured by Utku *et al.* [36] and listed in Table 5.1, showed no reaction rate sensitivity to their errors, however the state was retained during R-matrix calculations for completeness of the $3/2^+$ interference description (for which it provides a slight contribution).

7644 (1/2⁻, 3/2⁻) Interference effects from the 7644 keV state do not contribute to the reaction rate either as $J^\pi = 1/2^-$ or, as suggested by Murphy, as $J^\pi = 3/2^-$ and, therefore, was excluded from Table 5.1. The state was included in the focal plane fit, although its low statistics and proximity to neighbouring states prevented angular distribution measurements that could confirm the resonances spin-parity.

7700 (5/2⁻) The 7700 keV resonance was observed in this work but no angular distributions could be extracted. Investigated during R-matrix calculations, the state has no contribution toward the reaction rate of interest.

7758 3/2⁺ Whilst the dominating interference contribution between $3/2^+$ states arises from the 6459 and 7076 keV, the 7758 has still been included for completeness, given its non negligible shift in the S-factor. Observed by Murphy, and later again by Mountford *et al.* [64], the state has yet to be proposed a mirror assignment due to a lack of suitable analogue states in the region. No angular distributions from this state were able to be extracted from either the α or p particle coincidences

7819 ($7/2^+$) | ***(7826) ($11/2^+$)*** The 7819 keV resonance was observed from the (^{3}He,t) reaction to have a strong p decay channel. However, due to the level density in the region, no angular distributions could be extracted. R-matrix calculations do not show this state nor the missing 7826 keV state to have any impact on the ^{18}F(p,α) reaction rate in novae.

7879 $1/2^{(+)}$ The broad $1/2^+$ state above threshold (unobserved in this work) has been shown from the R-matrix calculations to contribute significantly to the direct capture rate uncertainty. Discussed previously, this is due to its unknown interference with the subthreshold resonance at E_x = 6008 keV. As with its subthreshold companion, the uncertainty in its α-particle and p partial widths makes little difference in comparison to its interference term (see Fig. 5.2).

7944 ($5/2^+$) | ***7984 ($1/2^+$)*** | ***(8014) ($3/2^+$)*** | ***8072 ($1/2^+$)*** Not shown in Fig. 4.15, resonances above 7850 keV were not well isolated on the focal plane and no features were visible that could be meaningfully extracted from the fitting routine. None of the states had any impact on the reaction rate at astrophysical energies either through resonance capture or through additional interference between $1/2^+$ or $3/2^+$ states. The suggested mirror assignment by this author (see Fig. 1.9) for the 7984 keV observed by Murphy has been made due to the unknown spin and potentially broad width (<50 keV) of the 8160 keV state in ^{19}F, making it the only suitable candidate.

6.2 Experimental Branching Ratios

As part of the α-particle and p decay distribution measurements, it was expected that the branching ratio of each decay channel could be calculated from the fit to the distribution (eq. 4.6). However, as shown in section 4.6.3, the results from the integration were unphysical and were attributed to the lower count ratios in the angular bins (see Fig. 4.26). Whilst considerable effort has been made to find the source of the discrepancy, as yet, no explanation has been found. To extract the ratios (for a single excitation energy) the counts from an α-particle or p coincidence peak were compared, after efficiency corrections, to those from the triton singles peak. There are several points of failure that could arise from this analysis.

First, the counts in the singles peak may be too high. The possibility of duplicate events being generated in the DAQ was investigated, however, no evidence was found to support

this hypothesis. A more likely cause for this scenario is unaccounted background in the triton spectra. Potential reactions were plotted in a similar manner to Fig. 3.16 and 3.17, using the kinematics of the beam to calculate their path through the Split-pole, but no other triton sources could be identified. The background from the bleeding deuteron spectrum was also well accounted for (section 4.4.2) rendering this scenario unlikely.

The second possibility is that the count rate in the silicon array was too low. The analysis of the ^{19}F(^{3}He,t)^{19}Ne data involved a series of cuts to select only valid events in coincidence with the tritons. These cuts were scrutinised closely to ensure no true α/p coincidences were rejected, however, no superfluous event loss could be identified. An alternate possibility was that the DAQ was not able to process the events quickly enough. For the average beam current (75 enA), the trigger rate from the Split-pole was $\sim$300 events s^{-1}, however, the count rate in each silicon detector was measured to be $\sim 5-6 \times 10^4$ events s^{-1} due to their much wider coverage in the chamber compared to the Split-pole aperture. It was thought that a pile-up of events may distort the data causing the detected energy to be measured incorrectly and prevent the identification of coincident decay. This was found not to be the case as there was no correlation between the branching ratios and beam current. Given the branching ratio's dependence on excitation energy, the timing from the TDCs was investigated[1], however, the distinction of the timing peak and its position in the window meant ToF measurements were unlikely to be the cause. Plots of EvE such as those in Fig. 4.10 were plotted for timing cuts made off the ToF peak but, as expected, no α-particle or p loci were visible.

A third possible misstep in the analysis was the efficiency correction made to each angular bin to account for the partial geometrical coverage. The simulations were run using detector positions measured by hand during the experiment. The error from the measurements ($\pm$1 mm) were also input into the simulations to provide the efficiency error but were too small to account for the branching ratio's factor of 2.5 discrepancy from the literature. Another conceivable reason is that the procedure for calculating each angular bin's efficiency was wrong (see eq. 3.5), although discussion amongst the collaboration found this not to be the case. The translation from laboratory to centre of mass coordinates was another vulnerability, however, like the efficiency calculations before, no incorrect methodology could be found. Efficiency calculations from an isotropic source were used to plot the

[1]Lower energy tritons have a longer time of flight through the Split-pole (see Fig. 4.3.4).

distributions from a triple α-source measurement, using the same method for coincidence data, and successfully recreated the sources isotropic nature and expected decay rate.

The last point of investigation was the unusual data structure inherited by the majority of recorded events. Approximately $^{3}/_{5}^{\text{th's}}$ of the data required discarding due to no TDC measurement for any of the silicon hits (i.e. tdcN = 0). Attempts were made to plot this subset of data in order to identify the presence of any ^{19}Ne particle decay, however, due to the lack of ToF selection, nothing could be observed above background. An explanation for the loss of timing information was that the DAQ TDC window spanned 2 μs (its maximum setting) and the ADC window spanned 5 μs (its default setting). A $^{2}/_{5}^{\text{th's}}$ proportion of events that contain TDC data therefore seemed reasonable, however, this has yet to be fully investigated with respect to the trigger rate and silicon hit rate and thus remains the only line of enquiry still open.

Branching ratios in the Yale experiment [83] were initially calculated at lower rates as well, although they were able to be accounted for in the analysis. The isotropic α-particle decay from the 5351 keV $1/2^{+}$ state was analysed first and found to have a branching ratio of <100%. The state is known to decay purely through the α-particle channel and so the data (with no energy dependence) were renormalised accordingly. The explanation for the Yale discrepancy was attributed to a "function of the hardware triggering", though no further elaboration was provided. The differences to the Orsay data, however, were that the ratios were extracted on the order of 80% of their expected values (vastly different from the ∼30% from Orsay) and also that the reduction in branching ratio was systematic across all energies in the Yale case.

The discrepancy is particularly concerning as experiments with a similar experimental set-up to that used in this work have already been performed, making the resolution of the branching ratio discrepancy of paramount importance.

6.3 Further Work

6.3.1 Indirect Reactions

Some of the largest uncertainties in the ^{18}F(p,α) reaction rate arise from resonance parameters just above and just below the p-threshold. These states are inaccessible to direct

measurement due to their low cross sections and must, therefore, be measured through other methods. The complications in the ^{19}F(^{3}He,t)^{19}Ne experiment performed at Orsay mean that there is still value in its repetition. A higher energy resolution in the focal plane, for instance, would be able to isolate the triplet of states above threshold to measure the J^{π} and Γ_{α} (possibly Γ_{p} with sufficient statistics) of the 6416 and 6459 keV states. Whilst separation of the 6282 and 6295 keV subthreshold states is unlikely with the Split-pole, improved statistics could allow decay distributions to be observed for smaller energy bins in order to calculate possible spin parity contributions from each.

The constraint of interference terms was limited due to the knowledge of the new broad $3/2^{-}$ state at $E_x = 6851$ keV. If indirect measurements were able to determine its partial widths, it is possible that data in the region could only be described by a much smaller selection of $1/2^{+}$, $3/2^{+}$ and $3/2^{-}$ interferences resulting in a reduced uncertainty at lower energies. Similarly of the 6968 keV state, given its recent discovery, all of its parameters have been taken from its ^{19}F analogue. The tail of the resonance impacts the exclusion of interference terms using current direct measurement data, and its constraint through indirect measurement may also be necessary.

The reaction rate was shown to have little sensitivity to the width or energy of the new subthreshold state ($E_x = 6008$) found in this work. However, its presence greatly influences the $1/2^{+}$ interference. Confirmation of this resonance, and its spin, is fundamental to understanding the reaction rate at nova temperatures and can only be measured using indirect techniques.

6.3.2 Direct Reactions

The largest source of uncertainty in the ^{18}F(p,α) reaction rate to emerge from the R-matrix calculations was the divergence between the $1/2^{+}$ and $3/2^{+}$ interference sequences. It is not possible to extract the interference term of a state experimentally using indirect techniques as can be done for the partial width, spin-parity and energy parameters. Only direct-capture (off resonance) yield measurements of the reaction can suggest if resonances are interfering constructively or destructively.

Shown in Fig. 2.4 from Chapter 2, the reaction probability decreases exponentially with decreasing energy due to the Coulomb barrier the particles must overcome. Therein lies

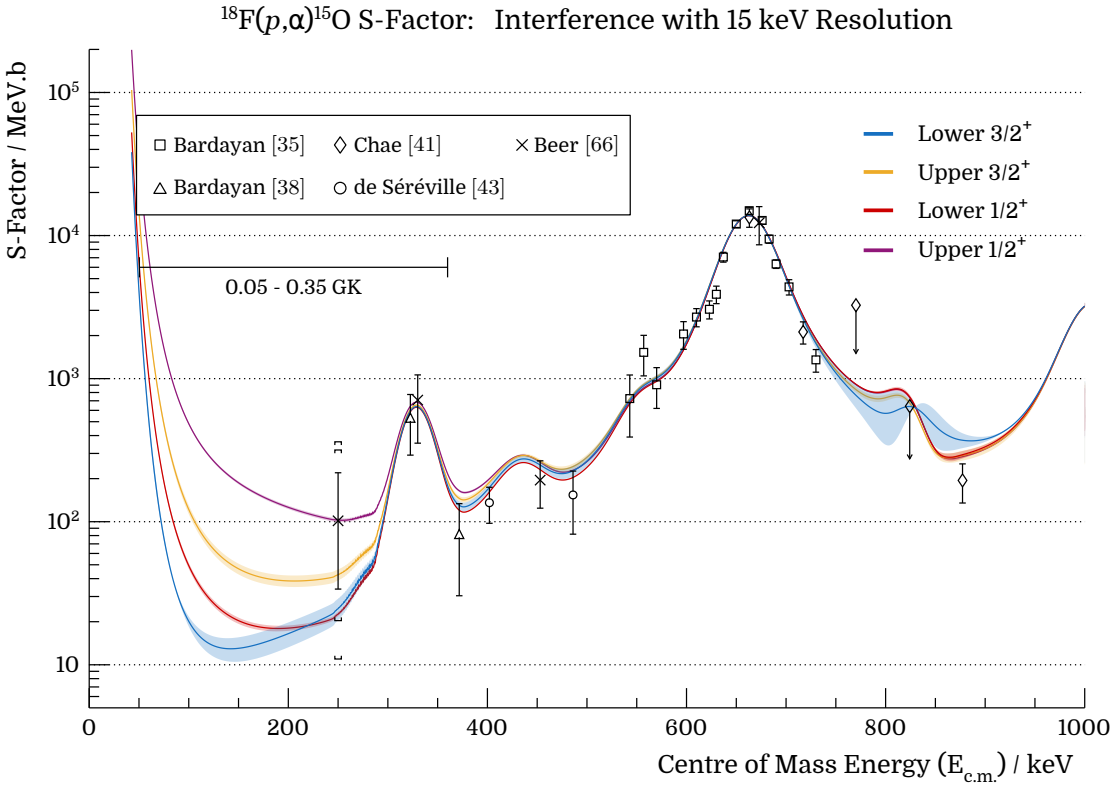

Figure 6.1: S-factor uncertainty from spin parity interference, calculated with a 15 keV Gaussian convolution. The S-factor curves have the same range as the 'nominal' plots in Fig. 5.3 to 5.9 but show additional interference bands as explained in the text.

the predicament of the ^{18}F + p system, where the largest uncertainty in the reaction rate is within the typical novae temperature, only a few hundred keV above the separation energy. Whilst providing the best measurement for identifying the correct interference, the reaction would be too slow for a reasonable experimental proposal given current beam intensities. There may, however, be other energies outside the novae temperature range where interference patterns are sufficiently separated to allow for correct interference identification but with an exponentially higher reaction rate. Using the R-matrix formalism, the rate could then be extrapolated down to the relevant energies.

In order to identify these regions, the S-factors were re-calculated using eq. 5.1 to convolute the resonances and simulate expected S-factor measurements observed with a 15 keV energy resolution. Fig. 6.1 shows the new calculations with the distinct bands that emerge from the interference between the $1/2^+$ and $3/2^+$ resonances. The 'lower $3/2^+$' is from destructive interference between the 48 and 665 keV resonances, the 'lower $1/2^+$' is from destructive interference between the subthreshold resonances but constructive interference

between the two broad states, the 'upper $3/2^+$' originates from constructive interference between the 48 and 665 keV resonances and finally the 'upper $1/2^+$' is from constructive interference both between the subthreshold and broad resonances.

Figure 6.2: Cross section difference between upper and lower estimates as shown in Fig. 6.1, plotted against the corresponding absolute σ. The dashed lines show potential energies for direct measurement either side of the 331 keV resonance.

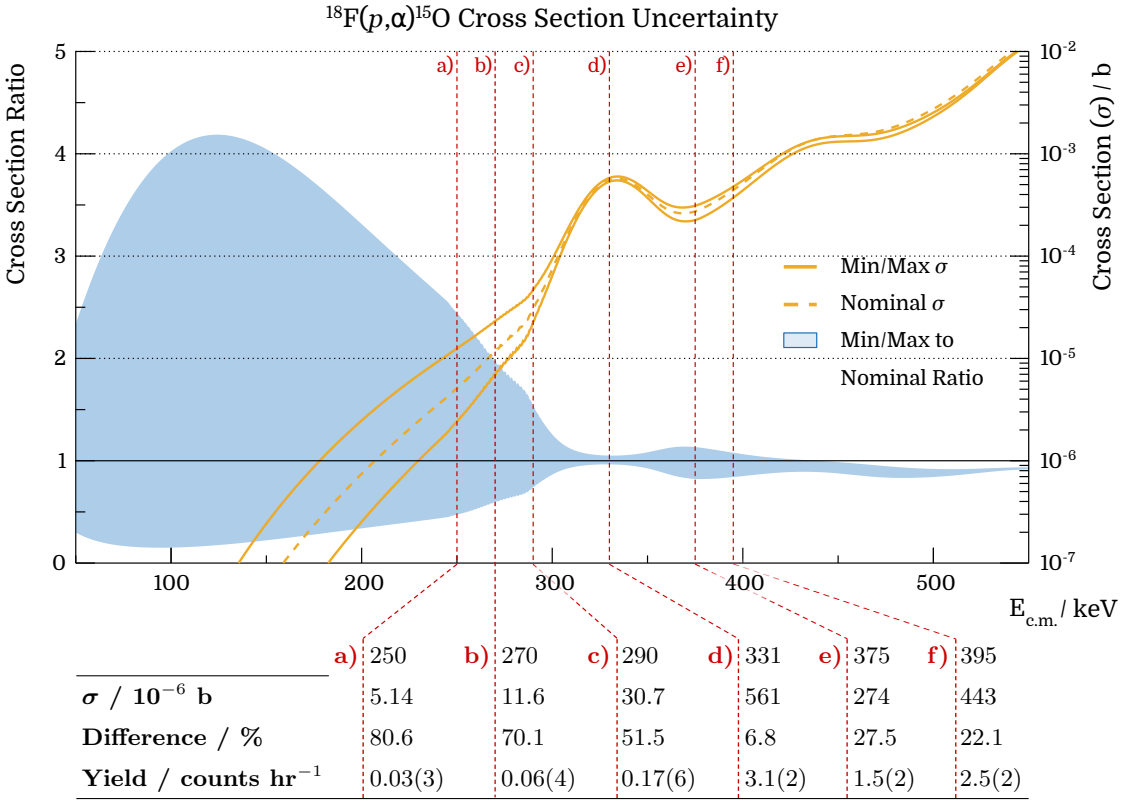

	a)	b)	c)	d)	e)	f)
	250	270	290	331	375	395
σ / 10^{-6} b	5.14	11.6	30.7	561	274	443
Difference / %	80.6	70.1	51.5	6.8	27.5	22.1
Yield / counts hr^{-1}	0.03(3)	0.06(4)	0.17(6)	3.1(2)	1.5(2)	2.5(2)

Table 6.1: Yield estimates for direct measurement reactions at energies either side of the 331 keV resonance. Lower energies offer greater separation to compensate current systematic errors but with a larger statistical error.

Fig. 6.2 shows the ratio between the maximum and minimum cross sections taken from the same convoluted calculations in Fig. 6.1 and the nominal absolute cross section (taken to be the 'upper $3/2^+$' band) for comparison. The off-resonance energies both above and below the 331 keV still offer a difference of ∼50% between the upper and lower interference terms but with a cross section 1-2 orders of magnitude higher. With greater statistics at higher energies, the yield measurement uncertainties reduce and smaller differences in interference can be observed, (though only until systematic errors begin to dominate). Table 6.1 lists yield estimates for a potential beam intensity of 5×10^6 particles per second for the nominal cross section surrounding the 331 keV resonance.

Chapter 7

Conclusion

To improve our knowledge of expected γ-ray emissions from novae, an experiment was performed to observe the resonances of ^{19}Ne and measure their parameters. The states were populated using the ^{19}F(^{3}He,t)^{19}Ne charge exchange reaction by accelerating ^{3}He to 25 MeV through the tandem accelerator at Orsay IPN onto a CaF_2 target. Triton ejectiles from the reaction were analysed using the Split-pole magnetic spectrometer to identify the populated states. Using an array of silicon detectors, coincident α-particle and p decay products from the populated ^{19}Ne* states were also able to be measured. The Split-pole accepted triton momenta from ^{19}Ne states between 2 and 8 MeV, whilst α-particle and proton emissions were detected from states above $E_x \simeq 5.5$ MeV and $E_x \simeq 7.5$ MeV respectively, as a function of their angle of emission.

Fits to the triton singles spectrum at the Split-pole focal plane identified states close to the proton threshold ($E_x = 6411$ keV) that were of astrophysical importance. In particular, evidence of a new state was located at 6008 keV, identified by the significant improvement to the fitting minimisation χ^2. Given its location and fitting parameters, it is strongly believed to be the broad subthreshold state ($J^{\pi} = 1/2^{+}$) previously postulated to exist. Calculations of the energy and total width correspond well with the unpublished parameters by Boulay *et al.* [60].

Detections of the decay particles, sensitive to their position, yielded angular distribution measurements from which their spin-parity was determined. Following complications with the ion source used in the experiment, resolution of the focal plane was lower than expected and prevented the isolation of a number of states. Those states for which no parameters

could be measured, included the triplet above the p-threshold that are known to influence the reaction rate. Whilst unfortunate, alpha-particle decay distributions from a critical state at $E_x = 6289$ were able to determine a spin of $J^\pi = 9/2^+$ or $11/2^+$. This is in direct contradiction with results from previous measurements that suggest the state to be of spin $1/2^+$. The different population methods were advocated to be the cause for the discrepancy, indicating there may be multiple states at that energy. This work can therefore conclude that the observed resonance cannot be a single state of spin $1/2^+$.

Intended measurements of α-particle or p branching ratios for the populated resonances were not possible due to discrepancies observed between the triton singles and α/p coincidences. Data from this experiment were compared to similar measurements made by Visser *et al.* [83] and showed a clear reduction in single to coincidence ratio (with a dependency on excitation energy) responsible for the weakened branching ratios observed. Investigations into the data set from Orsay are still ongoing and must be resolved before further measurements using this experimental setup are conducted.

A review of the ^{19}Ne resonance measurements conducted in the last decade since the publication by Nesaraja *et al.* [50] (including the experimental data from Orsay), was conducted as part of this work to assess the present state of the ^{18}F(p,α) reaction rate, and in particular the rate pertaining to nova burning temperatures. The importance of each state was determined in a series of calculations using the R-matrix formalism to estimate reaction cross sections from ^{19}Ne resonance parameters. Resonance energies ($E_{c.m.}$), partial widths (Γ) and spins (J^π) were input into the R-matrix code AZURE2 to explore the uncertainty from their measurements and resulting interference.

From the theoretical calculations, it was found that the reaction rate was particularly sensitive to resonance interference between $J^\pi = 1/2^+$ states. The primary cause for this was the presence of the broad $1/2^+$ state at 6008 keV and its interference with both the 6289 ($J^\pi = 1/2^+$) and 7879 keV resonances. Other interferences shown to impact the reaction rate are the $3/2^+$, $3/2^-$ and, if the missing broad state at 6939 keV is found, the $1/2^-$ states.

If the spin of the 6289 keV state is $J^\pi = 9/2^+$ or $11/2^+$, as found in this work, the uncertainty in the rate from interference between the $1/2^+$ states is reduced by up to a factor of 10. The ambiguity of the level's spin has led to the suggestion that the state is in fact a doublet, leading to the questioning of the $1/2^+$ state's position and introducing

further uncertainty. In addition, the 5459 keV state has uncertain spin-parity, and if included as $J^\pi \neq 3/2^+$ then the $3/2^+$ interference is also reduced to a negligible impact. S-factor comparisons to data from direct reaction measurements were able to exclude some constructive interference terms though further exclusions were prevented by the parameter uncertainties of the 6851 keV state situated in the data measurement region. Finally, the unmeasured proton widths for the states closest to the temperature range of interest, result in a large uncertainty in their predicted values. An order of magnitude variation in the proton widths of the 6437 and 6459 keV states were found to increase reaction rate uncertainties by up to two orders of magnitude.

After consideration of all ^{19}Ne* excitations from 6 to 8 MeV, the nominal uncertainty in the ^{18}F(p,α)^{15}O reaction rate was concluded to be up to a factor of 10. This is an increase from the factor of 5 (calculated last by Bardayan *et al.* [61]) primarily due to the inclusion of the broad 6008 keV proton subthreshold state. Reaction rates were also compared to those calculated in the last review paper by Iliadis *et al.* [85] (included in the STARLIB reaction rate library). Similar increases to the maximum uncertainty were observed, and deviations from the STARLIB rate at low temperatures were due to the treatment of the near-threshold resonances by Iliadis as $J^\pi = 3/2^+$.

The reaction rates were included in post-processing and hydrodynamic astrophysical codes that model the temperature and density profiles expected in novae. Modelling the ^{18}F(p,α) reaction using the maximum and minimum rates calculated in this work showed a direct impact on the ^{18}F produced in the runaway. Uncertainty in the rate yielded an uncertainty in the ^{18}F abundance of between a factor of 4 to a factor of 8 (depending on the conditions of the nova) - a substantial increase from the previously assumed factor of 2. Nominal rate comparisons to the STARLIB reaction rate show an increased production of ^{18}F by a factor of 50%, increasing the potential observation range of its decay by a factor of $\sqrt{1.5}$.

The unpredictability of ^{18}F abundance in novae, shown to be higher in this work than previously thought, means that study of its primary method of destruction, ^{18}F(p,α)^{15}O, must continue. Both indirect measurements of the ^{19}Ne compound nucleus, and direct measurement of ^{18}F(p,α) cross sections are necessary in order to address the dominant causes for its uncertainty identified in this work. Only when the nuclear physics input is constrained can our capability of detecting nucleosynthesis within novae be achieved, allowing us to further our understanding of these nuclear powered explosions in the cosmos.

Appendix A

Coordinate Transformation

To transform the silicon array coordinates from the laboratory to centre of mass frame of reference, the kinematics of the reaction had to be calculated in order to know the direction and momentum of the centre of mass of the decay (the moving ^{19}Ne).

A.1 Two Body Kinematics

The reaction proceedes as A(a,b)B where A is the ^{19}F target, a is the ^{3}He beam, b is the triton ejectile and B is the ^{19}Ne reactant (the momentum of which is desired result). Beginning from energy and momentum conservation

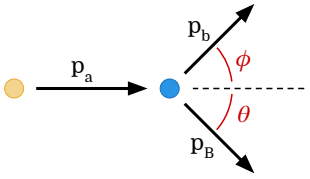

Momentum Conservation

$$\begin{aligned} p_a &= p_b\cos(\phi) + p_B\cos(\theta) \\ 0 &= p_b\sin(\phi) - p_B sin(\theta) \end{aligned} \tag{A.1}$$

Energy Conservation

$$E_a + Q = E_b + E_B + E_x = E_{\text{tot}} + E_x \ , \tag{A.2}$$

where Q is the Q-value ($Q = m_a + m_A - m_b - m_B$) and E_x is the excitation energy of the particles after reaction. Rearranging eq. A.1

$$(p_a - p_b\cos(\phi))^2 = p_B^2\cos^2(\phi) \tag{A.3a}$$

$$p_a^2 + p_b^2\cos^2(\phi) - 2p_a p_b\cos(\phi) = p_B^2\cos^2(\phi) \ , \tag{A.3b}$$

and adding equations A.3a and A.3b produces

$$p_a^2 + p_b^2 - 2p_a p_b \cos(\phi) = p_B^2 \ . \tag{A.4}$$

From the conservation of energy (eq. A.2) and that $E = \frac{p^2}{2m}$, the momentum of particle B can also be calculated via

$$E_{\text{tot}} - \frac{p_b^2}{2m_b} = \frac{p_B^2}{2m_B} \tag{A.5}$$

$$\Rightarrow \quad p_B^2 = 2m_B \left(E_{\text{tot}} - \frac{p_b^2}{2m_B} \right) \ . \tag{A.6}$$

Substituting the result above into eq. A.4 yields

$$p_b^2 \left(1 + \frac{m_B}{m_b} \right) - p_b(2p_a \cos(\phi)) + (p_a^2 - 2m_B E_{\text{tot}}) = 0 \ , \tag{A.7}$$

which can be solved as a quadratic equation. In particular, the quantities of importance to this work can be calculated as follows

$$p_B = \sqrt{2m_B(E_{\text{tot}} - E_b)} \tag{A.8}$$

$$\theta = \sin^{-1}\left(\frac{p_b}{p_B} \sin(\phi) \right) \ . \tag{A.9}$$

A.2 Three Dimensional Frame Rotation

Using the kinematics described above, the direction of the recoiling ^{19}Ne (eq. A.9) gives the frame rotation required. As the silicon detectors do not fall on a flat plane, both θ and ϕ used to describe each pixels position must be transformed.

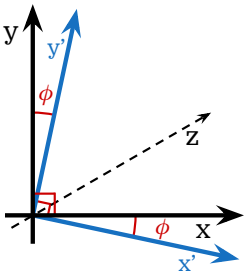

Rotation through ϕ

$$\begin{aligned} x' &= X\cos(\phi) - Y\sin(\phi) \\ y' &= X\sin(\phi) + Y\cos(\phi) \\ z' &= Z \end{aligned} \tag{A.10}$$

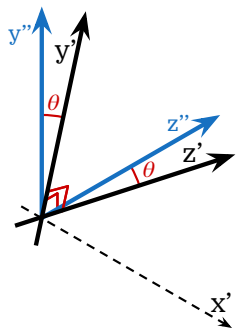

Rotation through θ

$$\begin{aligned} x'' &= X' \\ y'' &= X'\cos(\theta) - Z'\sin(\theta) \\ z'' &= Y'\sin(\theta) + Z'\cos(\theta) \end{aligned} \tag{A.11}$$

The resulting rotation matracies can be multiplied together

$$\begin{aligned} \begin{pmatrix} x'' \\ y'' \\ z'' \end{pmatrix} &= \begin{pmatrix} 1 & 0 & 0 \\ 0 & \cos(\theta) & -\sin(\theta) \\ 0 & \sin(\theta) & \cos(\theta) \end{pmatrix} \begin{pmatrix} \cos(\phi) & -\sin(\phi) & 0 \\ \sin(\phi) & \cos(\phi) & 0 \\ 0 & 0 & 1 \end{pmatrix} \begin{pmatrix} Y \\ X \\ Z \end{pmatrix} \\ &= \begin{pmatrix} \cos(\phi) & -\sin(\phi) & 0 \\ \cos(\theta)\sin(\phi) & \cos(\theta)\cos(\phi) & -\sin(\theta) \\ \sin(\theta)\sin(\phi) & \sin(\theta)\cos(\phi) & \cos(\theta) \end{pmatrix} \begin{pmatrix} Y \\ X \\ Z \end{pmatrix} , \end{aligned} \tag{A.12}$$

The transpose of eq. A.12 can be used to transform the rotated frame (x'', y'', z'') to the original, non-rotated frame (X, Y, Z). The cartesian coordinates can also be rewritten in sperical polar coordinates using the following expressions

$$\begin{aligned} x &= r\sin(\theta)\sin(\phi) \\ y &= r\sin(\theta)\cos(\phi) \\ z &= r\cos(\theta) \ . \end{aligned} \tag{A.13}$$

A.3 Lorentz Transformation

The recoiling ^{19}Ne also carries momentum calculated using eq. A.8, moving with a velocity β. The Lorentz matrix below can be used to transform the inertial frame $(')$ to the observers frame

$$\begin{pmatrix} E_s \\ p_x \\ p_y \\ p_z \end{pmatrix} = \begin{pmatrix} \gamma & \gamma\beta_{x'} & \gamma\beta_{y'} & \gamma\beta_{z'} \\ \gamma\beta_{x'} & 1+(\gamma-1)\frac{\beta_{x'}^2}{\beta^2} & (\gamma-1)\frac{\beta_{x'}\beta_{y'}}{\beta^2} & (\gamma-1)\frac{\beta_{x'}\beta_{z'}}{\beta^2} \\ \gamma\beta_{y'} & (\gamma-1)\frac{\beta_{y'}\beta_{x'}}{\beta^2} & 1+(\gamma-1)\frac{\beta_{y'}^2}{\beta^2} & (\gamma-1)\frac{\beta_{y'}\beta_{z'}}{\beta^2} \\ \gamma\beta_{z'} & (\gamma-1)\frac{\beta_{z'}\beta_{x'}}{\beta^2} & (\gamma-1)\frac{\beta_{z'}\beta_{y'}}{\beta^2} & 1+(\gamma-1)\frac{\beta_{z'}^2}{\beta^2} \end{pmatrix} \begin{pmatrix} E_0 \\ p'_x \\ p'_y \\ p'_z \end{pmatrix} , \tag{A.14}$$

where E_s is the doppler shifted energy, E_0 is the energy in the frame of the ^{19}Ne and γ is the lorentz factor $(1 - {}^{v^2}/_{c^2})^{-1/2}$.

Appendix B

Angular Bin Background

Due to the ordering placed in the sort code, it was not possible to calculate the background from coincidental events below the timing peak directly for each angular bin. Instead, the background was modelled for each detector and applied proportionally to the detector composition for that bin. Below is a section of code that analyses the Monte-Carlo simulations run for each resonance energy and outputs the parameters of each bin, including the bin width (error in θ), the weighted average θ, the bin efficiency and the detector composition of the bin.

```
for (int j=1; j<NoBins+1; j++){          #loop over angular bins
  BinMean[j] /= BinCount[j];     //BinMean = SUM(theta)/SUM(count)
  BinNorm[j] = (1 / ((Double_t) BinCount[j] / TotalCount)) / (4*3.141592);
                                 //final bin efficiency.
  for (int k=1; k<7; k++){               #loop over detectors
    DetBinRatio[k][j] = (Double_t) DetBinCount[k][j] / DetCount[k];
                                 //ratio of counts from detector k in bin j
  }
}
```

The following code counts the average background for each detector from their respective TDC spectrum (eg. Fig. 3.15) and outputs to the variable `BG_D` and its associated error to `BG_Err_D`.

```
for(Int_t i=1; i<7; i++){                #loop over detectors
  ecl_name = Form("ecl_bg_D[%d]",i);
  htiming = (TH1*) fin->Get(ecl_name);  //get bg spectra from sort code
    x_axis = htiming->GetXaxis();

  for(Int_t j=0; j<6; j++){              #loop over timing bins
    if(j<3) x=2; if(j>=3) x=4;
```

```
    lo = x_axis->FindBin( ((j+x)*250)-38 );     //same width as peak
    up = x_axis->FindBin( ((j+x)*250)+38 );
        //gate on spectra for six bins either side of timing peak

    BG[j] = htiming->Integral(lo,up);   //integrate each
    BG_D[i] += BG[j];                   //sum together
  }

  BG_D[i] /= 6;                         //find average
  mu = 0;
  for(Int_t j=0; j<6; j++){             #loop over timing bins
    mu += pow( (BG[j] - BG_D[i]),2 );
  }
  sig = sqrt( (0.1667 * mu) );
  BG_Err_D[i] = sig / sqrt(6);
}
```

To plot the angular bin data, the background (including that from the timing) is accounted for using the code below. The timing background for the bin is calculated by multiplying the detector background (calculated in the second script) with the background percentage (calculated in the first script).

```
for(Int_t i=1; i<NoBins+1; i++){        #loop over angular bins
  Bin_count = hcounts->GetBinContent(i+1);
                                //get state bin count from fitting routine
  Bin_error = sqrt(Bin_count);  //calculate error in counts

  for(Int_t j=1; j<7; j++){             #loop over detectors
    Bin_count -= (Int_t)(Bin_Ratio_D[j][i] * BG_D[j]);
    Bin_error = sqrt( pow(Bin_error,2)
                + pow((BG_Err_D[j] * Bin_Ratio_D[j][i]),2) );
  }
        //coincidence error subtracted from total counts
        //(error added in quadrature)

  Bin_count *= (Int_t)Efficiency[i];
  Bin_error = (Bin_count * Efficiency[i])
              * sqrt( pow((Bin_error / Bin_count),2)
              + pow((Eff_Err[i] / Efficiency[i]),2) );
        //bin count multiplied by efficiency
        //(error added in quadrature)

  Bin_count /= Total_count;
  Bin_error = (Bin_count / Total_count)
              * sqrt( pow((Bin_error / Bin_count),2)
              + pow((sqrt(Total_count) / Total_count),2) );
        //bin count divided by total count from fitting routine
        //(error added in quadrature)

  orsay_gr->SetPoint(point, Theta_mean[i], Bin_count);
  orsay_gr->SetPointError(point, Theta_error[i], Bin_error);
        //plot bin count and error
}
```

Appendix C

$1/2^-$ Interference Contribution

The missing 6939 keV state ($E_{c.m.} = 528$ keV, $J^\pi = 1/2^-$) is expected to have an α-particle width of $\Gamma_\alpha = 99(69)$ keV and a p width of $\Gamma_p = 34$ eV based on its mirror state assignment to the 6989 keV state in ^{19}F. Omitted from previous calculations, it has been included in Fig. C.1 to show its effect if the state were to exist with its current parameters. Also included are the individual contributions from the $1/2^-$ interference between the 26, 528 and 1233 keV states.

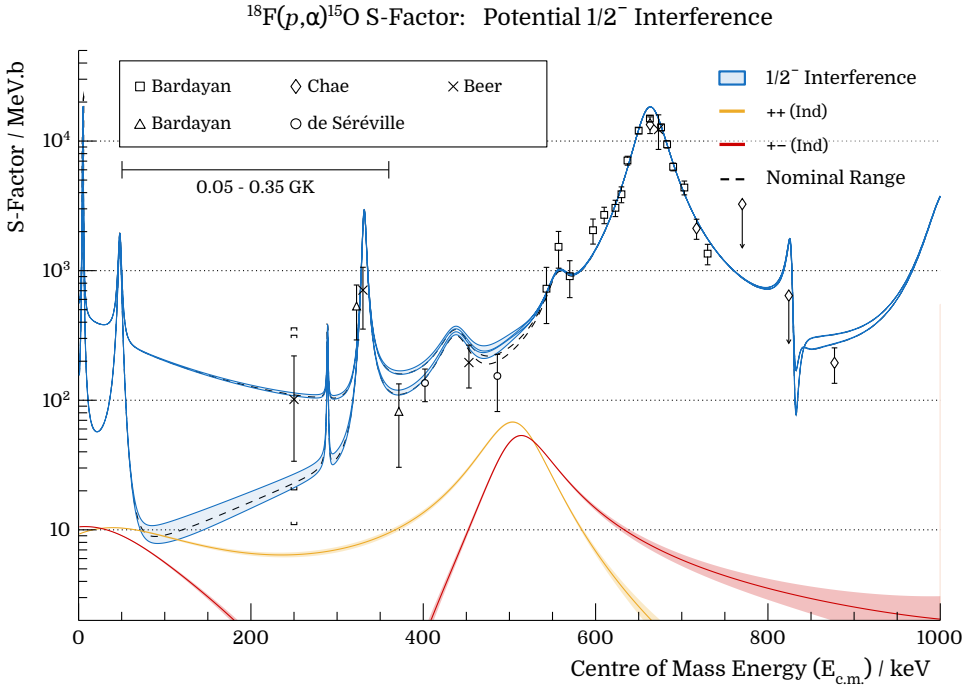

Figure C.1: Change in maximum and minimum S-factor from inclusion of the 528 keV resonance and its associated interference. The resonance's individual (Ind) contribution has been shown by the red and yellow curves.

Appendix D

Missing ^{19}Ne State Fit

The analysis of the ^{19}F(^{3}He,t)^{19}Ne experiment was undertaken prior to the publication by Cherubini *et al.* [62] and Parikh *et al.* [57] who found evidence for the 6537 and 6968 keV states respectively. The identification of new states from this work was not feasible due to the resolution of the focal plane, however, the 6537 and 6968 keV states have been included in the fitting routine in Fig. D.1 to show the improvements they make to the overall fit. The change to the fit also included the missing 7558 keV state given its slight improvement to the region.

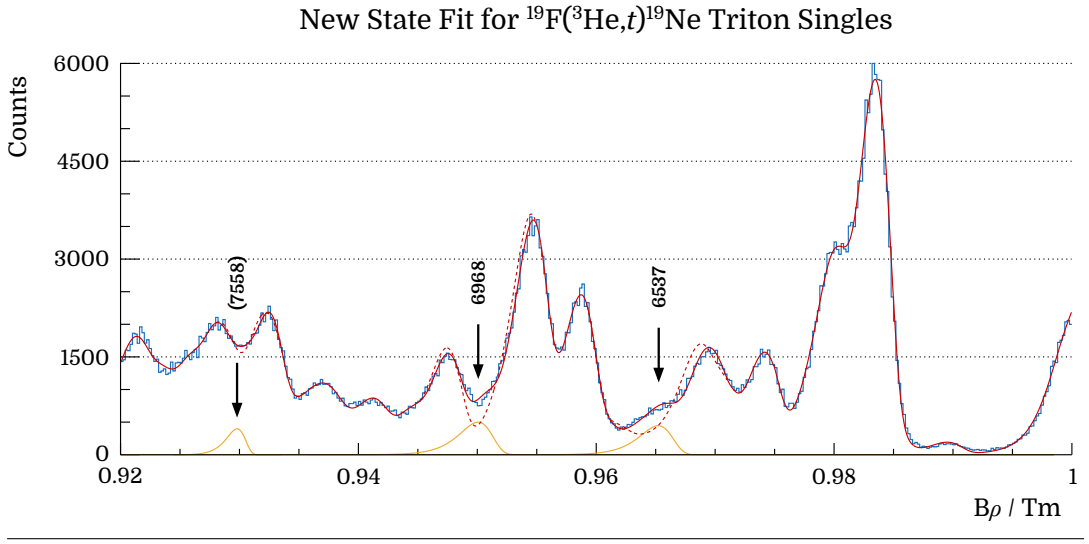

Figure D.1: Fitted function to the triton singles spectra including the highlighted missing states. The original fit is shown with a dashed line and the new fit with a solid line.

Bibliography

[1] E. Rutherford, *LXXIX. The Scattering of α and β Particles by Matter and the Structure of the Atom*, Philosophical Magazine Series 6 **21**, 669 (1911).

[2] A. G. W. Cameron, *Nuclear Reactions in Stars and Nucleogenesis* (1957).

[3] E. M. Burbidge *et al.*, *Synthesis of the Elements in Stars*, Reviews of Modern Physics **29**, 547 (1957).

[4] G. North, *Observing Variable Stars, Novae and Supernovae.* (Cambridge University Press, 2014).

[5] C. Iliadis, *Nuclear Physics of Stars* (Wiley-VCH Verlag GmbH & Co., 2008).

[6] T. M. B. Finzell, *A Detailed Study of the Gamma-Ray Nova V1324 SCO*, Ph.D. thesis, Michigan State University (2017).

[7] S. Chandrasekhar & E. A. Milne, *The Highly Collapsed Configurations of a Stellar Mass*, Monthly Notices of the Royal Astronomical Society **91**, 456 (1931).

[8] S. Chandrasekhar, *The Highly Collapsed Configurations of a Stellar Mass (Second Paper)*, Monthly Notices of the Royal Astronomical Society **95**, 207 (1935).

[9] J. José & M. Hernanz, *Beacons in the Sky: Classical Novae vs. X-ray Bursts*, European Physical Journal A **27**, 107 (2006).

[10] M. F. Bode & A. Evans, *Classical Novae* (Cambridge University Press, 2008).

[11] M. J. Darnley *et al.*, *Classical Novae from the POINT-AGAPE Microlensing Survey of M31 - II. Rate and Statistical Characteristics of the Nova Population*, Monthly Notices of the Royal Astronomical Society **353**, 571 (2006).

[12] J. José & M. Hernanz, *Nucleosynthesis in Classical Novae: CO versus ONe White Dwarfs*, The Astrophysical Journal **494**, 680 (1998).

[13] S. Starrfield *et al.*, *Evolutionary Sequences for Nova V1974 Cygni using New Nuclear Reaction Rates and Opacities*, Monthly Notices of the Royal Astronomical Society **296**, 502 (1998).

[14] R. D. Gehrz *et al.*, *Nucleosynthesis in Classical Novae and its Contribution to the Interstellar Medium*, Publications of the Astronomical Society of the Pacific **110**, 3 (1998).

[15] J. José, A. Coc & M. Hernanz, *Synthesis of Intermediate-Mass Elements in Classical Novae: from Si to Ca*, The Astrophysical Journal **560**, 897 (2001).

[16] J. José, M. Hernanz & C. Iliadis, *Nucleosynthesis in Classical Novae*, Nuclear Physics A **777**, 550 (2006).

[17] J. Casanova *et al.*, *Three-Dimensional Simulations of Turbulent Convective Mixing in ONe and CO Classical Nova Explosions*, Astronomy & Astrophysics **595**, A28 (2016).

[18] M. Hernanz, *Gamma-Ray Emission from Nova Outbursts*, arXiv **1305**, 0769 (2013).

[19] M. D. Leising & D. D. Clayton, *Positron Annihilation Gamma Rays from Novae*, The Astrophysical Journal **323**, 159 (1987).

[20] M. Hernanz, *BATSE Observations of Classical Novae*, in *AIP Conference Proceedings*, Vol. 510 (2000) p. 82–86.

[21] F. Senziani *et al.*, *Detectability of Gamma-Ray Emission from Classical Novae with Swift/BAT*, Astronomy and Astrophysics **485**, 223 (2008).

[22] M. Hernanz & J. José, *Updated Prospects for Detectability of Classical Novae with INTEGRAL*, in *European Space Agency, (Special Publication)*, 552 (2004) p. 95–98.

[23] D. W. Bardayan *et al.*, *The Astrophysically Important 3^+ State in ^{18}Ne and the $^{17}F(p,\gamma)^{18}Ne$ Stellar Rate*, Physical Review C **62**, 055804 (2000).

[24] C. Fox *et al.*, *Thermonuclear Reaction Rate of $^{17}O(p,\gamma)^{18}F$*, Physical Review C **71**, 055801 (2005).

[25] J. José, *Stellar Explosions: Hydrodynamics and Nucleosynthesis* (CRC / Taylor & Francis, 2017).

[26] J. D. Garrett, R. Middleton & H. T. Fortune, *Hole States in ^{19}Ne*, Physical Review C **2**, 1243 (1970).

[27] D. S. Haynes, K. W. Kemper & N. R. Fletcher, *Reaction $^{20}Ne(^3He,\alpha)^{19}Ne$ at 18 MeV*, Physical Review C **5**, 5 (1972).

[28] M. Wiescher, *Warm CNO Nucleosynthesis as a Possible Enrichment Mechanism for Oxygen and Fluorine Isotopes*, The Astrophysical Journal **263**, 891 (1982).

[29] D. R. Tilley *et al.*, *Energy Levels of Light Nuclei A = 18-19*, Nuclear Physics A **595**, 1 (1995).

[30] K. E. Rehm *et al.*, *Study of the $^{18}F(p,\alpha)^{15}O$ Reaction at Astrophysical Energies Using a ^{18}F Beam*, Physical Review C **52**, R460 (1995).

[31] K. E. Rehm *et al.*, *Astrophysical Reaction Rate for the $^{18}F(p,\alpha)^{15}O$ Reaction*, Physical Review C **53**, 1950 (1996).

[32] K. E. Rehm *et al.*, *Exploring the $^{18}F(p,\gamma)^{19}Ne$ Gateway to the Formation of Heavy Elements in Hot Stars*, Physical Review C **55**, R566 (1997).

[33] R. Coszach *et al.*, *A Direct Measurement of the $^{18}F(p,\alpha)^{15}O$ Reaction*, Physics Letters B **353**, 184 (1995).

[34] J. Graulich *et al.*, *The $^{18}F(p,\alpha)$ Reaction and its Astrophysical Implications*, Nuclear Physics A **626**, 751 (1997).

[35] D. W. Bardayan *et al.*, *Destruction of ^{18}F via $^{18}F(p,\alpha)^{15}O$ Burning Through the $E_{c.m.}$ = 665 keV Resonance*, Physical Review C **63**, 065802 (2001).

[36] S. Utku *et al.*, *Breakout from the Hot CNO Cycle: The $^{18}F(p,\gamma)$ vs $^{18}F(p,\alpha)$ Branching Ratio*, Physical Review C **57**, 2731 (1998).

[37] A. Coc *et al.*, *Influence of New Reaction Rates on ^{18}F Production in Novae*, Astronomy and Astrophysics **357**, 561 (2000).

[38] D. W. Bardayan *et al.*, *Strength of the $^{18}F(p,\alpha)^{15}O$ Resonance at $E_{c.m.}$ = 330 keV*, Physical Review Letters **89**, 262501 (2002).

[39] D. W. Bardayan *et al.*, *Search for Astrophysically Important ^{19}Ne Levels with a Thick-Target $^{18}F(p,p)^{18}F$ Measurement*, Physical Review C **70**, 015804 (2004).

[40] D. W. Bardayan, R. L. Kozub & M. S. Smith, *^{19}F α Widths and the ^{18}F+p Reaction Rates*, Physical Review C **71**, 018801 (2005).

[41] K. Y. Chae *et al.*, *First Experimental Constraints on the Interference of $3/2^+$ Resonances in the $^{18}F(p,\alpha)^{15}O$ Reaction*, Physical Review C **74**, 012801 (2006).

[42] N. de Séréville *et al.*, *New Low-Energy Measurement of the $^{18}F(p,\alpha)^{15}O$ Reaction*, European Physical Journal: Special Topics **150**, 211 (2007).

[43] N. de Séréville *et al.*, *Low-Energy $^{18}F(p,\alpha)^{15}O$ Cross Section Measurements Relevant to Nova γ-ray Emission*, Physical Review C **79**, 015801 (2009).

[44] N. de Séréville *et al.*, *Study of the $^{18}F(p,\alpha)^{15}O$ Reaction for Application to Nova γ-ray Emission*, Nuclear Physics A **718**, 259 (2003).

[45] N. de Séréville *et al.*, *$^{2}H(^{18}F,p\alpha)^{15}N$ Reaction Applied to Nova γ-ray Emission*, Physical Review C **67**, 052801 (2003).

[46] N. de Séréville, E. Berthoumieux & A. Coc, *The $^{18}F(p,\alpha)^{15}O$ Reaction Rate for Application to Nova γ-ray Emission*, Nuclear Physics A **758**, 745 (2005).

[47] N. de Séréville *et al.*, *Indirect Study of ^{19}Ne States near the ^{18}F+p Threshold*, Nuclear Physics A **791**, 251 (2007).

[48] R. L. Kozub *et al.*, *New Constraints on the $^{18}F(p,\alpha)^{15}O$ Rate in Novae from the (d,p) Reaction*, Physical Review C **71**, 032801 (2005).

[49] R. L. Kozub *et al.*, *Neutron Single Particle Strengths from the (d,p) Reaction on ^{18}F*, Physical Review C **73**, 044307 (2006).

[50] C. D. Nesaraja *et al.*, *Nuclear Structure Properties of Astrophysical Importance for ^{19}Ne Above the Proton Threshold Energy*, Physical Review C **75**, 055809 (2007).

[51] A. Coc, *Nucleosynthesis in Novae: Experimental Progress in the Determination of Nuclear Reaction Rates*, in *American Institute of Physics Conference Proceedings*, Vol. 1016 (2008) p. 119–126.

[52] A. M. Laird *et al.*, *Is γ-ray Emission from Novae Affected by Interference Effects in the ^{18}F(p,α)^{15}O Reaction?*, Physical Review Letters **110**, 032502 (2013).

[53] A. S. Adekola *et al.*, *First Proton-Transfer Study of ^{18}F+p Resonances Relevant for Novae*, Physical Review C **83**, 052801 (2011).

[54] C. Akers *et al.*, *Measurement of Radiative Proton Capture on ^{18}F and Implications for Oxygen-Neon Novae*, Physical Review C **94**, 262502 (2013).

[55] A. S. Adekola *et al.*, *^{19}Ne Levels Studied with the ^{18}F(d,n)^{19}Ne*(^{18}F+p) Reaction*, Physical Review C **85**, 037601 (2012).

[56] M. Dufour & P. Descouvemont, *The ^{18}F(p,α)^{15}O Low-Energy S-factor: A Microscopic Approach*, Nuclear Physics A **785**, 381 (2007).

[57] A. Parikh *et al.*, *Spectroscopy of ^{19}Ne for the Thermonuclear ^{15}O(α,γ)^{19}Ne and ^{18}F(p,α)^{15}O Reaction Rates*, Physical Review C **92**, 055806 (2015).

[58] A. S. Adekola, *Proton-Transfer Study of Unbound ^{19}Ne States via ^{2}H(^{18}F,α+^{15}O)n Reaction*, Ph.D. thesis, Ohio University (2009).

[59] A. S. J. Murphy *et al.*, *Simultaneous Measurement of the ^{18}F(p,p)^{18}F and ^{18}F(p,α)^{15}O Reactions: Implications for the Level Structure of ^{19}Ne, and for ^{18}F Production in Novae*, Physical Review C **79**, 058801 (2009).

[60] F. Boulay *et al.*, *A New Broad Resonance in ^{19}Ne Relevant for the Study of Novae* (2017), to be published.

[61] D. W. Bardayan *et al.*, *The First Science Result with the JENSA Gas-Jet Target: Confirmation and Study of a Strong Subthreshold ^{18}F(p,α)^{15}O Resonance*, Physics Letters, Section B: Nuclear, Elementary Particle and High-Energy Physics **751**, 311 (2015).

[62] S. Cherubini *et al.*, *First Application of the Trojan Horse Method with a Radioactive Ion Beam: Study of the ^{18}F(p,α)^{15}O Reaction at Astrophysical Energies*, Physical Review C **92**, 015805 (2015).

[63] J. C. Dalouzy *et al.*, *Discovery of a New Broad Resonance in ^{19}Ne: Implications for the Destruction of the Cosmic γ-Ray Emitter ^{18}F*, Physical Review Letters **102**, 162503 (2009).

[64] D. J. Mountford *et al.*, *Resonances in ^{19}Ne with Relevance to the Astrophysically Important ^{18}F(p,α)^{15}O Reaction*, Physical Review C **85**, 022801 (2012).

[65] A. S. Adekola *et al.*, *Single-Nucleon Transfer Reactions on ^{18}F*, Physical Review C **84**, 054611 (2011).

[66] C. E. Beer *et al.*, *Direct Measurement of the $^{18}F(p,\alpha)^{15}O$ Reaction at Nova Temperatures*, Physical Review C **83**, 042801 (2011).

[67] G. J. Feldman & R. D. Cousins, *Unified Approach to the Classical Statistical Analysis of Small Signals*, Physical Review D **57**, 3873 (1998).

[68] W. A. Rolke, A. M. López & J. Conrad, *Limits and Confidence Intervals in the Presence of Nuisance Parameters*, Nuclear Instruments and Methods in Physics Research A **551**, 493 (2005).

[69] C. Iliadis *et al.*, *The Effects of Thermonuclear Reaction-Rate Variations on Nova Nucleosynthesis: A Sensitivity Study*, The Astrophysical Journal Supplement Series **142**, 105 (2002).

[70] I. J. Thompson & F. M. Nunes, *Nuclear Reactions for Astrophysics: Principles, Calculation and Applications of Low-Energy Reactions* (Cambridge University Press, 2011).

[71] G. R. Satchler, *Introduction to Nuclear Reactions* (Palgrave Macmillan UK, 1990).

[72] A. M. Lane & R. G. Thomas, *R-matrix Theory of Nuclear Reactions* (1958).

[73] E. Vogt, *Oct 4-8th lecture notes*, R-Matrix School of the Joint Institute for Nuclear Astrophysics, Notre Dame (2004).

[74] J. G. Pronko & R. A. Lindgren, *Angular Correlations of Sequential Particle Decay for Aligned Nuclei*, Nuclear Instruments and Methods **98**, 445 (1972).

[75] H. Enge, *Magnetic Spectrographs and Beam Analyzers*, Nuclear Instruments and Methods **28**, 119 (1964).

[76] J. Spencer & H. Enge, *Split-pole Magnetic Spectrograph for Precision Nuclear Spectroscopy*, Nuclear Instruments and Methods **49**, 181 (1967).

[77] H. A. Enge, *Magnetic Spectrographs for Nuclear Reaction Studies*, Nuclear Instruments and Methods **162**, 161 (1979).

[78] Micron, *Semiconductor Specification Sheet*, Tech. Rep. (Micron Semiconductor Ltd, 2017).

[79] G. F. Knoll, *Radiation Detection and Measurement*, 3rd ed. (John Wiley & Sons, 2000).

[80] A. Matta *et al.*, *NPTool: A Simulation and Analysis Framework for Low-Energy Nuclear Physics Experiments*, Journal of Physics G: Nuclear and Particle Physics **43**, 045113 (2016).

[81] S. Agostinelli *et al.*, *GEANT4 - A Simulation Toolkit*, Nuclear Instruments and Methods in Physics Research A **506**, 250 (2003).

[82] D. W. Visser, *Particle Decay Branching Ratios for States of Astrophysical Importance in ^{19}Ne*, Ph.D. thesis, Yale University (2003).

[83] D. W. Visser *et al.*, *Particle Decay Branching Ratios for States of Astrophysical Importance in ^{19}Ne*, Physical Review C **69**, 048801 (2004).

[84] R. E. Azuma *et al.*, *AZURE: An R-matrix Code for Nuclear Astrophysics*, Physical Review C **81**, 045805 (2010).

[85] C. Iliadis *et al.*, *Charged-Particle Thermonuclear Reaction Rates: II. Tables and Graphs of Reaction Rates and Probability Density Functions*, Nuclear Physics A **841**, 31 (2010).

[86] A. L. Sallaska *et al.*, *STARLIB: A Next-Generation Reaction-Rate Library for Nuclear Astrophysics*, The Astrophysical Journal Supplement Series **207**, 18 (2013).

[87] F. Herwig *et al.*, *Nucleosynthesis Simulations for a Wide Range of Nuclear Production Sites from NuGrid*, in *Proceedings of Science* (2008) p. 1–5.

[88] R. H. Cyburt *et al.*, *The JINA Reaclib Database: Its Recent Updates and Impact on Type-I X-Ray Bursts*, The Astrophysical Journal Supplement Series **189**, 240 (2010).

[89] P. A. Denissenkov *et al.*, *MESA and NuGrid Simulations of Classical Novae: CO and ONe Nova Nucleosynthesis*, Monthly Notices of the Royal Astronomical Society **442**, 2058 (2014).

[90] J. H. Aitken *et al.*, *A Survey of New Resonances in the $^{15}N(\alpha,\gamma)^{19}F$ Reaction*, Canadian Journal of Physics **48**, 1617 (1972).

[91] W. Dixon & R. Storey, *Levels of ^{19}F from the $^{15}N(\alpha,\gamma)^{19}F$ Reaction for E_α = 2.8–4.0 MeV*, Nuclear Physics A **284**, 97 (1977).

[92] H. Smotrich *et al.*, *Elastic Scattering of Alpha Particles by N15*, Physical Review **122**, 232 (1961).